Development of novel imaging tools for selected biomedical applications

Omar E. Olarte

Advisor: Prof. Pablo Loza-Alvarez

PhD in Photonics – The Institute of Photonic Sciences – 2013

Contents

Table of Figures

Table of tables

Abstract

In the quest for better and faster images of cellular and subcellular structures, biology-oriented optical microscopes have advanced significantly in the last few decades. Novel microscopy techniques such as non-linear microscopy (NLM), including two-photon excited fluorescence (TPEF) and second harmonic generation (SHG) microscopy, and light-sheet fluorescence microscopy (LSFM) are emerging as alternatives that overcome some the intrinsic limitations of standard microscopy systems. In this thesis I aimed to advance such techniques even more, and combine them with other photonic technologies to provide novel tools that would help to address complex biological questions. This thesis is organized in two main parts. The first part is dedicated to applications involving femtosecond lasers that are employed for precise microsurgery. For that, damage assessment methodologies based on NLM were developed and tested in relevant biomedical models. In the second part, wavefront engineering methods were employed to enhance the imaging capabilities of light-sheet microscopy systems. These novel methodologies were tested as well in relevant biological applications. This thesis is, therefore, organized as follows:

In chapter 1, a brief and comprehensive review of the basic microscopy techniques employed in this thesis is presented, together with the challenges and achievements of this thesis in sequential order.

In chapter 2, a multimodal imaging methodology for the assessment of laser induced collateral damage is presented. This was specifically developed for the control of the damage in femtosecond-laser dissection of single axons within a living *Caenorhabditis elegans* (*C. elegans*). Here, it is shown that collateral damages at the level of the myosin structure of the muscles adjacent to the axon, can be readily detected.

In chapter 3, the optimized multimodal methodology developed in the chapter 2 was employed for minimally invasive dissection of axons of D-type motoneurons in *C elegans*.

Here, a microfluidic chip for *C elegans* immobilization and a detailed protocol was employed to evaluate the axon regeneration of such neurons. The potential of such platform for testing drugs with regeneration-enhancing capabilities is also presented.

In chapter 4, a novel use of TPEF microscopy is presented to characterize and fine tune the laser for photodisruption of excised human crystalline lens samples.

In chapter 5, a thorough description of the implementation of a multimodal Digital Scanned Light-Sheet Microscope (DSLM) able to work in the linear and nonlinear regimes under either Gaussian or Bessel beam excitation schemes, is presented. The enhanced capabilities of the developed system is evaluated using *in vivo C. elegans* samples and multicellular tumor spheroids

In chapter 6, the development of a completely new concept in light sheet-based imaging is presented. This is based on the extension of the depth-of-field of the lens in the emission path of the microscope by using wavefront coding (WFC) techniques. Furthermore, I demonstrate the application of the developed methodology for fast volumetric imaging of living biological specimens and 3D particle tracking.

Chapter 1: Introduction

Major advancements in biological research have been possible by the developing of novel techniques and instrumentation in the fields of optics and photonics. This imposes an enormous challenge that certainly pushes the limits of the optical sciences. Laser development and optical microscopy may have not been the same without the fruitful interaction with biological sciences. Since their introduction in the second half of the twentieth century, lasers have been proven to be versatile and effective tools to non-invasive examination and sub-cellular manipulation of biological samples. The use of lasers to obtain high resolution images of cellular structures is now a daily practice in many biological laboratories around the world. Of special interest for biology is the development of techniques based on the observation of selected fluorescent structures inside the samples. These structures are usually labelled with vital dyes or have attached genetically-encoded proteins that make them fluorescent (in some specimens this is an intrinsic characteristic). In the typical fluorescence (wide-field) microscope the specimen is illuminated with laser light of a specific wavelength which is absorbed by this fluorescent elements, or fluorophores, causing them to emit light of longer wavelengths. This light is then collected using a CCD camera. The main drawback of this configuration is that planes at different depths inside the specimen are excited at the same time. The resulting detected fluorescence includes a large unfocused background component. To eliminate the out-of-focus signals, a confocal configuration is used. A confocal microscope normally uses a high numerical aperture (NA) for creating a diffraction-limited illumination point and uses a pinhole, located in an optically conjugated plane in front of the detector, to eliminate out-of-focus signal. In this way, only the light produced very close to the focal plane can be detected and, in consequence, *optical sectioning* is achieved. In confocal microscopy the focused laser beam, usually in the visible wavelength range, is raster-scanned across the sample to produce an optical section from the selected field of view, this is why this technique is usually termed Confocal Laser Scanning Microscopy (CLSM) [1]. This technique has emerged as a very powerful tool for biological imaging. Its ability to provide high transversal and axial resolution, collect three-dimensional images of relatively thick specimens, together with the user friendliness and versatility of modern

commercial confocal microscopes, has made it the biologist's preferred imaging tool. However, the use of short wavelengths for exciting the fluorescence makes it suffer from fundamental penalties such as phototoxicity/photodamage and low penetration depth due to the strong dependence of scattering coefficients with the wavelength. On the other hand, Nonlinear microscopy (NLM) techniques [2,3], such as two-photon excited fluorescence (TPEF), second harmonic generation (SHG) and third harmonic generation (THG)have resulted in an interesting alternative to CLSM. NLM relies in the use of ultrashort-pulsed lasers which normally emit in the near infrared (NIR) spectral region. The nonlinear contrast is based on second and third-order nonlinear light-matter interactions. Since these nonlinear optical effects are proportional to the second or third power of the fundamental light intensity, they are induced only at the focus of a high numerical aperture (NA) microscope objective. This fact results in the intrinsic elimination of the out-of-focus contributions and results in the intrinsic optical sectioning inherent to nonlinear imaging techniques. Therefore, it is a straightforward task to generate a sharp, three-dimensional image. The excitation beam is simply raster scanned across the focal plane, and the signal generated as a result of the nonlinear excitation is measured and correlated to the beam position in a similar way as CLSM. Imaging using NLM possess several advantages over conventional CLSM: i) it possess intrinsic optical sectioning without the need of any pinhole (and thus all the generated light is used), ii) nonlinear excitation is done normally in the NIR and, as a consequence, larger penetration depths can be achieved, iii) there is a reduced photobleaching as the interaction occurs only at the focal point and iv) NML is amenable for label-free imaging, that is the case of SHG and THG, among others. Nonlinear microscopes provide immense possibilities in biological investigation, but the possibility of counting also with complementary linear imaging techniques is, in many cases, desirable.

Optical microscopes, as any other optical instrument, are limited by a fundamental maximum of resolution determined by the diffraction. This is called the *diffraction limit* of resolution. High-end objectives employed for any of the afore-mentioned microscopy techniques are designed to have very high imaging performance close to the diffraction limit of resolution. However, this is only true when ideal conditions are met, e. g. the sample under observation is thin and transparent. Therefore,

resolution of these microscopes is often compromised by the optical properties of the specimen itself. Spatial variations in the refractive index of the specimen introduce optical aberrations that hinder image quality. This is a particular problem when imaging deep into thick biological specimens. Ultimately, the aberrations restrict the amount of specimen that can be observed by the microscope. This is a serious limitation if one wants to observe cells and their processes in their usual environment, rather than in the unnatural surroundings of a microscope slide. To ameliorate such problems Adaptive Optics (AO) may be used. AO has been broadly applied in astronomy to reduce the effects of changing atmospheric conditions which produce aberrations and deteriorate the image quality of stars and satellites. By employing wavefront sensors (WFS) and deformable mirrors (DM), the distortions produced when distant light sources travel through the turbulent atmosphere can be corrected. This concept can be extrapolated to the problem of aberration compensation in microscopy [4]. There are several approaches to measure and correct sample related wavefront aberrations in fluorescence microscopy. For NLM, correction of the excitation beam will ensure a better focussing and therefore, a more efficient nonlinear process. In practice, measuring and correcting fundamental beam aberrations of microscopes is a difficult task. However, this can be done by finding a well-defined, localized and bright enough source for measuring the aberrations. This is known in AO community as *guide star*. Strategies have been proposed to guide star-like analogous by introducing artificial guide stars (fluorescent micron-sized beads) into the sample [5]. However, this interferes with the sample being an invasive technique. Other alternatives are not based on guide stars and correct the aberrations by optimizing a figure-of-merit defined on the captured images. Both solutions have limited applications and may compromise the viability of delicate/living biological specimens.

My PhD started in this point by trying to find a solution to the challenge of defining a reliable protocol to measure and correct aberrations in the excitation beam of NLM. For this, we presented a novel method taking advantage of the fact that nonlinear excitation (particularly TPEF) occurs only in a highly localized and confined region of the sample. This can in fact be considered a natural reference source which we called *nonlinear guide star*. Using this concept we demonstrated, for the first time,

the use of intrinsically generated guide stars for the purposes of wavefront measurement and correction in AO microscopy. This principle has been demonstrated with both, moderate and increased scattering samples. In both cases we found a TPEF signal improvement.

This work shows an initial example of the use wavefront engineering methods, in this case AO, to attack problems encountered in biological microscopy.

At this point, I realized the big potential that such kind of technology would have to other applications, particularly to laser-based surgery.

Ultrashort-pulsed lasers used for NLM can be employed as well to perform dissections on selected targets on a variety of biological samples. The most significant advantage of using these lasers is the confinement of induced effects to the focal volume owing to the involvement of nonlinear absorption mechanisms. Some of the many applications of femtosecond laser surgery in bio -medical applications are: neuronal axotomy in *C. elegans* [6], wound response of *Drosophila melanogaster* embryos during dorsal closure [7], subcellular nanosurgery in cell cytoskeleton [8], and human eye corneal surgery [9], among others. The physical mechanisms involved in laser ablation of transparent dielectric materials with femtosecond lasers are well known [10]. When ultrashort pulses of NIR light are focused to a tight spot through high NA microscope objective, high peak intensities are achieved at the sample plane with relatively low pulse energies. This generates nonlinear photon (multiphoton) absorption in an otherwise transparent medium and electron ionization within the focal volume. Then, free-electron density increases exponentially due to a process termed as cascade ionization. At a critical density, the resulting free-electron plasma causes optical breakdown and physical disruption of the material. Pulse width and the focusing strength determine the intensity threshold to produce optical breakdown. This suggests that laser parameters can be finely tuned to control the effects of the generated plasma and the subsequent optical breakdown into the irradiated volume.

Following this route, I was devoted to build and optimize a microscopy system capable of high-precision surgery that would be applied to relevant biological and biomedical problems, such as neuron regeneration and crystalline lens softening.

On the other hand, the visualization and quantification of biological processes in difficult samples such as living organisms and tissue models require microscopy methods that can provide 3-dimensional data with high spatial and temporal resolutions over a large field of view. Nevertheless, microscopy methods employed for such difficult tasks should also minimize the phototoxic effects of laser irradiation. For example, In CLSM, every time an optical section is captured, fluorescence in many other axial planes is excited and rejected by the confocal pinhole. This led to an accumulative phototoxicity/photodamage when volumetric imaging is required. Light-sheet fluorescence microscopy (LSFM), also known as selective plane illumination microscopy (SPIM) [11], has been proven to be an interesting alternative to CSLM. In LSFM a thin laminar sheet illuminate sample form the side, thus exciting only a two-dimensional section of the sample. The emitted fluorescence is imaged along an optical axis perpendicular to the illumination plane. This atypical configuration provides intrinsic optical sectioning, with no energy deposition outside the optical section; large fields of view imaging, and enables isotropic resolution [12]. In spite of all this, LSFM still carries the problem of using lasers in the visible wavelengths for excitation, and then is prone to scattering.

Thinking on this, I became aware of the potential of another wavefront engineering technology to modify the point spread function (PSF) of a system but this time to produce thin, long “needles” of light. This “needles”, known as Bessel beams [13], have shown to have interesting properties that make them to keep well formed when propagate inside highly scattering samples. Therefore, I explored the potential of such beams to build a multimodal LSFM, which in combination with femtosecond lasers in the excitation arm, provided a system with high resolution, enhanced contrast and large field-of-view imaging.

Finally, having a 3D microscopy technique that would allow the observation of fast events with high resolutions in a large field of view is of extreme importance for biological applications. Such a technique would allow for a better understanding of complex dynamic processes in living cells, tissues and organisms. Calcium waves of heart and brain cellular cultures, the embryonic zebrafish beating heart and the red blood cells in the developing cardio-vascular are a few of the most challenging

biological processes calling for faster microscopy techniques [14]. LSFM with its many advantages have shown important improvements in terms of speed as compared with regular CLSM. Nevertheless, the need to mechanically scan the sample to retrieve the optical sections sets the limit of the volumetric imaging speed that can be achieved by LSFM.

To deal with this, I have explored the use of a similar wavefront engineering approach applied to the collection path of the previously developed light-sheet microscope. For this, an optical setup inspired in the principles of AO that can effectively provide the system capable to overcome the intrinsic speed limit present in regular LSFM. I will show how this allowed us to obtain fast volumetric imaging of living animals and fast 3D particle tracking.

1.1 References

1. J. B. Pawley, *Handbook of biological confocal microscopy* (Springer, 2006).

2. W. R. Zipfel, R. M. Williams, y W. W. Webb, "Nonlinear magic: multiphoton microscopy in the biosciences," Nat Biotech **21**, 1369-1377 (2003).

3. R. Carriles, D. N. Schafer, K. E. Sheetz, J. J. Field, R. Cisek, V. Barzda, A. W. Sylvester, y J. A. Squier, "Invited Review Article: Imaging techniques for harmonic and multiphoton absorption fluorescence microscopy," Rev. Sci. Instrum. **80**, 081101 (2009).

4. M. J. Booth, "Adaptive optics in microscopy," Philos. Trans. R. Soc. Math. Phys. Eng. Sci. **365**, 2829-2843 (2007).

5. X. Tao, B. Fernandez, O. Azucena, M. Fu, D. Garcia, Y. Zuo, D. C. Chen, y J. Kubby, "Adaptive optics confocal microscopy using direct wavefront sensing," Opt. Lett. **36**, 1062 (2011).

6. M. Yanik, H. Cinar, H. Cinar, A. Chisholm, Y. Jin, y A. Ben-Yakar, "Neurosurgery - Functional regeneration after laser axotomy," Nature **432**, 822-822 (2004).

7. A. Thayil, A. Pereira, M. Mathew, D. Artigas, E. Blanco, y P. Loza-Alvarez, "Decrease in laser ablation threshold for epithelial tissue microsurgery in a living Drosophila embryo during dorsal closure," J. Microsc. **232**, 362-368 (2008).

8. S. Kumar, I. Z. Maxwell, A. Heisterkamp, T. R. Polte, T. P. Lele, M. Salanga, E. Mazur, y D. E. Ingber, "Viscoelastic retraction of single living stress fibers and its impact on cell shape, cytoskeletal organization, and extracellular matrix mechanics," Biophys. J. **90**, 3762-3773 (2006).

9. A. Heisterkamp, T. Ripken, T. Mamom, W. Drommer, H. Welling, W. Ertmer, y H. Lubatschowski, "Nonlinear side effects of fs pulses inside corneal tissue during photodisruption," Appl. Phys. B **74**, 419-425 (2002).

10. A. Vogel, J. Noack, G. Hüttman, y G. Paltauf, "Mechanisms of femtosecond laser nanosurgery of cells and tissues," Appl. Phys. B **81**, 1015-1047 (2005).

11. J. Huisken, J. Swoger, F. Del Bene, J. Wittbrodt, y E. H. K. Stelzer, "Optical Sectioning Deep Inside Live Embryos by Selective Plane Illumination Microscopy," Science **305**, 1007 -1009 (2004).

12. J. Mertz, "Optical sectioning microscopy with planar or structured illumination," Nat. Methods **8**, 811-819 (2011).

13. J. Durnin, "Exact solutions for nondiffracting beams. I. The scalar theory," J. Opt. Soc. Am. A **4**, 651-654 (1987).

14. J. Vermot, S. E. Fraser, y M. Liebling, "Fast fluorescence microscopy for imaging the dynamics of embryonic development," HFSP J. **2**, 143-155 (2008).

Chapter 2: Femtosecond laser axotomy in *Caenorhabditis elegans* and collateral damage assessment using a combination of linear and nonlinear imaging techniques

2.1 Abstract

In this work, highly localized femtosecond laser ablation is used to dissect single axons within a living *Caenorhabditis elegans* (*C. elegans*). We present a multimodal imaging methodology for the assessment of the collateral damage induced by the laser. This relies on the observation of the tissues surrounding the targeted region using a combination of different high resolution microscopy modalities. We present the use of Second Harmonic Generation (SHG) and Polarization Sensitive SHG (PSHG) to determine damage in the neighbor muscle cells. All the above is done using a single instrument: the multimodal microscopy setup that allows simultaneous imaging in the linear and non-linear regimes, and femtosecond-laser ablation.

2.2 Introduction

Nowadays lasers are one of the most powerful and versatile tools in the biomedical field. Apart from their use in macro-and microscopic imaging techniques, their application in the non-invasive modification of biological samples is of particular importance. For these purposes, ultrashort pulsed lasers employing near infrared wavelengths have been shown to be the ideal tool when a very controlled and precise modification is required. These lasers have the ability to induce nonlinear photoionization and thereby to confine interaction to the focal volume (<1 femtoliter) of a tightly focused beam[1]. This enables controlled incisions with submicrometer precision can be induced. In addition to this, the use of near infra-red (NIR) light provides much higher tissue penetration due to a reduced (linear) absorption and scattering of the sample. This is opening up a whole new window for laser nanosurgery as a non-invasive powerful surgery technique that can be applied in a vast range of biomedical areas.

Although the precision of the femtosecond laser scalpel in biological samples is widely accepted to be superior to other surgical techniques, the complex nature of the

interaction calls for stringent tests on how precise this tool is. A logical way to perform these tests is to observe how much damage is sustained in the structures surrounding the target of surgery and, specially, in a specific biological sample. Assessment of this collateral damage is not just important to validate the precision of the surgical tool but it would also help to understand how a specific biosample responds to the surgery (chemically, structurally and behaviorally). Such determination of collateral damage is not trivial when the surgery is performed at the microscopic or submicroscopic level. Ordinary transmission light microscopes are not optimal for a detailed characterization of the resultant low-contrast subcellular modifications. For this reason, researchers have opted for the use of contrast enhancing microscopy techniques to observe and characterize the effects of laser irradiation. Among them, fluorescence microscopy has been particularly useful to monitor the laser induced damage to the cells, either by using a fluorescent reporter of the chemical species leading to cell degradation (e.g. reactive oxygen species ROS[2]) or by following the rise in auto fluorescence signal in the surroundings of the dissected area [3][4].

A very interesting case of the use of femtosecond lasers for subcellular surgery is the dissection of axons, or axotomy, of the nematode *Caenorhabditis elegans* (*C. elegans*). Single *C. elegans* neurons were first used as targets for laser surgery in a report by Yanik *et al.*[5]. In this study spontaneous axon regeneration was observed for the first time in this model organism. Moreover, individual axons of *C. elegans* were precisely cut with a focused femtosecond laser beam inducing an anomalous behavioral response that was restored to normal once the regeneration was completed. This technique allowed not only the study of the response of the organism to a single axon dissection but also a much more exhaustive study at different levels of neuronal interconnections and their particular regeneration properties[6][7] [8][9].

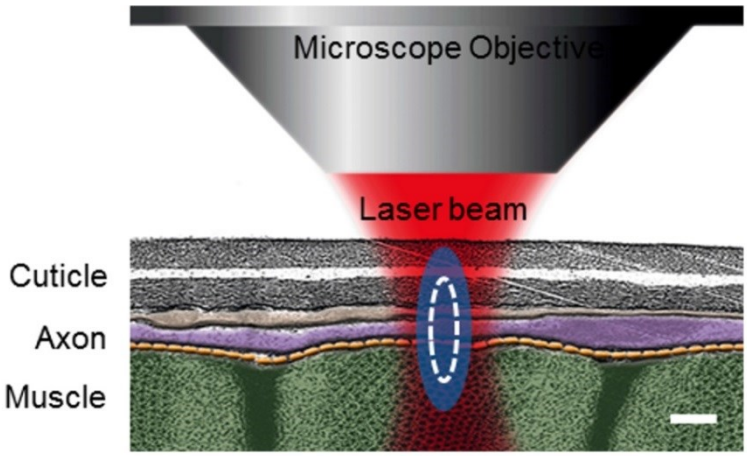

Figure 2.1: TEM illustration of the anatomical region of C. elegans where the laser axotomy is performed.
Body wall muscles are shown in green, axons in purple and cuticle in gray. Blue ellipsoid is the estimated full-width-at-half-maximum of the beam's point spread function. White line represents the limit of the maximum plasma density generated at the focal spot. Scale bar 300 nm

C. elegans D-type motoneurons are particularly attractive for the study of collateral damage induced during a femtosecond laser axotomy due to several reasons. First, these neurons extend axons that are extremely thin (few hundred nanometers) and reside in a complex environment surrounded by cuticle (above) and muscle (below) as can be seen in Figure 2.1. (background figure adapted from Wormatlas [10]). This means that even a very tiny mis-targeting or inaccuracy in the use of the laser surgery tool would show up as a collateral damage in the surrounding structures. Secondly, they provide an effective method towards the understanding of the triggered responses after axotomy that lead to axon regeneration [5][6][7][8][9]. Therefore, having a system that produces very precise cuts and has the capability to readily detect any unwanted/collateral damage is very important in the understanding of the mechanisms of neuronal regeneration.

So far, evaluation of collateral damage resulting from axotomy has been done by employing widefield fluorescence microscopy to measure the separation of the axon ending tips as well as the size of the damage in the muscle cell in close proximity to the axons. Both axons and muscles were labeled by green fluorescent protein (GFP) [11] [12]. While this can provide an approximate indication of the size of the damaged areas, there is still the need for methods that would provide more detailed information about the extent and the nature of the collateral damage, as well as the

many processes that could take place during the surgery. In a previous work, we showed how the combination of confocal fluorescence microscopy simultaneously with laser-scanned transmitted light microscopy (LT) provides a powerful tool not only for the real-time observation of the surgery with high resolution but also for the study of the different dynamical processes happening during the procedure [4]. Nevertheless, these linear microscopy techniques do not fully take advantage of the endogenous sources of contrast present in the region surrounding the operated axon. Particularly, the muscular structures of the *C. elegans* nematode have been shown to be sources of Second Harmonic Generation (SHG), a nonlinear optical effect that can be excited with ultrashort pulsed lasers [13].

In contrast to confocal and two-photon excited fluorescence (TPEF), which rely on photon absorption, SHG is a nonlinear scattering process and hence, in principle, it deposits no energy to the matter with which light interacts. The energy conservation and label-free characteristics enable minimally invasive imaging, which is highly desirable especially for *in vivo* studies. The most widely studied biological structures in tissues that produce endogenous SHG signal are based on collagen, muscle, and microtubules elementary structures. Furthermore, these elementary SHG scatterers, when excited with different incoming linear polarizations, provide a SHG response that is characteristic of the local scatterer orientation. This polarization dependent SHG (PSHG) technique has been used to interpret images taken from *C. elegans* muscles [14]. Furthermore, using PSHG imaging it is possible to determine the orientation, θ_{SHG}, and degree of organization, $\Delta\theta$, of the SHG elementary source (i.e. the hyperpolarizable molecule) inside the muscular tissue.

In this study we cut axons of *C. elegans* D-Type motoneurons using femtosecond unamplified MHz pulses and provide a new approach for a rigorous, detailed and more precise assessment of the collateral damage induced to the surrounding tissues. We present the use of a combination of linear and nonlinear high-resolution imaging techniques, all of them integrated in a single multimodal optical workstation to monitor any change induced to the tissues around the operated axon [15]. Damage to the cuticle produced with the femtosecond laser can be readily observed with transmitted light. At the same time, confocal microscopy is used to reveal minute collateral tissue damage that generates autofluorescence or produces any change in

the original fluorescence of the structures. Finally, previous laser axotomy works were relying on genetically modified worms expressing muscle fluorescence to assess the caused damage in this tissue [11]. In this paper we exploit the advantages offered by SHG to extract information of unlabeled muscular tissue. Furthermore, we present PSHG as a novel high-resolution contrast mechanism able to reveal laser axotomy inflicted molecular damage in the muscle of this model organism.

2.3 Materials and methods

2.3.1 The multimodal microscope

A multiphoton microscope was built around a commercial confocal (Nikon C1-Si) inverted microscope (Nikon Eclipse Ti-E [14], Nikon Inc., Japan) using a Kerr-lens mode-locked Ti:Sapphire oscillator (Coherent MIRA 900f) producing 150 fs (FWHM) pulses at a repetition rate of 76MHz. This microscope incorporate two independent pairs of galvanometric mirrors, one for continuous-wave visible laser (within scan head of Nikon C1-Si) and the other (placed externally) for the ultrashort pulsed laser. Both laser sources were coupled through 2 different input ports in such a way that both the confocal and multiphoton sections could work independently and simultaneously. This multimodal unit could, therefore, be used in the linear and nonlinear regime with a variety of different techniques working in a simultaneous way. In particular, the nonlinear input could be used for performing the axotomy while the confocal unit could be used to visualize axotomy and the collateral damage at the same time. For more details on the full capabilities of this set-up please see Mathew *et al*. [15].

2.3.2 Worm mounting

C. elegans were grown on nematode growth medium (NGM) agar plates using standard procedures [16]. To visualize the axons and to perform most of our axotomy studies we employed the transgenic strain juIs76 [unc-25::gfp] II that express GFP in D-type motoneurons. To confirm that SHG gives an equivalent/superior muscle damage information, when compared to fluorescence based methods, we employed the transgenic strain RP1: trIs10 [myo-3p::MB::YFP+myo-2p::YFP+ceh-23::HcRed+unc-25::DsRed+unc-129nsp::CFP. This strain expresses YFP (membrane anchored) in muscle cells. In both cases, the worm cultures were synchronized and

single L4 *larvae* were mounted on 2% agar pads with 0,8 μl of 10mM Levamisole (Dr. Ehrenstorfer) between two 170 μm glass slides. These were sealed with melted paraffin for sample stabilization.

In both cases, the worm cultures were synchronized and single L4 *larvae* were mounted on 2% agar pads with 0,8 μl of 10mM Levamisole (Dr. Ehrenstorfer)

2.3.3 Axotomy

Axotomies were performed on the commissures of the D-type motoneurons, on the most ventral/dorsal part of the axon just after its association with the cords (~1-5μm away). The position of the precise focal plane for cutting was found based on simultaneous TPEF and SHG imaging of the axon and the body wall muscles, respectively. This provided us with the anatomical references to finely adjust the position of the laser beam precisely at the axial center of the axon (see Figure 2.1). A different number of axotomies per worm (in different axons) were performed resulting in a total of sixty-one surgeries. Axotomies were performed by parking the tightly focused laser beam on the target point while controlling the irradiation time with an electronic shutter. For this work, the laser central wavelength was set to 868nm in order to optimize the imaging performance the system, without compromising the available laser power required for ablation. We employed an oil immersion 60x 1.4NA microscope objective that focuses the beam to a point spread function (PSF) of full-width-at-half-maximum (FWHM) dimensions of 0.45 μm transversal and 1.2 μm axial [17]. To find the appropriate laser power for cutting, the exposure time was set to 200 ms and the laser power was increased up to the value that led to an effective disruption of axons. This methodology yielded an optimal average power of 90mW (energy per pulse of 1.2nJ) which corresponds to a peak intensity of approximately $3x10^{12}W/cm^2$at the sample plane. The same power was used throughout the experiments.

2.3.4 Multimodal imaging for collateral damage assessment

It is important to determine if the axons are indeed severed and not simply photobleached and appear as a cut at the point of laser interaction (point of surgery). The following cues helped in determination of successful axotomy: a) retraction of

the axon; b) sealing and/or formation of bumps at the point of laser surgery and c) spilling of axoplasm [4][12]. Moreover, in order to confirm complete severing, we performed several axotomies on GFP labeled ASJ neurons followed by DiI staining (data not shown) [18].

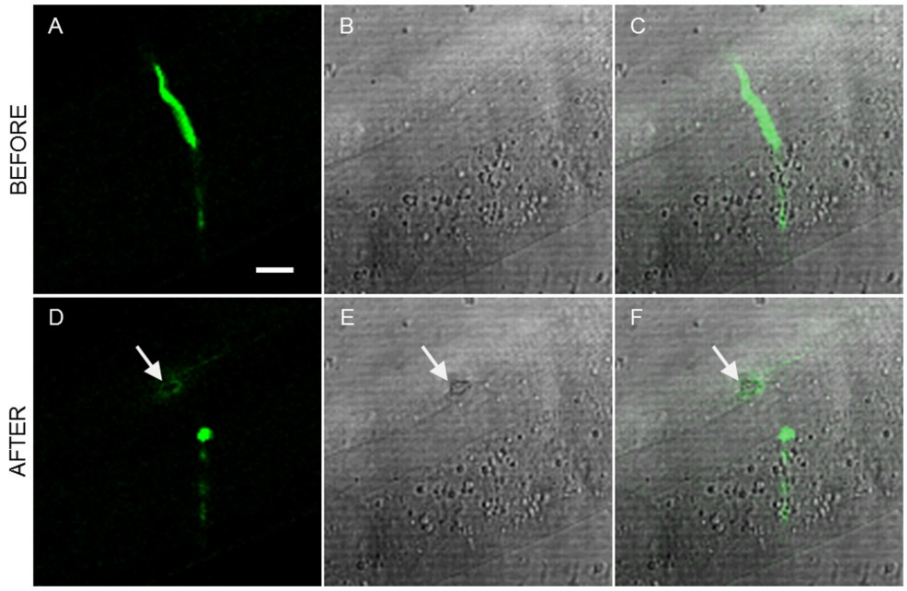

Figure 2.2: Damage assessment using linear imaging techniques.
a) Confocal, b) transmitted light and c) combined images of the region surrounding the axon before the laser dissection. d–f) show the same region after the surgery. Damage is evidenced by increased autofluorescence in the confocal image and a dark spot in the transmitted light image. Both damage structures colocalize at the combined image. Excitation of the GFP labeled neurons was done at 488 nm. Arrows point to the place of the laser axotomy. Scale bar 10 µm.

Our collateral damage assessment methodology relies on the visualization of the tissues surrounding the dissected axon. The following collateral damage scenarios can be detected: a) Damage to the cuticle is easily observable form the laser-scanned transmitted light microscopy images; b) Any collateral tissue damage, both in the cuticle or in the muscle can potentially be detected by looking out for localized increase in autofluorescence around the point of laser interaction using the confocal microscopy images; c) to have an even better determination of the collateral damage to muscle, SHG microscopy of the muscle tissues could be employed. It may be noted that all the three imaging modalities (laser transmitted , confocal and SHG) is done using the same instrument that performs the laser surgery.

In the following description we present the detailed depiction of the methodology used for the damage assessment. First, the area surrounding the point of surgery was

imaged pre-surgically using TPEF and SHG microscopy. The axotomy was then performed using custom-made software that allows us to select the point on the axon to be dissected using the TPEF image. The surgical procedure was recorded while being performed using confocal and transmitted light microscopy to help observe the effective dissection of the axon as well as any dynamical effect that provide information about collateral damage. Immediately after the surgical procedure, a second set of nonlinear (TPEF and SHG) images were taken, at several focal planes around the point of surgery, to correct for any changes in the focal plane over the tissue relaxation time. Finally, worms presenting axotomies that do not show clear collateral damage were selected to be imaged with PSHG microscopy [19]. In this case if there is any change in the myosin structure caused by the laser tissue interaction the PSHG technique could potentially reveal it.

In order to characterize the level of damage that can be reported with the PSHG technique, a series of experiments using worms expressing YFP in the body wall muscles were used (9 worms). This enabled to observation of fluorescence, SHG and PSHG images from the same axotomized region of interest (ROI).

2.4 Results

Sixty-one axons were laser cut and simultaneously imaged using confocal microscopy, 56 of the 61 operated commissures were successfully severed. The inflicted collateral damage was determined using different imaging techniques using our multimodal optical workstation. Figure 2.2 shows the typical example of a laser axotomy and the high resolution imaging approach for the visualization of collateral damage. Figure 2.2 (a-c) and (d-f) show confocal and transmitted light images before and after the axotomy, respectively. The post-surgical confocal image, Figure 2.2(d), reveals a circular pattern of autofluorescence that is generated around the point of surgery, which indicates that some collateral damage is induced to the close-by tissue. In addition this damage is also evidenced by a clear retraction of the axon tips in the laser axotomy region [4]. Moreover, the dark spot evidenced in the post-surgical transmitted light image (in Figure 2.2(e)) clearly indicates that the damage was induced in the cuticle. As expected, both observed damage patterns colocalize over the same region as can be seen in Figure 2.2(f).

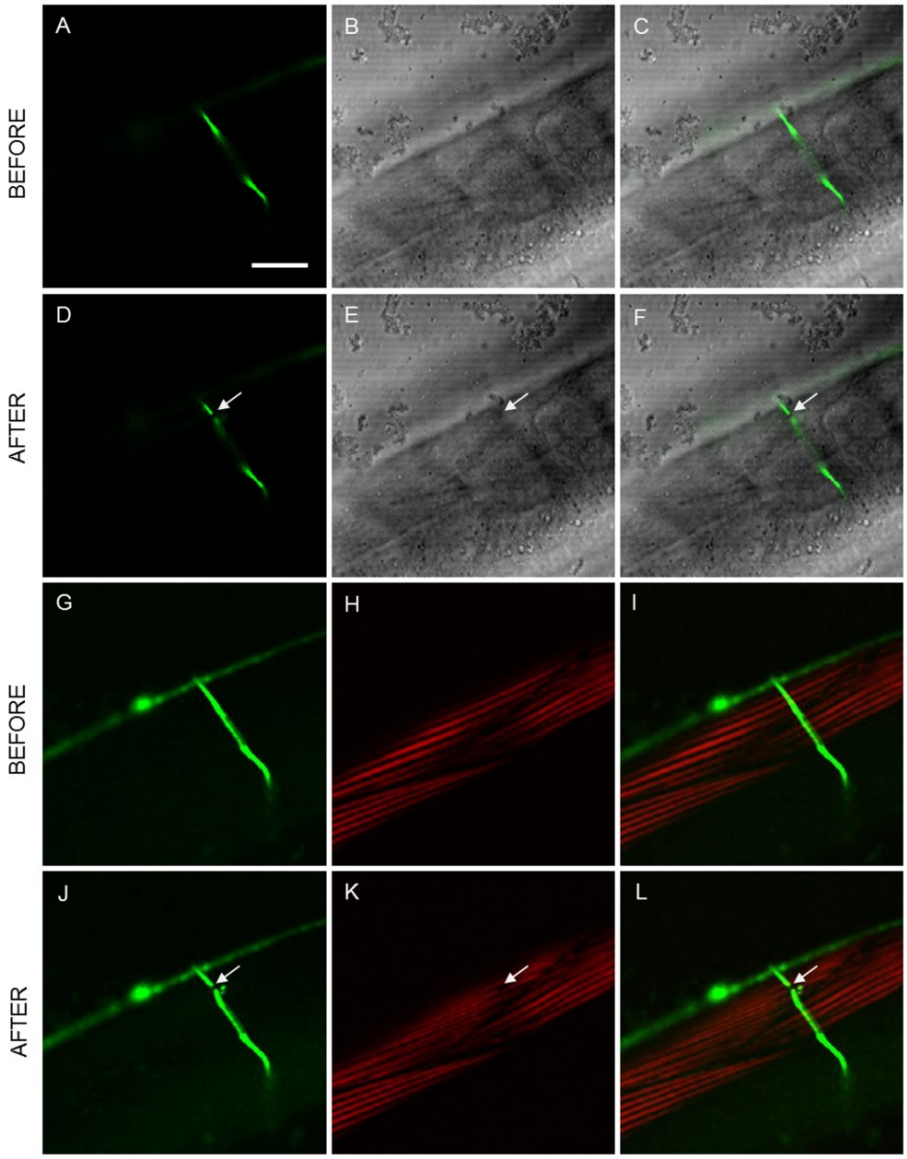

Figure 2.3: Collateral damage assessment using linear and nonlinear imaging techniques.
Linear: a) confocal, b) transmitted light and c) combined images of the region surrounding the axon before the laser dissection; d–f) show the same region after the surgery. Nonlinear: g) TPEF, h) SHG and i) combined images before the laser dissection; j–l) show the same region after the surgery. No collateral damage was observed in CFM while damage in muscle is evidenced with SHG microscopy. Arrows point to the place of the laser axotomy. Scale bar 20 µm.

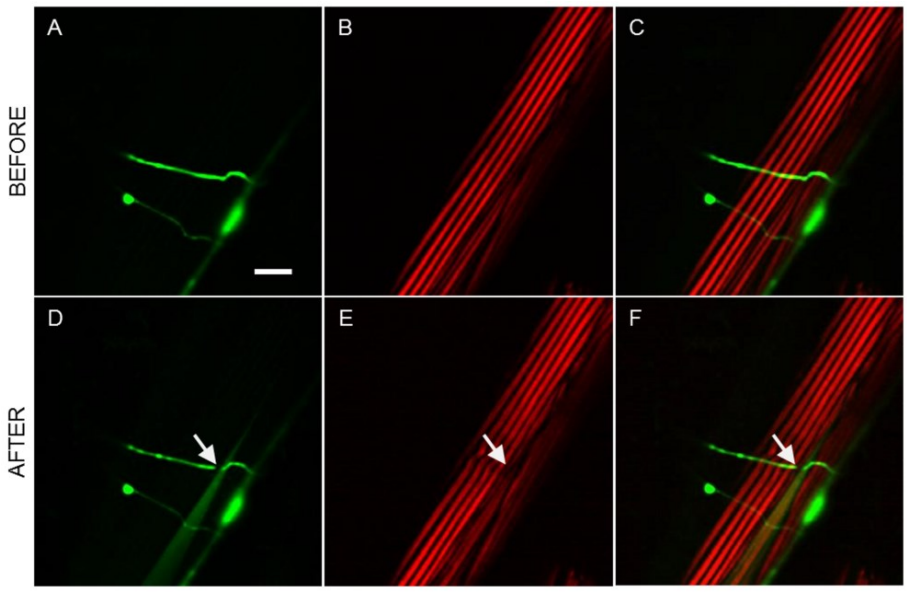

Figure 2.4: Laser-induced changes induced to the muscle visible with SHG imaging.
a) TPEF, b) SHG, and c) combined images before the dissection; d–f) show the same region after the surgery. Arrows point to the place of the laser axotomy. Scale bar 10 µm.

Post-surgical nonlinear imaging using combined simultaneous TPEF and SHG microscopy further aided in determination of collateral damage. Figure 2.3 shows a complete multimodal imaging performed at the region closer to the axotomy. Figure 2.3 (a-c) and (g-i) show the multimodal images taken before axotomy, whereas Figure 2.3 (d-f) and (j-l) are the resulting images after the procedure. In this case, no collateral damage is observed either in the confocal image, Figure 2.3(d), or in the TPEF image, Figure 2.3(j). Minimum collateral cuticle damage is observed in the laser transmitted image, Figure 2.3(e). The surgical tool has made an efficient cut in the axon, with minimum damage to the cuticle, however, changes have been induced to the muscle as can be observed in the Figure 2.3(k): reduction of the SHG signal in a small region around the dissection point and transition from Single-Band to Double-Band (SB to DB) signal structure of the muscle sarcomeres. This clearly illustrates the power of multimodal imaging (Confocal+ Laser-transmitted +TPEF+SHG) in making a thorough assessment of collateral damage.

There were a number of cases where no apparent collateral damage is observed using the linear and nonlinear fluorescent techniques. However, a slight “distortion” of muscle (not actual damage) could be observed in the SHG images of muscle. These distortions were in the form of either a slight reduction in the SHG signal from the

muscles surrounding the region of surgery or a wavy-like appearance in the muscles. Such a case is shown in Figure 2.4 where, after axotomy, the muscle below exhibits wavy appearance without any actual loss of SHG signal in the muscle.

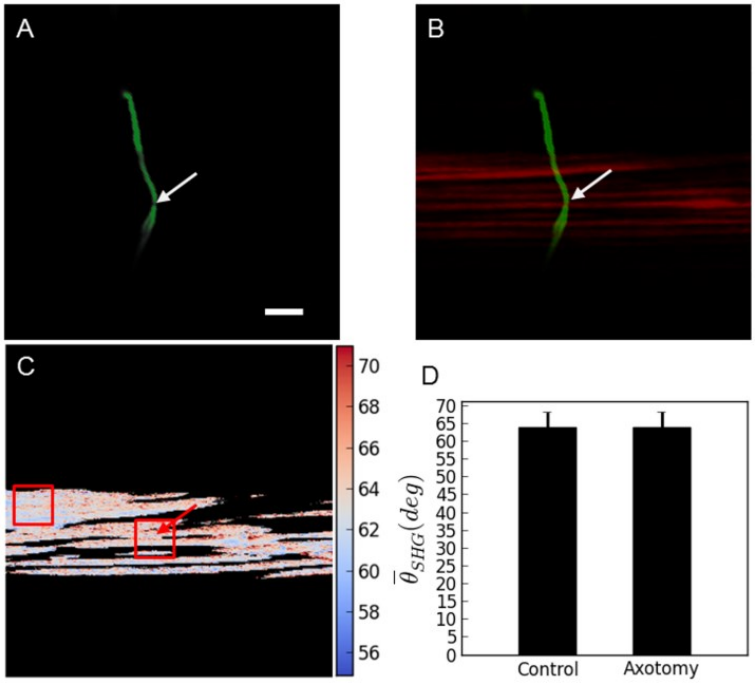

Figure 2.5: PSHG microscopy for the damage assessment after the axotomy. a) TPEF reveals a successfully cut axon. b) SHG signal from body wall muscle do not change after the surgery; c) Post-surgical pixel-resolution mapping of myosin θ_{SHG} at the muscle obtained from PSHG (color bar in degrees); d) θ_{SHG} (mean±1 standard deviation) for the muscles in the region surrounding the cut and in the control region (red squares). The control region was selected in the intact adjacent muscular cell far away from the axotomy. Unpaired two tailed t-test (n = 200 pixels for both sets) yields p>0.05 meaning that θ_{SHG} mean is not significantly different between the two regions. Arrows point to the place of the laser axotomy. Scale bar 10 µm.

When the femtosecond laser tool is properly tuned and perfectly focused at the center of the axon, incisions can be induced without any collateral damage. One such case (out of 12) is shown in Figure 2.5(a-b). TPEF evidenced that the axon is effectively severed whereas SHG image and PSHG analysis suggests that no damage was induced to the muscle. In these particular cases, where no damage was observed (with any of the above mentioned linear- and nonlinear imaging techniques), PSHG was performed to display the orientation of the hyperpolarizable molecule in myosin θ_{SHG}. This was performed at a pixel level, as can be seen in the Figure 2.5(c). Unpaired two tailed *t*- test on these data shows that there are no significant

differences in the mean value of θ_{SHG} between the area surrounding the axotomy and the intact muscle well apart from the axotomy, Figure 2.5(d). This means that no damage could be detected even at the level of the myosin structure of the muscles.

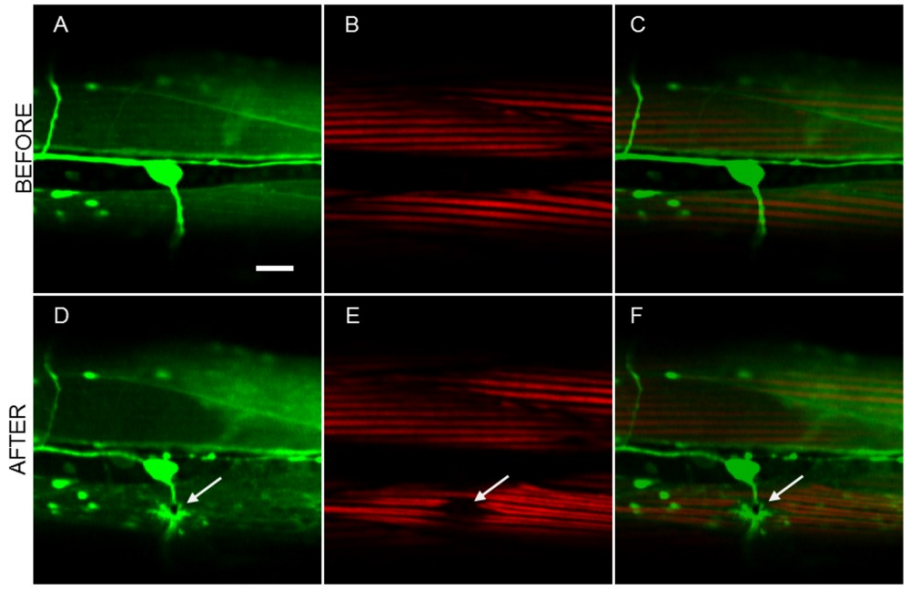

Figure 2.6: Comparison between SHG and fluorescence for the muscle damage assessment after the axotomy, large collateral damage.
Before the axotomy: a) TPEF images of YFP marked muscles and axons; b) SHG signal of the same muscles; and c) merge of TPEF and SHG images for comparison. Post-surgical images: d) TPEF and e) SHG images showing the laser damage hat is evident over a larger region. c) Shows a merged TPEF and SHG images for comparison. Arrows point to the place of the laser axotomy. Scale bar 10 µm.

The characterization of the damage that can be reported with the SHG technique was compared with a series of experiments using worms expressing YFP in the body wall muscles. To be able to properly target the neurons with the laser, the worms were also expressing CFP in the axons. In all these cases fluorescence, SHG and PSHG were addressed in the same axotomized region of interest (ROI). Firstly, a large collateral damage, evidenced by a fracture of a thick filament fiber was produced. Here, as expected, the lack of fluorescence and/or SHG signal are enough to reveal damage (see Figure 2.6). Notice that, as shown before [11], other strains with different muscle labelling strategies could be equally used for this same purpose.

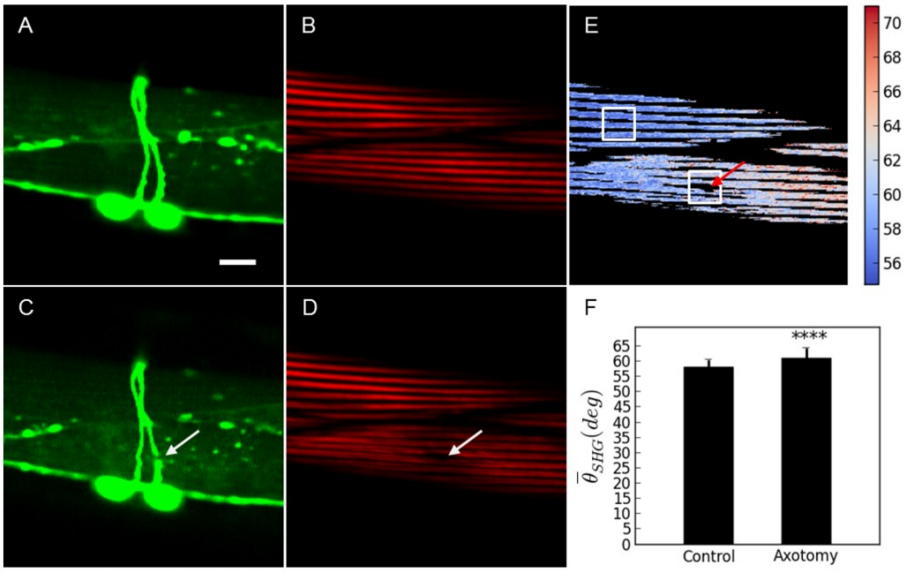

Figure 2.7: Comparison between PSHG and fluorescence for the muscle damage assessment after the axotomy, medium collateral damage.
Before the axotomy: a) TPEF image of YFP marked muscles and axons; b) SHG image of the muscles in the same region. After the axotomy: c) TPEF reveals a successfully cut axon showing a gap that interrupts the continuity of the axon. No other damage is apparent; d) SHG image of the body wall muscle shows the change from SB to DB structure of the sarcomeres. PSHG analysis: c) Post-surgical pixel-resolution mapping of θ_{SHG} at the muscle (color bar in degrees); d) θ_{SHG} (mean±1 standard deviation) for the muscles in the region surrounding the cut and in the control region (white squares). The control region was selected in the adjacent muscular cell far away from the axotomy. Unpaired two tailed *t*- test (n = 200 pixels for both sets) yields $p<0.001$ (****) meaning that θ_{SHG} mean is significantly different between the two regions. Arrows point to the place of the laser axotomy. Scale bar 10 μm.

Then, a reduced collateral damage in which no evident muscle fiber is broken was selected. In this case, TPEF from the axons (CFP labeled) reveals a successfully cut showing a gap that interrupts the continuity of the axon. However, fluorescence from the muscle (YFP labeled) structure does not reveal any collateral damage. In contrast, SHG imaging shows, as in Figure 2.3, the appearance of Double-Band structure in each of the thick filaments around the axotomized region (see Figure 2.7).

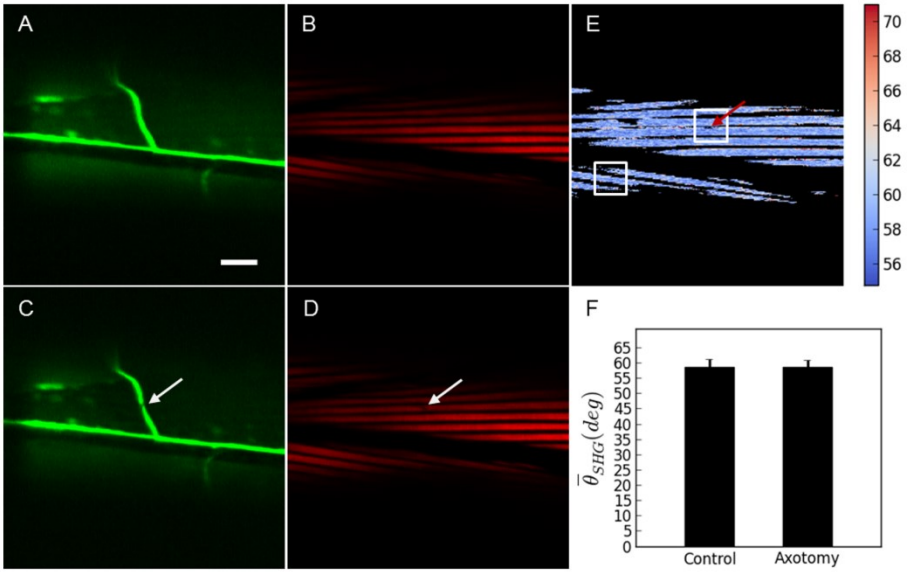

Figure 2.8: Comparison between PSHG and fluorescence for the muscle damage assessment of after the axotomy, minimum collateral damage.
Before the axotomy: a) TPEF image of YFP marked muscles and axons; b) SHG image of the muscles in the same region. After the axotomy: c) TPEF reveals a successfully cut axon, in the shape of a gap that interrupts the continuity of the axon, but no other damage is apparent; d) SHG image of the body wall muscle shows a small signal decrease at the targeted point on the axon. No other change or structural transformation is evident. PSHG analysis: c) Post-surgical pixel-resolution mapping of myosin θ_{SHG} at the muscle (color bar in degrees); d) θ_{SHG} (mean±1 standard deviation) for the muscles in the region surrounding the cut and in the control region(white squares). The control region was selected in the adjacent muscular cell far away from the axotomy. Unpaired two tailed t- test (n = 200 pixels for both sets) yields $p>0.05$ meaning that θ_{SHG} mean is not significantly different between the two regions. Arrows point to the place of the laser axotomy. Scale bar 10 µm.

Upon analysis with the PSHG technique (unpaired two tailed *t*- test (n=200 pixels for both sets)) we found that the region around the axotomy revealed significant differences ($p<0.001$ (****)) when compared to an intact sarcomere region. Finally, we proceed to analyze a region where TPEF from the axons (GFP labeled) reveals a successfully cut axon, in the shape of a gap that interrupts the continuity of the axon, but no other damage is apparent. Here a highly confined (within a few pixels) decrease of SHG signal near the axotomized neuron was observed (see Figure 2.8). In this case, there was no Double-Band structure being produced and our PSHG analysis (unpaired two tailed *t*- test (n=200 pixels for both sets)) did not find any significant difference ($p>0.05$) with intact tissue. This suggests that no damage has been produced or that this has been propagated in a negligible way after the axotomy procedure, as it is the case of Figure 2.5.

Table 2.1: Successful axotomies and associated damage assessment techniques.

<table>
<tr><td rowspan="5">Experiments

61</td><td rowspan="5">Successful axotomies

56</td><td rowspan="2">NO apparent damage

12</td><td>PSHG: revealed NO Myosin modification

3</td></tr>
<tr><td>PSHG: Revealed myosin modification

9</td></tr>
<tr><td rowspan="3">Damaged

44</td><td>Confocal, TPEF: damage is revealed through autofluorescence

33</td></tr>
<tr><td>Transmitted light: observation of long lasting bubbles in the cuticule

4</td></tr>
<tr><td>SHG: lack of the characteristic SHG signal in muscle due to fiber disruption

44</td></tr>
</table>

Table 2.1 summarizes the total number of successful axotomy experiments and the techniques used for the damage assessment. The potential structural damage on the muscle cells in the "NO apparent damage" set of results could only be done with PSHG imaging. This means that the 9 experiments that show disruption of the SHG signal, and potential damage in the muscular nano-organisation, would have been overseen without the use of this technique.

2.5 Discussion

In this study we employed a MHz femtosecond laser oscillator to precisely sever axons of *C. elegans* D-type motoneurons. The axotomies were recorded in real-time (i.e. during the axotomy process) using a set of linear and nonlinear imaging techniques implemented in a multimodal microscopy workstation. Pre- and post-surgical high resolution images were used to further assess the collateral damage caused to the surrounding tissues. TPEF and SHG provided the anatomical

references to precisely locate the laser spot on the target axon. SHG and PSHG microscopy were used *a posteriori* to determine the collateral damage inflicted to the muscle whereas laser transmitted was used for the damage assessment of the cuticle.

Laser axotomy and multimodal imaging were performed on 61 different axons. Of these, 56 resulted in a successful cut, with or without some degree of collateral damage. As we set the power of the laser close to the threshold for axon cutting, smaller and more confined collateral damage was produced. The typical sizes of collateral damage ranged between 1 and 3 microns if fluorescence was used for the assessment (with some exceptions as the one in the Figure 2.6 that extended over 10 microns). SHG images reported damages from small punctures sizing less than a micron up to 10 microns when the sarcomere fibers were cut (see Figure 2.6). In both cases the lower limit of detection is given by the resolution limit of the employed methods (close to 0.5 microns in confocal, TPEF and SHG).

The variation in induced damage is inherent to the fact that the technique is applied to a biological sample. Each worm used in the experiments, although carefully selected and synchronized, is different and can be positioned in different ways, causing, therefore, different types of errors and different degrees of efficiency of the cut (and induced damage).

This is also why an efficient and versatile tool for collateral damage detection is needed. By the use of our multimodal imaging tool we were able to identify that in ~20% of the cases (12 neurons) no collateral damage whatsoever could be detected. It is interesting to note that by using only increased autofluorescence (widely accepted metric) as an indicator of damage, this number would have been ~54% (33 neurons). In such a case, this would not account for the minute damage produced along the axial extension of the focused beam and, therefore, its effects in the cuticle and/or the body wall muscles that do not show up as autofluorescence.

Previous collateral damage studies have been done based on: i) axonal regeneration speed and efficiency [5][12], ii) distance between the sealed axon endings and monitoring of the muscle damage using a fluorescence reporter [11] and iii) the behavioural mechanism associated with a certain kind of neurons [20]. Methods that rely only on the generation or the suppression of the fluorescence do not discriminate

between different tissues and can be affected by other fluorescent phenomena associated to the axotomy, such as axoplasm spilling and autofluorescence generated by stimulation of the cells [4]. The other methods, however, do not provide a direct visualization, do not detect minute collateral damage caused to the surrounding tissues nor are strong and robust indicators of the induced cut (such is the case of the distance between sealed axons as this varies with natural retraction of the axon tips during surgery).

Likewise, in regeneration studies, the effectiveness of functional reconnection of both axon endings could also be biased by having damage in the surroundings of the axons and possibly interfering with media guidance cues. On the other hand, the methodology here described results in a precise way for assessing this damage that is independent from any post-surgical factors. It includes a stringent quantitative criteria based on observation of the several indicative factors of collateral damage such as i) induced autofluorescence in the borders of the target area or in neighboring tissues, ii) cuticle damage, iii) muscle modification and iv) cavitation bubbles. This could be used in a wide range of biological applications in which *in vivo* damage assessment after laser nano-surgery is required, including neuronal regeneration studies.

Furthermore, in this work we have introduced, for the first time, the SHG imaging technique for determining collateral muscle damage after axon surgery. SHG/PSHG allows inferring the muscular structures at the molecular level (myosin) [21][22] and has, therefore, the potential to reveal minute collateral damages to the muscle. Although the relevance of these minute damages is not obvious for the axon regeneration process, this study presents a quantitative method that would allow a proper assessment of such influences.

In our experiment we have observed several different changes induced to the muscles: punctures in the muscle, reduction in SHG signal and change of the muscular fibre structure. Punctures are the result of direct collateral damage induced to the muscle mediated by the same physical mechanisms responsible of the axon dissection. In the case of a reduction of the SHG signal with no transition from SB to DB, our PSHG analysis revealed that there is no damage of the muscle at the myosin

level (as this is the molecule generating the SHG signal). On other hand, when SB to DB conversion happens, this can be easily quantified with the PSHG technique. This suggests that there is an important impact on the myosin structure due to the axotomy.

Finally, structural changes such as a wave-like pattern appearance and SB to DB conversion have been seen to also occur together with a strong stretch/contraction of the muscle [4]. Previous studies have related the change from SB to DB pattern to chemical degradation of *ex vivo* samples [23] and laser induced photo-damage [24]. In this work, we employed living *C. elegans*, indicating that this conversion is not related to fixation chemicals. Also, the laser powers employed for non-linear imaging were set to the level considered safe [25]. Therefore, both simultaneous SB to DB conversion and wave-like pattern formation can be seen as a side effect of the localized high-power laser irradiation employed to cut the axons.

Our results show that femtosecond pulses from our mode-locked laser oscillator can be effectively used to perform high precision neuron surgery *in vivo* with controlled collateral damage. The beam had an average power of 90mW (an energy per pulse of 1.2nJ) which are focused with an objective lens of 1.4 NA. This corresponds to a peak intensity of approximately $3x10^{12}W/cm^2$. Under these conditions, the ablation is mediated by dissociative effects of the generated low plasma density, in conjunction with photochemical effects into the irradiated volume. It was shown that in this regime, smooth nanometer-scale dissections can be obtained [1][26][27]. Moreover, we can assume that the maximum damage is confined to the volume where the plasma is created. In our case, considering the theoretical estimations of the PSF of the focused beam with our experimental parameters we obtained a plasma distribution with dimensions 222 nm transversal and 613 nm axial. Therefore, even if the laser is perfectly focused at the axial center of the axon, damage in either cuticle or body wall muscles is expected, as can be seen in Figure 2.1. Furthermore, a small mistake on the axial positioning of the laser scalpel will be revealed as an increased damage whether in the muscle or in the cuticle. Fortunately, our method is capable to detect and account for any of these effects by using the proposed multimodal damage assessment technique.

2.6 Conclusion

This study shows that femtosecond pulses from a mode-locked laser oscillator can be effectively used to perform high precision nanosurgery and provides an alternative approach for a practical and comprehensive damage assessment. This method has the potential to be used in most neuronal structures in *C. elegans* since there are many cases where different neuronal processes (not only axons but also dendrites) have neighboring muscles and cuticle. Most head neurons in *C.elegans* such as the sensory neurons, for instance, that make up a high percentage of the neurons in this model organism that are thoroughly used for behavior studies, are highly attractive candidates due to their strategic position around the pharynx, a big muscular structure that can be easily visualized using SHG microscopy. The application of the above mentioned techniques can be extended to other biosamples containing different endogenous sources of SHG (myosin, collagen, microtubules, etc.). The use of combined imaging techniques in one imaging set-up is an unconventional approach to *in vivo* studies of different structures and tissues that can prove to be an extremely valuable tool to the examination of induced damage by laser surgery tools.

Experiments from Figure 2.2 to Figure 2.4 were carried out by Manoj Mathew and are included here for completeness.

2.7 References

1. A. Vogel, J. Noack, G. Hüttman, y G. Paltauf, "Mechanisms of femtosecond laser nanosurgery of cells and tissues," Appl. Phys. B **81**, 1015-1047 (2005).

2. J. Baumgart, K. Kuetemeyer, W. Bintig, A. Ngezahayo, W. Ertmer, H. Lubatschowski, y A. Heisterkamp, "Repetition rate dependency of reactive oxygen species formation during femtosecond laser-based cell surgery," J. Biomed. Opt. **14**, 054040 (2009).

3. A. Thayil, A. Pereira, M. Mathew, D. Artigas, E. Blanco, y P. Loza-Alvarez, "Decrease in laser ablation threshold for epithelial tissue microsurgery in a living Drosophila embryo during dorsal closure," J. Microsc. **232**, 362-368 (2008).

4. S. I. C. O. Santos, M. Mathew, y P. Loza-Alvarez, "Real time imaging of femtosecond laser induced nano-neurosurgery dynamics in C. elegans," Opt. Express **18**, 364-377 (2010).

5. M. Yanik, H. Cinar, H. Cinar, A. Chisholm, Y. Jin, y A. Ben-Yakar, "Neurosurgery - Functional regeneration after laser axotomy," NATURE **432**, 822-822 (2004).

6. C. Gabel, H. Gabel, D. Pavlichin, A. Kao, D. Clark, y A. Samuel, "Neural circuits mediate electrosensory behavior in Caenorhabditis elegans," J. Neurosci. **27**, 7586-7596 (2007).

7. D. Clark, D. Biron, P. Sengupta, y A. Samuel, "The AFD sensory neurons encode multiple functions underlying thermotactic behavior in Caenorhabditis elegans," J. Neurosci. **26**, 7444-7451 (2006).

8. D. Clark, C. Gabel, T. Lee, y A. Samuel, "Short-term adaptation and temporal processing in the cryophilic response of Caenorhabditis elegans," J. Neurophysiol. **97**, 1903-1910 (2007).

9. S. Chung, D. Clark, C. Gabel, E. Mazur, y A. Samuel, "The role of the AFD neuron in C. elegans thermotaxis analyzed using femtosecond laser ablation," BMC Neurosci. **7**, 30 (2006).

10. "WormAtlas," http://www.wormatlas.org/.

11. M. F. Yanik, H. Cinar, H. N. Cinar, A. Gibby, A. D. Chisholm, Y. Jin, y A. Ben-Yakar, "Nerve Regeneration in Caenorhabditis elegans After Femtosecond Laser Axotomy," Sel. Top. Quantum Electron. IEEE J. Of **12**, 1283-1291 (2006).

12. F. Bourgeois y A. Ben-Yakar, "Femtosecond laser nanoaxotomy properties and their effect on axonal recovery in C. elegans," Opt. Express **15**, 8521-8531 (2007).

13. S. V. Plotnikov, A. C. Millard, P. J. Campagnola, y W. A. Mohler, "Characterization of the Myosin-Based Source for Second-Harmonic Generation from Muscle Sarcomeres," Biophys. J. **90**, 693-703 (2006).

14. S. Psilodimitrakopoulos, S. I. C. O. Santos, I. Amat-Roldan, A. K. N. Thayil, D. Artigas, y P. Loza-Alvarez, "In vivo, pixel-resolution mapping of thick filaments' orientation in nonfibrilar muscle using polarization-sensitive second harmonic generation microscopy," J. Biomed. Opt. **14**, 014001 (2009).

15. M. Mathew, S. I. C. O. Santos, D. Zalvidea, y P. Loza-Alvarez, "Multimodal optical workstation for simultaneous linear, nonlinear microscopy and nanomanipulation: Upgrading a commercial confocal inverted microscope," Rev. Sci. Instrum. **80**, 073701 (2009).

16. S. Brenner, "The Genetics of Caenorhabditis Elegans," Genetics **77**, 71-94 (1974).

17. S. Grill y E. H. K. Stelzer, "Method to calculate lateral and axial gain factors of optical setups with a large solid angle," J. Opt. Soc. Am. A **16**, 2658-2665 (1999).

18. S. Shaham (ed.), "Methods in cell biology," (2006).

19. S. Psilodimitrakopoulos, V. Petegnief, G. Soria, I. Amat-Roldan, D. Artigas, A. M. Planas, y P. Loza-Alvarez, "Estimation of the effective orientation of the SHG source in primary cortical neurons," Opt. Express **17**, 14418-14425 (2009).

20. S. Chung, D. Clark, C. Gabel, E. Mazur, y A. Samuel, "The role of the AFD neuron in C. elegans thermotaxis analyzed using femtosecond laser ablation," BMC Neurosci. **7**, 30 (2006).

21. S. Psilodimitrakopoulos, D. Artigas, G. Soria, I. Amat-Roldan, A. M. Planas, y P. Loza-Alvarez, "Quantitative discrimination between endogenousSHG sources in

mammalian tissue, based ontheir polarization response," Opt. Express **17**, 10168-10176 (2009).

22. P. J. Campagnola y L. M. Loew, "Second-harmonic imaging microscopy for visualizing biomolecular arrays in cells, tissues and organisms," Nat Biotech **21**, 1356-1360 (2003).

23. G. Recher, D. Rouède, C. Tascon, L.-A. D'Amico, y F. Tiaho, "Double-band sarcomeric SHG pattern induced by adult skeletal muscles alteration during myofibrils preparation," J. Microsc. **241**, 207-211 (2011).

24. G. Recher, D. Rouède, E. Schaub, y F. Tiaho, "Skeletal muscle sarcomeric SHG patterns photo-conversion by femtosecond infrared laser," Biomed. Opt. Express **2**, 374-384 (2011).

25. K. König, "Cell Damage During Multi-Photon Microscopy," en *Handbook Of Biological Confocal Microscopy*, J. B. Pawley, ed. (Springer US, 2006), pp. 680-689.

26. K. Kuetemeyer, R. Rezgui, H. Lubatschowski, y A. Heisterkamp, "Mechanisms of femtosecond laser cell surgery in the low-density plasma regime," Proc. SPIE **7897**, 789704-789704-5 (2011).

27. S. Kalies, K. Kuetemeyer, y A. Heisterkamp, "Mechanisms of high-order photobleaching and its relationship to intracellular ablation," Biomed. Opt. Express **2**, 805-816 (2011).

Chapter 3: Towards a reliable and simple device for axon regeneration screening for applications in drug testing: preliminary results on Citicoline

3.1 Introduction

In the last chapter, a method to obtain highly localized femtosecond laser ablation that can be used to dissect single nerve fibers within the body of a *C elegans* was presented. When properly optimized (using multimodal microscopy) this method induce minimum damage to the tissues surrounding the cut axon. Particularly, when cutting D-type motoneurons it was shown that damage can be controlled even at the level of the molecular structure of the myosin of the muscle cells adjacent to axon [1]. Yanik *et al*. were the first to demonstrate femtosecond laser surgery in *C. elegans* dissecting axons within the body of the worm [2]. They have found that by dissecting the entire set of the D-type motorneurons worms lose the ability to move backwards. Chung *et al*. performed experiments snipping thermosensory neurons [24]. They found that cutting the dendritic branch of these neurons was equivalent to killing the entire neuron, confirming that the thermosensory apparatus is localized in the dendritic tip. In the same experiment, they showed also, that cutting individual nerve fibers within the dendritic bundle apparently do not affect the adjacent processes close as 500 nm away. Detailed analysis of neuron interaction such as the above example, demonstrates the power of single cell femtosecond laser dissection within the simple neural system *of C. elegans*. Most importantly, Yanik *et al*. found that after some time, some of the severed neurons were able to regrow the cut axons and restore the nerve function [2]. These seminal findings opened up a new range of possibilities for exhaustive genetic and molecular studies of *in vivo* neuronal regeneration. Some of these studies are based on the use of mutant worms lacking their normal neuronal regenerative ability. This has resulted in the identification of the role of several genes in regeneration [3,4]. In spite of all this, the essential question of this biological model is if it is relevant as compared to human biology. A direct comparison between the different mechanisms leading to axon regeneration in *C. elegans* and those in vertebrate models is still not possible because these mechanisms are not well understood. Fortunately, some factors that regulate axon

regeneration in *C. elegans* have been found to play similar roles in vertebrate neurons [5]. Then, this model organism would become an important tool to identify the conserved mechanisms of axon regeneration. Among the multiple applications of this model, chemical screening for drug testing and is one of the most promising. Particularly, the screening of molecules that can enhance axon regeneration in *C. elegans* could be the first step in the development of new therapies for the treatment of brain injury and degenerative diseases in humans.

Citicoline, or, cytidine diphosphate-choline (CDP-Choline) is a small molecule that is an essential intermediate in the biosynthesis of structural phospholipids of cell membranes [6]. Different studies have shown its many benefits for medical uses. Beneficial effects have been reported in various central nervous system injury models and neurodegenerative diseases [7]. Other studies have reported the neuroprotective effects of Citicoline such as the prevention of neuronal degeneration [8], the prevention of memory impairment [9] and the enhancement of the cognitive performance of healthy subjects [10]. In contrast, recent studies pointed out that Citicoline is not efficacious in the treatment of moderate-to-severe acute ischemia in humans [11]. Despite these many studies, the exact mechanisms through which Citicoline operates are not fully understood. In order to better understand the effects of this drug at a cellular level, but still in a living, fully functional organism, we present the use of a very simple model of neuronal injury. This is done by performing laser axotomy in *C. elegans.* This will enable to study the effects of this small molecule in the process of axonal regeneration in the worm.

C. elegans is an organism model that is ideal for pharmaceutical testing. It is a sophisticated multicellular animal with many different organs and tissues: muscle, hypodermis, intestine, reproductive system, glands, and a nervous system. Also there is a large collection of mutants and large-scale high-throughput screening of many chemical species is enabled thanks to its prolific progeny yield. Besides, several studies revealed a strong conservation in molecular and cellular pathways between worms and mammals. Actually, comparison of the human and *C. elegans* genomes confirmed that the majority of human disease genes and disease pathways are present in *C. elegans* [12]. Nevertheless, *C. elegans* model has some important limitations. First, some molecular pathways are divergent between worms and humans, and

therefore cannot be studied. Secondly, these models do not recreate the complete physiology of the human cellular structures, limiting the reach of the obtained results [13]. Despite of these limitations, *C elegans* are the ideal tool to bridge the gap between *in vitro* and preclinical (mice) assays, providing a tool for fast and cost-effective high-throughput technologies.

In this work, we have built a device and developed a protocol to score the effects of Citicoline in the process of spontaneous axon regeneration of D-type motoneurons in *C elegans*. To our knowledge this is the first time Citicoline has been tested for neuroprotective effects in invertebrate animal models.

3.2 The microfluidic-based worm immobilization setup

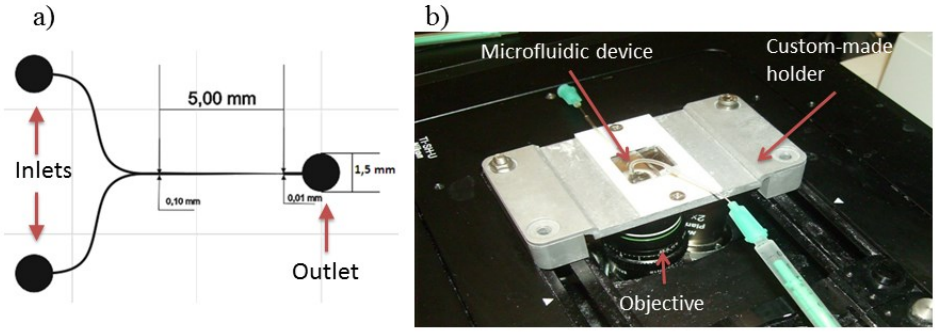

Figure 3.1: Design of the microfluidic-based immobilization setup.
Figure a) shows the original design in Corel Draw, and b) show the final microfluidic setup mounted on the microscope.

The high mobility of animals like *C. elegans* requires their immobilization for imaging and manipulation of cellular and sub-cellular features required for the different studies. This is normally done by combining mechanical pressure and the use of anaesthetics during the sample preparation [14]. In this approach, worms are picked form growth plates and put on a thin freshly prepared agar pad that is further enclosed and sealed between two cover glasses. Agar helps to distribute the pressure uniformly along the worm body and keeps the sample hydrated. Usually the movements of the worm are highly restricted just by making this preparation, but anaesthetics are employed if full immobilization is required. The problem of this preparation for repetitive, sequential or long-time measurements is that worms have to be removed from the preparation and mounted again for the next step, or for recovery stages. In this process worms are easily lost or injured during the sample

disassembly [15]. Additional problems may arise by the use of chemical anaesthetics such as sodium azide (NaN_3), levamisole and tricaine/tetrimisole. Side-effects of these products on are unknown, detrimental or uncharacterized [16,17]. Mainly due to these reasons, other approaches to restrain the movement of the worms were suggested. Immobilization by freezing or heating the worms [18,19], and using microbeads [20] are some of the more recent ideas. Other options available include various microfluidic lab-on-a-chip possibilities like compressing worms by air or CO2 [21,22]. These approaches made possible numerous applications for high-throughput screening using a variety of small animal models [23]. Microfluidic approach is very interesting as it permits to customize the design to the particular needs of each experiment. Here we produced a simple microfluidic device using soft lithography, to immobilize *C. elegans* in order to perform studies on axon regeneration.

3.2.1 Fabrication

Microfluidic devices were fabricated in polydimethylsiloxane PDMS (Sylgard 184, Down Corning) using soft-lithography techniques. The device was designed in Corel Draw™; chrome masks were prepared by Leicrom(Barcelona, Spain). Masters were fabricated on silicon wafers using SU8-25 (MicroChem) photoresist with 41, 56 and 68 μm tall features and treated with chlorotrimethylsilane. Masters were molded into PDMS with the ratio of polymer to cross-linker of 10:1. The devices were bonded to 170um glass cover slips via plasma bonding.

3.2.2 Design

The device has two inlets two for loading/unloading animals, and one outlet to empty the loading chamber (flushing outlet). The channel was chosen to decrease its width uniformly in width starting from 100 μm to 10 μm at the narrowest part. This will keep the nematode static before reaching the flushing outlet. The total length of the channel was set to 5mm. This design was inspired in an array of traps previously reported for parallel imaging and manipulation of *C. elegans* [24]. A custom-made device holder was fabricated in order to fit the microfluidic device to the multimodal microscope. This also helps to prevent the detachment of the PDMS form the glass while manipulating the device.

All inlets and outlets were cut with calibrated punchers. Fluids are delivered and withdrawn via Tygon tubing connected to the device with metal pins (Elveflow, Paris, France). Fluid manipulation is done using manual syringes. To keep/release the pressure on the channel, inlets and outlet can be manually open/close by using two way valves attached to the tygon tubing.

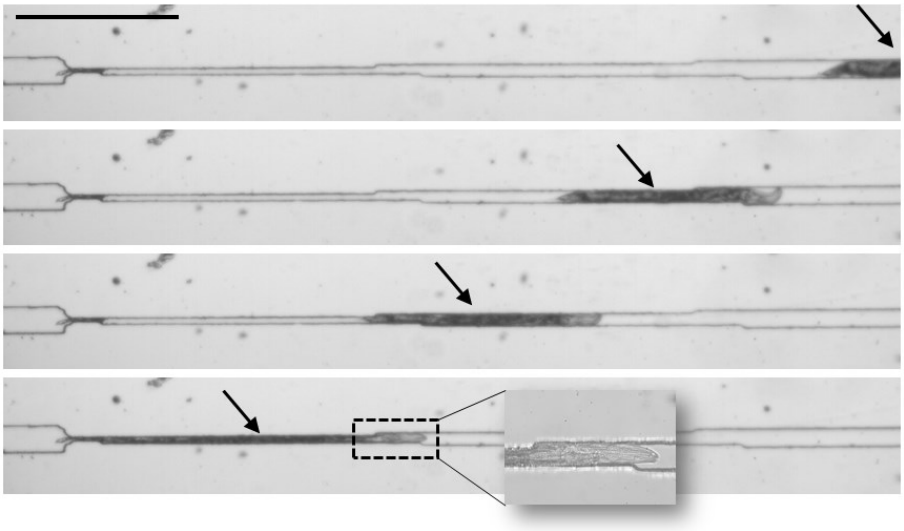

Figure 3.2: Sequence of immobilization of a worm within the microfluidic chip.
Several time frames showing how a worm gets immobilized within the designed microfluidic chip. Inset show a detail of head of the worm, that are free to move thanks to the stepped shape of the PDMS channel. Arrows show the position of the worm at every step. Scalebar : 1mm.

3.2.2.1 Operation of the chip

A solution containing young adult worms is prepared and loaded into a 100ml Eppendorf tube. Immobilization is performed in following steps. First, microfluidic device is loaded on to the microscope and the micro channel is brought to focus. This is done by using white light illumination and a camera attached to one of the microscope imaging ports. Then, M9 buffer is injected trough the outlet to pressurize and clean the channel for debris and air bubbles. When the channel is clean and free of bubbles some worms are loaded form the tube to a syringe and injected trough an inlet port. Pressure is carefully applied until a worm is observed within the field of view of the microscope. Once the worm reaches the narrower part of the trap the pressure is continuously decreased until a full immobilization is achieved. This normally happens when the channel is totally blocked and no more pressure can be applied with the syringe. If worm is still moving, negative pressure can be applied

form the outlet using a separate syringe. Finally, valves of inlets and outlet are closed to preserve the pressures inside the channel. Figure 3.2 show several frames of a sequence of worm immobilization using the aforementioned procedure. This figure also illustrates that the width of the channels decrease in discrete steps rather than continuously. This is because the resolution of the chrome masks employed to produce the SU-8 mold was not enough to reproduce the continuous ramp originally designed (Figure 3.1(a)).

Axon imaging and/or axotomy can be now performed if the worm is lying on the side where most of the axons are located, otherwise, imaging is affected by scattering and neurons could not be well visualized. In such case, the nematode is loaded back to the inlet tubing and discarded. Later, when the imaging /surgery is finished worm is carefully sucked out of the chamber using same syringe by following the worm with the camera. When the worm is already in the plastic tubing attached to the syringe, the metal pin is detached from the chamber and the worm is released to a plate of NGM for recovery.

3.2.3 Characterization of the device

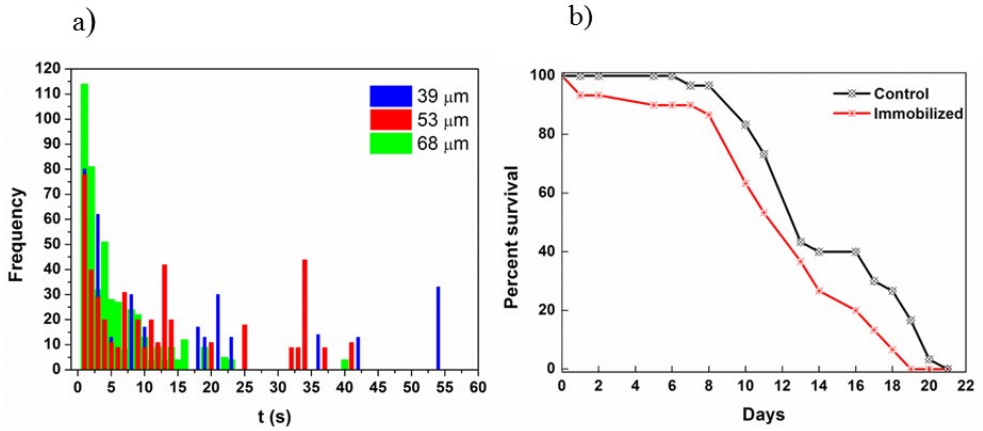

Figure 3.3: Characterization of the microfluidic immobilization device.
a) Frequency vs Duration of the time intervals where the worms remain still after being immobilized for three devices with different heights. Five worms were scored for movements during two minutes for each of the three devices. In b), lifespans of microfluidically-immobilized and control populations is shown. The mean lifespan of the immobilized population was 12.6± 4.6 days, and the mean lifespan of the control population was 14.6±4.0 days. The number of worms employed for both immobilized and control populations is 30.

Worms are immobilized in our trap by restraining their movements using a wedge-shaped channel. Besides, the observation of axon regeneration requires that worms

remain healthy after being immobilized. First, to assess the "trapping" capability of our microfluidic we measured the time intervals in which the worms remain still inside the channel during a total interval of two minutes. This is a time interval much longer than the required for axotomy, then we can evaluate the trapping capability in a wide window . We did this for devices with different channel heights to find the optimum value. Results are shown in Figure 3.3(a). As the average time required to perform the surgery is about 15s, according to the figure devices with of 53μm and 39μm height are suitable for our experiments, as they present movement-free intervals equal-or-longer than the required for axotomy. Nevertheless, we have observed that within the shorter channel worms look a bit over-squeezed even when they are in the wider 100μm section. Therefore, we kept the device with a channel of 53μm height for our experiments.

Second, we perform an experiment in order to evaluate the effects of the proposed immobilization in the lifespan of the worms. The results are shown in Figure 3.3(b). We found a slight decrease on the lifespan of the worms subjected to microfluidic inmobilization compared to the control, from 14.6 to 12.6 days. This would be related to the increased roughness of our devices that may affect the cuticle of some of them in their transit trough the narrower part of the channel. Small wounds to the cuticle has been reported before to reduce slightly (10%) the statistics of the lifespan of *C elegans* [25]. Besides of this, we consider that this minor reduction is negligible as compared to the potential damage to the animals and the high rate of incidental loss of animals related to the use of standard agar-anesthesia preparation.

3.2.4 Citicoline toxicity

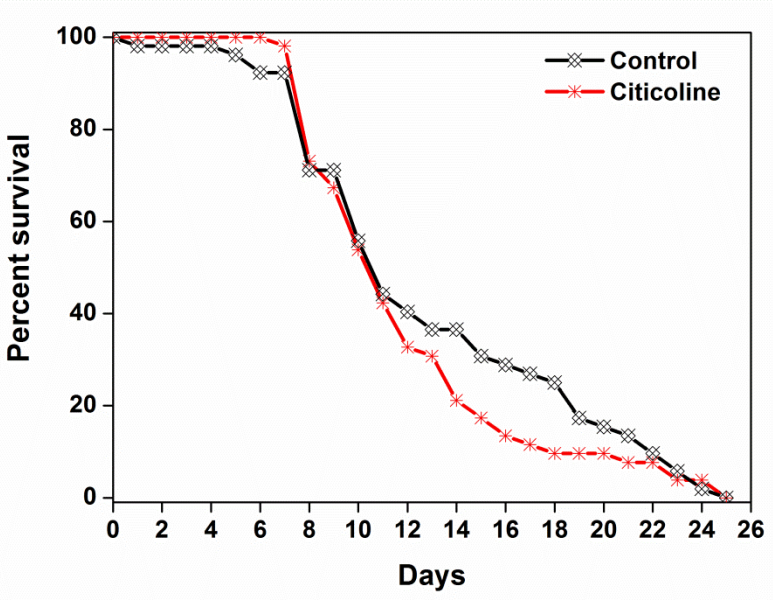

Figure 3.4: Citicoline toxicity assay on *C elegans*.
Lifespans of worms exposed to a high dose of Citicoline(200mg/ml) and control worms. The mean lifespan of the Citicoline-exposed population was 12.1± 4.6 days, and the mean lifespan of the control population was 13.0±5.8 days. The number of worms employed for both immobilized and control populations is 52.

Citicoline has been shown to have very low toxicity as well as very minor side effects in animals and humans [26]. On the other hand, to our knowledge, there are no studies of the effects of Citicoline in invertebrate models, particularly *C. elegans*. Besides, it is well known that the mode of penetration in these animals is a variable combination of limited diffusion through the cuticle and ingestion. *C. elegans* are surrounded by a thick cuticle that is a physical barrier to the penetration of molecules, and, therefore, to optimize the delivery of the drug to the target neurons high concentrations of have to be employed. In order to see if this drug is toxic at high concentrations we performed an experiment where the worms were exposed to 50, 100, and 200mg/ml of Citicoline. Results for the higher employed concentration, 200mg/ml, are shown in Figure 3.4. We found that the lifespan of the worms exposed to Citicoline as compared to the control population have almost the same lifespan, 12.1 and 13.0 days, respectively, and therefore the drug present no toxicity at the concentrations employed. We therefore chose to use 200mg/ml as the concentration of Citicoline for our experiments as it do not harm the worms and it would maximize the drug intake.

3.2.5 Results 2: Laser microsurgery and imaging: axon cutting and regeneration

3.2.5.1 The multimodal microscope

For this project we use the same multimodal microscopy setup employed for the chapter related to damage assessment of axotomy . Basically, it is a multiphoton microscope that was built around a commercial confocal inverted microscope using Ti:Sapphire femtosecond laser. Both laser sources were coupled through 2 different input ports in such a way that both the confocal and multiphoton sections could work independently and simultaneously. This multimodal setup can be used in the linear and nonlinear regime with a variety of different techniques working in a simultaneous way. In particular, the nonlinear input could be used for performing the axotomy while the confocal unit could be used to visualize axotomy and the collateral damage at the same time. Besides, white light illumination can be employed to follow the worm inside the microfluidic chip by using a camera attached to a side port.

3.2.5.2 Worms sample preparation

C. elegans were grown on nematode growth medium (NGM) agar plates using standard procedures [27]. To visualize the axons used for these studies, we employed the transgenic strain juIs76 [unc-25::gfp] II that express GFP in D-type motoneurons. When required, and just before the experiments, preparations of worms in liquid media (M9 saline buffer) were prepared by picking the worms from the NGM plates to a drop of M9 buffer for cleaning. Then, 10 to 20 worms were transferred from the drop to a 100ml Eppendorf tubes full of M9 buffer. The solutions of worms were kept a 20ºC until their use.

3.2.5.3 Worms recovery after axotomy

For control worms recovery was made in regular 5 cm diameter NGM bacteria-seeded agar plates. For the drug testing experiments, Citicoline were dissolved in M9 saline buffer to a concentration of 200mg/ml and vortexed for 1min at maximum speed. Worms to be recovered are put on regular 5 cm diameter NGM plates. Just after this, 100µl of the Citicoline solution are spread uniformly over the bacterial lawn. This preparation results in a drug load per area of 1.6mg/cm^2. All plates were kept a 20ºC until their use.

3.2.5.4 Lifespan experiments

To monitoring survival in *C. elegans* we prepared populations of synchronous worms as described in the literature [28]. Test and control populations were transferred to the bacteria seeded NGM plates. Lifespans of the worms were monitored by observing each day whether or not the animals moved in response to being touched with a platinum wire. Worms that did not move were scored as dead. Worms were removed from the analysis of lifespans if they were lost during incubation. During the first week following removal of the worms from the device, we transferred the worms to fresh plates every day in order to separate the worms from their progeny.

3.2.5.5 Axotomy

Axotomies were performed on the commissures of the D-type motoneurons, close to the ventral cord (~5-10μm away). The position of the focal plane for cutting was found based on simultaneous TPEF imaging of the axon. Axotomies were performed by parking the tightly focused laser beam on the target point while controlling the irradiation time with an electronic shutter. For this work, the laser central wavelength was set to 868nm. We employed a water immersion 25x 1.05NA microscope objective that focuses the beam to a point spread function (PSF) of full-width-at-half-maximum (FWHM) dimensions of 0.7 μm transversal and 1.5 μm axial. The laser power for cutting was adjusted to fit the optimal encountered with the multimodal approach described in the last chapter ($3x10^{12}W/cm^{2)}$. This resulted in an optimal average power of 130mW (energy per pulse of 1.75nJ). The exposure time for axotomy was set to 200 ms.

3.2.5.6 Axon regeneration

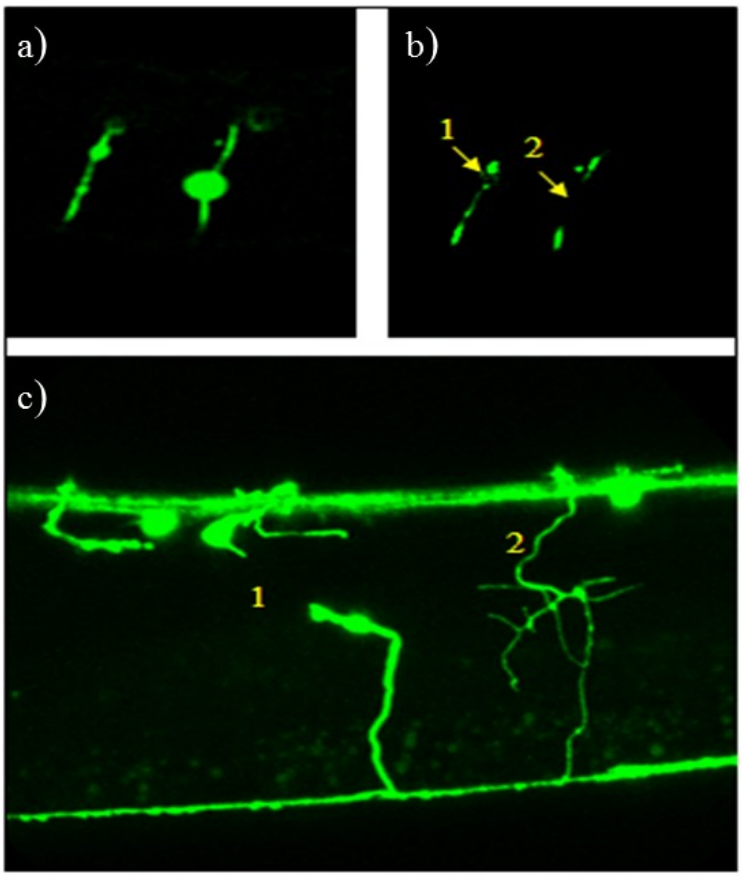

Figure 3.5: Patterns of axon regeneration – full reconnection.
A couple of adjacent D-type neuronal axons a) before and b) after laser cutting. Arrows point to the place of axotomy for axons 1 and 2. Both neurons regenerated axons, but only axon 2 succedded to fully reconnect to the dorsal cord.

As explained before we chose the D-type motor neurons in young adult worms as targets for axotomy. D-type motoneurons receive and provide input on both the ventral and dorsal side of the body. Their cell bodies are located in the ventral cord, and they extend circumferential axons towards the dorsal side where they form synapses to body muscles. This fact makes these axons ideal for our experiments as they are well isolated and can be identified and recorded using any type of fluorescence microscopy.

The experiments reported in this section were carried out as follows. A solution containing synchronized worms was prepared in a 100ml tube. Then, worms were loaded one-by-one into the microfluidic device for immobilization. Laser axotomy was performed once the worm was loaded and stabilized into the channel and no

major movements were detected. Among 3 to 5 axons were then cut per worm. For this, TPEF microscopy was used to find the commissure of interest and select the targeted point on the axon. By doing so, a cut efficiency of 100% was obtained. Worms were then taken off from the microfluidic device and recovered in NGM plates. The whole procedure of immobilization, imaging and unloading lasted not longer than 2 minutes per worm (axotomy itself lasted less than 10s per point). Control and test worm populations were put on regular NGM plates. Test population was treated *in situ* with a solution of 200mg/ml of Citicoline that was spread on the bacterial lawn. After 24h of recovery both sets of worms were loaded again to the microfluidic device to check for the regeneration using confocal fluorescence microscopy.

Different patterns of regeneration were observed and scored in both populations. Regenerating axons either emerge from the cell body or as a continuation of the proximal end of the severed axon. Figure 3.5(a) show two adjacent axons before the surgery and Figure 3.5(b) show the axons after the surgery, where arrows indicate the place where the axotomy was performed. Axon 1 in in Figure 3.5(b) regenerated *de novo* from the adjacent cell body, as can be seen in Figure 3.5(c).

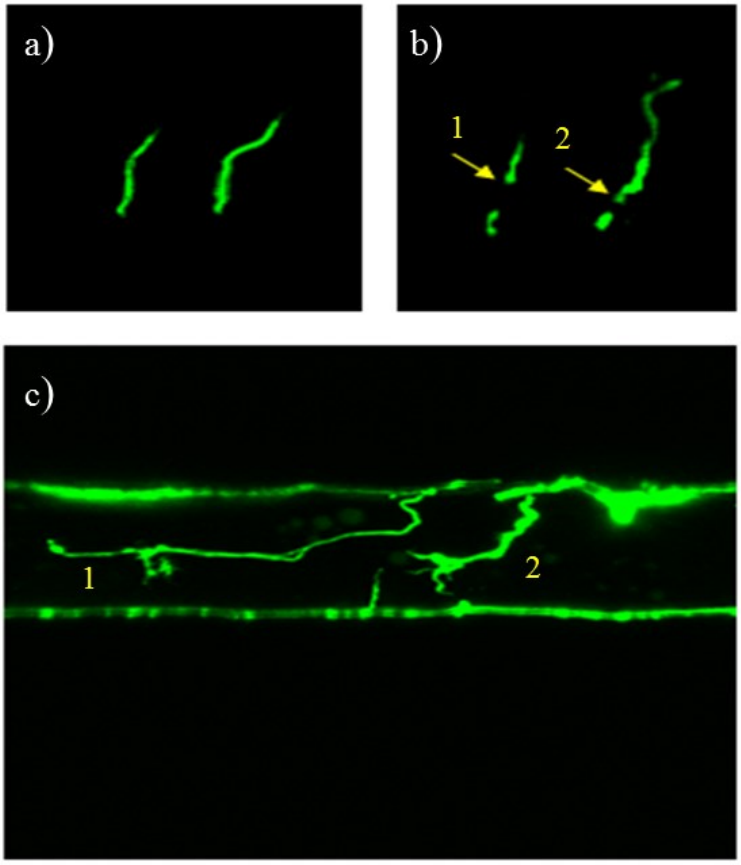

Figure 3.6: Patterns of axon regeneration – long branches
A couple of adjacent D-type neuronal axons a) before and b) after laser cutting. Arrows point to the place of axotomy. c) Both neurons regenerated axons, but none of them reconnect to the dorsal cord after 24h. Instead, they grew long axonal processes along worm's body.

Here some axonal branches can be seen sprouting close by the adjacent cell body. It is clear also from Figure 3.5(c) that axon 1 did not reconnect to the distal end or to the dorsal cord. In contrast, axon 2 appear fully reconnected to the dorsal cord by a thin branch that is connected to the ventral cord appears thinner as compared with normal distal ends (compare with the distal end of axon 1.). Similarly, another regeneration pattern was observed where no functional reconnection was achieved. An example of such pattern is shown in Figure 3.6. In this case two operated neurons seem to regenerate from their proximal ends and extend long axonal processes along the nematode body. None of them get to reconnect to the dorsal cord within the set evaluation interval of 24h. It is apparent, though, that axon 2 is very close to reach a functional reconnection with either its distal end or the dorsal. It is interesting to note

that axon 1 show two branches where one of them seem to be directed in the right direction toward the ventral cord.

Finally, in some cases we observed what is known as “aberrant connection” where the axon result in a reconnection after the axotomy but the point of connection is erroneous. Usually this happens when the axon reconnects back to the ventral cord or to a proximal end of other operated axon.

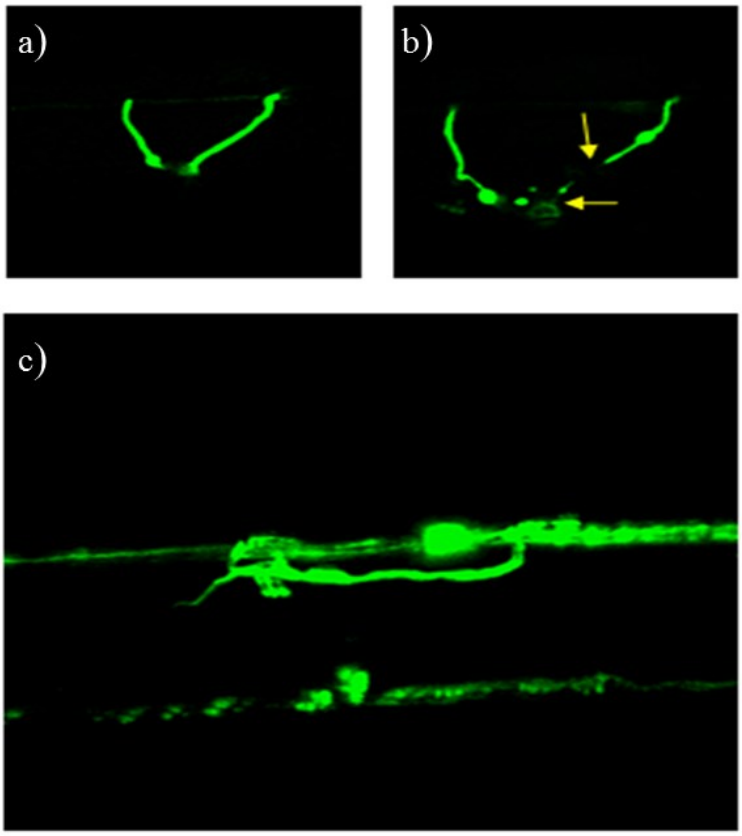

Figure 3.7: Patterns of axon regeneration – aberrant connections
D-type neuronal axon a) before and b) after laser cutting. Arrow point to the place of axotomy. c) Neuron regenerated an axon, but made an aberrant reconnection to the ventral cord.

Figure 3.7 illustrate one of such cases where an axonal branch is generated at one side of the cell body. The axon extended parallel to the ventral cord of the nematode and got finally connected to it at some point on the other side of the originating cell body.

The aforementioned regeneration patterns were observed in both control and Citicoline-treated worms. Basically most of the cut axons regenerate: 27 axons (90%, n=30) from the control and, 20 axons (95%, n=21) from the Citicoline treated

population. We have found also that, complete regeneration was achieved in 7 axons (26% of the regenerated) from control and, 7 axons (33% of the regenerated) from the Citicoline-treated population. Finally, the occurrences of aberrant connections were low in both populations examined. Just one axon per population showed such behavior, corresponding to 4% and 5% of the regenerated axons for control and test populations, respectively. As summary of these results is shown in Table 3.1

Table 3.1. Summary of the axon regeneration experiments.

Summary	Axotomies performed	Succesful cuts	Regeneration efficiency	Complete regeneration	Aberrated regeneration
Control	30	30 (100%)	27 (90%)	7 (26%)	1 (4%)
Citicoline	21	21 (100%)	20 (95%)	7 (33%)	1 (5%)

3.2.6 Discussion and concluding remarks

The first important task of this work was to design, build and characterize a microfluidic-based immobilization system. We have developed a protocol for handling the worms in order to deliver and recover the individuals form the implemented device for axon regeneration experiments. The reliability and viability of the microfluidic-device were demonstrated as it is able to maintain the worms still enough as to perform the surgery and to take pre- and post-operation confocal images, affecting minimally the lifespan of the worms (see Figure 3.3). The second relevant result of this work was the evaluation of the toxicity of Citicoline on *C elegans.* Several different concentrations of Citicoline were employed to evaluate a dose that resulted toxic to these animals. High doses up to 200mg/ml (approx. 400mM) do not produce any toxic effects as treated worms present normal lifespan

as compared with control population, Figure 3.4. In order to maximize the drug intake for the regeneration experiments, the maximum characterized concentration, 200mg/ml, was employed. Previous studies on the effects of small molecules on *C elegans* axon regeneration have used concentration of the order of 2-4 mM, where the worms were treated within a liquid solution [30]. In contrast, for this work, the drug solution was applied to the bacterial lawn of regular NGM plates that may require much bigger concentration of the test chemical to be effectively delivered to the worms [31,32]. The third relevant result of this work is that both the microfluidic device and the protocol enable to observe and characterize the different patterns of regeneration that, although reported previously in several communications [4,33], remained elusive in our experiments due to the low throughput and inefficacy of the normal sample preparation. In addition, 100% cut efficacy was achieved thanks to the previous optimization based on multimodal imaging. Several regeneration patterns were observed without qualitative distinction between control and Citicoline-treated populations. After axotomy, neurons respond either: regenerating new axons from either the cell body or the proximal stump, Figure 3.5; growing long axonal branches, Figure 3.6; and making aberrant connections, Figure 3.7. The regeneration efficiency was very high for both control and treated populations, reaching 90% and 95% of the total number of worms, respectively. From these, full reconnection was observed only in the 26% of the control and in the 33% of the treated worms. The rest of the regenerated axons did not reach the dorsal cord within 24h post-axotomy, and a minority made aberrant connections. A qualitative analysis of the results points to a better performance of the axon regeneration in the population treated with Citicoline. Nevertheless, the results are not conclusive due to the impossibility to perform a statistical test on the presented data to evaluate level of significance of the regeneration enhancement produced by Citicoline. In spite of this, the proposed methodology opens up a wide range of possible experiments that would help to reliable assess the performance of Citicoline in *in vivo* invertebrate animal models. Measurement of the many different parameters like area of the growth cone, length of the axonal branches and time lapse experiments at different time resolutions would help to better evaluate the effect of the drug to axon regeneration. Additional elements and compartments would be added to the design of the

microfluidic chip in order to allow the recovery *in situ.* This would increase the reliability of the procedure for dynamic studies of axon regeneration as the many cycles of load-in take-out required for imaging can be avoided. Finally, different ways to supplement the drug would help to better understand the molecular mechanism leading to an enhanced regeneration. Treating the worms with the drug before, after and before-after the operation can result in a way to discern if the drug works better as a neuro-protective or as a neuro-repairing agent.

3.3 References

1. S. I. C. O. Santos, M. Mathew, O. E. Olarte, S. Psilodimitrakopoulos, y P. Loza-Alvarez, "Femtosecond Laser Axotomy in Caenorhabditis elegans and Collateral Damage Assessment Using a Combination of Linear and Nonlinear Imaging Techniques," PLoS ONE **8**, e58600 (2013).

2. M. Yanik, H. Cinar, H. Cinar, A. Chisholm, Y. Jin, y A. Ben-Yakar, "Neurosurgery - Functional regeneration after laser axotomy," Nature **432**, 822-822 (2004).

3. Z. Wu, A. Ghosh-Roy, M. Yanik, A. Zhang, Y. Jin, y A. Chisholm, "Caenorhabditis elegans neuronal regeneration is influenced by life stage, ephrin signaling, and synaptic branching," PNAS **104**, 15132-15137 (2007).

4. C. V. Gabel, F. Antoine, C.-F. Chuang, A. D. T. Samuel, y C. Chang, "Distinct cellular and molecular mechanisms mediate initial axon development and adult-stage axon regeneration in C. elegans," Development **135**, 1129-1136 (2008).

5. R. El Bejjani y M. Hammarlund, "Neural Regeneration in Caenorhabditis elegans," Annu. Rev. Genet. **46**, 499-513 (2012).

6. J. J. Secades y J. L. Lorenzo, "Citicoline: pharmacological and clinical review, 2006 update," Methods Find. Exp. Clin. Pharmacol. **28 Suppl B**, 1-56 (2006).

7. R. M. Adibhatla y J. F. Hatcher, "Citicoline mechanisms and clinical efficacy in cerebral ischemia," J. Neurosci. Res. **70**, 133-139 (2002).

8. X. A. Alvarez, C. Sampedro, R. Lozano, y R. Cacabelos, "Citicoline protects hippocampal neurons against apoptosis induced by brain beta-amyloid deposits plus cerebral hypoperfusion in rats," Methods Find. Exp. Clin. Pharmacol. **21**, 535-540 (1999).

9. L. A. Teather y R. J. Wurtman, "Dietary CDP-choline supplementation prevents memory impairment caused by impoverished environmental conditions in rats," Learn. Mem. Cold Spring Harb. N **12**, 39-43 (2005).

10. E. McGlade, "Improved Attentional Performance Following Citicoline Administration in Healthy Adult Women," Food Nutr. Sci. **03**, 769-773 (2012).

11. A. Dávalos, J. Alvarez-Sabín, J. Castillo, E. Díez-Tejedor, J. Ferro, E. Martínez-Vila, J. Serena, T. Segura, V. T. Cruz, J. Masjuan, E. Cobo, J. J. Secades, y International Citicoline Trial on acUte Stroke (ICTUS) trial investigators, "Citicoline in the treatment of acute ischaemic stroke: an international, randomised, multicentre, placebo-controlled study (ICTUS trial)," Lancet **380**, 349-357 (2012).

12. T. C. elegans S. Consortium, "Genome Sequence of the Nematode C. elegans: A Platform for Investigating Biology," Science **282**, 2012-2018 (1998).

13. L. Ségalat, "Invertebrate Animal Models of Diseases as Screening Tools in Drug Discovery," ACS Chem. Biol. **2**, 231-236 (2007).

14. S. Shaham, "Methods in cell biology," WormBook (2006).

15. A. B. Byrne, T. J. Edwards, y M. Hammarlund, "In vivo laser axotomy in C. elegans," J. Vis. Exp. JoVE (2011).

16. P. A. Padilla y M. L. Ladage, "Suspended animation, diapause and quiescence: Arresting the cell cycle in C. elegans," Cell Cycle **11**, 1672-1679 (2012).

17. M. R. Massie, E. M. Lapoczka, K. D. Boggs, K. E. Stine, y G. E. White, "Exposure to the metabolic inhibitor sodium azide induces stress protein expression and thermotolerance in the nematode Caenorhabditis elegans," Cell Stress Chaperones **8**, 1-7 (2003).

18. C. B. Rohde y M. F. Yanik, "Subcellular in vivo time-lapse imaging and optical manipulation of Caenorhabditis elegans in standard multiwell plates," Nat. Commun. **2**, 271 (2011).

19. H.-S. Chuang, H.-Y. Chen, C.-S. Chen, y W.-T. Chiu, "Immobilization of the nematode Caenorhabditis elegans with addressable light-induced heat knockdown (ALINK)," Lab. Chip **13**, 2980-2989 (2013).

20. E. Kim, L. Sun, C. V. Gabel, y C. Fang-Yen, "Long-Term Imaging of Caenorhabditis elegans Using Nanoparticle-Mediated Immobilization," PLoS ONE **8**, e53419 (2013).

21. F. Zeng, C. B. Rohde, y M. F. Yanik, "Sub-cellular precision on-chip small-animal immobilization, multi-photon imaging and femtosecond-laser manipulation," Lab. Chip **8**, 653 (2008).

22. C. B. Rohde, F. Zeng, R. Gonzalez-Rubio, M. Angel, y M. F. Yanik, "Microfluidic system for on-chip high-throughput whole-animal sorting and screening at subcellular resolution," Proc. Natl. Acad. Sci. **104**, 13891 -13895 (2007).

23. S. Mondal, S. Ahlawat, y S. P. Koushika, "Simple microfluidic devices for in vivo imaging of C. elegans, Drosophila and zebrafish," J. Vis. Exp. JoVE (2012).

24. S. E. Hulme, S. S. Shevkoplyas, J. Apfeld, W. Fontana, y G. M. Whitesides, "A microfabricated array of clamps for immobilizing and imaging C. elegans," Lab. Chip **7**, 1515-1523 (2007).

25. N. Pujol, S. Cypowyj, K. Ziegler, A. Millet, A. Astrain, A. Goncharov, Y. Jin, A. D. Chisholm, y J. J. Ewbank, "Distinct Innate Immune Responses to Infection and Wounding in the C. elegans Epidermis," Curr. Biol. **18**, 481-489 (2008).

26. R. Conant y A. G. Schauss, "Therapeutic applications of citicoline for stroke and cognitive dysfunction in the elderly: a review of the literature," Altern. Med. Rev. J. Clin. Ther. **9**, 17-31 (2004).

27. S. Brenner, "The Genetics of Caenorhabditis Elegans," Genetics **77**, 71-94 (1974).

28. M. Porta-de-la-Riva, L. Fontrodona, A. Villanueva, y J. Cerón, "Basic Caenorhabditis elegans methods: synchronization and observation," J. Vis. Exp. JoVE e4019 (2012).

29. S. Grill y E. H. K. Stelzer, "Method to calculate lateral and axial gain factors of optical setups with a large solid angle," J. Opt. Soc. Am. A **16**, 2658-2665 (1999).

30. C. Samara, C. B. Rohde, C. L. Gilleland, S. Norton, S. J. Haggarty, y M. F. Yanik, "Large-scale in vivo femtosecond laser neurosurgery screen reveals small-molecule enhancer of regeneration," Proc. Natl. Acad. Sci. U. S. A. **107**, 18342-18347 (2010).

31. D. Kokel, Y. Li, J. Qin, y D. Xue, "The nongenotoxic carcinogens naphthalene and para-dichlorobenzene suppress apoptosis in Caenorhabditis elegans," Nat. Chem. Biol. **2**, 338-345 (2006).

32. P. M. Dexter, K. A. Caldwell, y G. A. Caldwell, "A predictable worm: application of Caenorhabditis elegans for mechanistic investigation of movement disorders," Neurother. J. Am. Soc. Exp. Neurother. **9**, 393-404 (2012).

33. M. F. Yanik, H. Cinar, H. N. Cinar, A. Gibby, A. D. Chisholm, Y. Jin, y A. Ben-Yakar, "Nerve Regeneration in Caenorhabditis elegans After Femtosecond Laser Axotomy," Sel. Top. Quantum Electron. IEEE J. Of **12**, 1283-1291 (2006).

Chapter 4: Laser photodisruption and of two-photon excitation fluorescence microscopy in human crystalline lenses

4.1 Abstract

A Ti:Sapphire femtosecond (fs) laser source was used to produce photodisruption on a number of excised human crystalline lens samples. A high numerical aperture (NA=1.05) microscope objective having a large working distance (2.0mm) was used to focus the light onto excised crystalline lens samples. Under these circumstances, the modification generated on the crystalline lens was highly localized and almost transparent. However, the damaged region showed autofluorescence that could be visualized by means of two-photon excitation microscopy using the same laser source

4.2 Introduction

Presbyopia is an age related condition in which the lens of the eye loses the capability of accommodation, which is achieved by the action of the cilliary muscle on the zonular fibers attached to the crystalline lens. It is usually accepted that when the cilliary muscle relaxes its diameter increases, pulling from the zonular fibers and reducing the power of the crystalline lens by making it flatter. On the contrary, when contracting, the inner diameter of the cilliary muscle becomes smaller, releasing tension from the zonular fibers allowing the lens to change to a thicker, rounder shape [1].

It is also most widely accepted that presbyopia appears due to a process of sclerosis of the crystalline lens. This process is continuous and steady through life, and can be detected in the early years of childhood. In adulthood, sclerosis translates into loss of flexibility of the crystalline lens and, as a consequence, the subject cannot focus on near distance objects. By age 60, virtually 100% of the population is affected by presbyopia [2].

Many different options for treatments of presbyopia have been suggested to date. The most common approach consists on the use of optical elements that allow the subject to focus on multiple distances, such as bifocal, multifocal and progressive addition lenses and multifocal contact lenses. A wide range of surgical solutions have been

suggested to minimize the effects of presbyopia [3], such as crystalline lens replacement by multifocal intraocular lenses, intracorneal inlays and anterior ciliary sclerotomy [4–7]. Also, great advance has been reported on laser surgery for multifocal correction of the cornea [8–10]. Another approach to minimize the impact of presbyopia on the subject's day to day life is monovision. Under this approach one eye is corrected to focus on short distances and the other on the farther ones. This correction can be achieved either using contact lenses or laser surgery. Monovision relays on the brain capabilities to ignore the image of the eye that is blurred in favor of that on focus according to the needs of the patient. In this option there is a clear impact on depth perception since binocularity is lost [11,12].

All the treatments described above focus on minimizing the effects of presbyopia on the patient, but do not provide a cure for it. None of them can restore the flexibility of the crystalline lens that is lost over time.

A novel approach that aims at restoring flexibility lost with age in the crystalline lens has been reported. This treatment is referred to as laser lentotomy, since a laser beam is used to modify the internal structure of the crystalline lens producing controlled and localized photodisruption on the tissue. This allows more relative motion of the internal structure of the lens increasing its flexibility [13]. Studies have been published on the safety of the technique on animal models showing no evidence of cataract, changes in overall transmittance of the lens or other safety issues related to the treatment [14]. The studies also characterized the damage generated in the tissue describing a structure of intraocular bubbles on the areas where the laser beam was focused. These bubbles coalesced unless the damage of the laser was spaced enough and a certain pulse energy threshold was not reached. These effects of the treatment may compromise the optical quality of the lens affecting the image of an object on the retina. Further studies have extended this work to excised human crystalline samples, reporting changes on their flexibility [15,16]. Finally, *in vivo* experiments have been performed on animal models [17].

Fs laser oscillators are widely in photodisruption since they can help minimize thermal damage. Under high NA focusing conditions, their high pulse intensity allows for high localization of damaged volumes, while keeping the mean power

low [18,19]. In addition, their short pulse duration (low energy) avoid thermal build up reducing the effects on the tissue due to photodisruption [20]. The use of these laser sources improves efficiency, accuracy and safety of the procedure.

Photodisruption has been used before to modify different types of biological tissue, e.g. skin, sclera, cornea and retina, to name a few, and the use of a range of different infrared (IR) pulsed laser sources in the field of ophthalmology is very wide. They are used in photocoagulation for the treatment of diabetic retinopathy [21–24], corneal flap generation for refractive laser surgery [25–27], intrastromal laser surgery [10], and capsulotomy [28,29]. Also, other research applications are being developed, such as chicken cornea ablation [30], and modification of excised cat cornea and lens [31–33].

It has been observed that subproducts that are generated as a result of photodisruption in different kinds of biological tissue can modify two photon excitation fluorescence (TPEF) signal [34]. An increase on the auto fluorescence signal has been observed in different kinds of biological tissue that have been treated using photo ablation [35–38].

In the work presented here, we extend the application of photodisruption using fs lasers to studies on human crystalline lens samples, by adapting the parameters of the delivered fs pulses in order to minimize the volume of damaged tissue. The main objective behind this approach is to optimize photoablation parameters, minimizing any effects that cavitation bubbles could have on the visual performance of the patient. Advances in this direction could have a great impact in a future implementation of lentotomy for the treatment of presbyopia. Since small effects of photoablation can be difficult to observe on the human crystalline lens, this work also shows the capability to use two-photon excitation fluorescence (TPEF) microscopy to visualize with improved contrast the effect of photodisruption on the samples [39].

4.3 Methods

A Kerr lens modelocked Ti:Sapphire femtosecond laser source (Coherent Inc., USA) was used in these experiments. The source generated a beam with a repetition rate of 76 MHz, 800nm wavelength, and pulse width below 150fs.

The fs laser beam was coupled into a modified Eclipse Ti-E microscope (Nikon Corp., Japan), equipped with a water immersion, high numerical aperture (NA=1.05) and long working distance (2.0mm) microscope objective (Olympus Corp., Japan), which is optimized for infrared light. Coupling of the beam to the microscope was performed through a set of two scanning mirrors, that allowed to sweep the focused beam on the sample to generate the images [40]. This workstation is capable of different simultaneous high-resolution linear (confocal, DIC, laser scanned transmitted light and wide-field, fluorescence, etc) and non-linear (TPEF, second and third harmonic generation), imaging techniques, but it is also capable to modify the sample by means of photoablation or photodisruption, depending on the exposure parameters and the sample itself.

In order to generate photodisruption, the average power delivered to the sample was 240-280mW, which corresponds to a pulse energy of ~3.5nJ. For imaging purposes, a motorized neutral density filter was placed in the path of the beam so that the average power was reduced to ~24mW on the sample plane. This configuration allowed changing from imaging to ablating configuration with ease, by just removing the motorized ND filter. Thus, the procedure for data acquisition consisted on imaging the sample to determine the region to be treated, changing to ablating configuration by removing the motorized ND filter, performing photodisruption after choosing the desired geometry, and finally going back to imaging configuration to obtain images of the treated area for characterization purposes by repositioning the motorized ND filter on the beam path. This whole procedure was performed in less than a second.

In order to control the geometry of the photodisruption pattern on the sample, two different scanning configurations were available. On the first one, the two galvanometric mirrors used to scan the beam and generate the images, were controlled to sweep the fs laser beam over the sample following a chosen geometry, usually a straight line. The speed at which the laser beam was scanned over the sample could be changed very precisely so that the amount of energy transferred to the tissue could be controlled. Sweeping the beam slowly allowed for more laser pulses to hit a particular point in the sample, building up the energy delivered on that point. On the other hand, sweeping the beam at faster speed reduced the number of

pulses and energy delivered. This method limited the size of the ablation pattern to the field of view of the system. An additional scanning system used a translation stage to move the sample around, which allowed for generation of much larger photodisruption patterns, comparable to the size of the whole crystalline lens itself [41].

Sample preparation and manipulation was performed in two different ways. In a first approach, the crystalline lens was completely removed from the ocular globe, and placed on a glass bottom petri dish suitable for microscopy. The petri dish was filled with balanced salt solution (BSS) to keep the sample hydrated. There was no fixation of the lens other than the pressure of the weight of the lens itself on the petri dish. This first approach was mainly intended to minimize complications related to the manipulation of the whole ocular globe, and to determine the most appropriate parameters for both, image acquisition and photodisruption.

On a second stage, and once these parameters had been determined, the crystalline samples were treated when still inside the ocular globe. To ensure that the working distance of the microscope objective was enough to treat the sample, the cornea was removed before the experiment, along with the rest of the anterior chamber, including the iris, leaving the crystalline lens exposed. The remaining ocular globe was then placed on the petri dish and secured using a plastic ring that minimized motion. BSS was also poured on the petri dish to keep the exposed area of the lens hydrated.

We studied lens samples from 6 donors with a mean age of 81 years (range 71 - 88).The samples were treated within 3 to 5 days post mortem.

4.3.1 Ethical issues

As already stated, excised human crystalline lens samples were used on this study. Samples were provided by the Eye Bank for the Treatment of Blindness of the Centro de Oftalmología Barraquer, in Barcelona. Samples were obtained fulfilling the European Commission Directive 2006/17/CE concerning donation, procurement and control of the tissues and cells of human origin, as well as good clinical practices. Also, European legislation on Informed Consent 2001/20/CE was considered when obtaining these samples.

4.4 Results

Bright field, transmitted light and TPEF microscopy images of several human crystalline lens samples were generated using the system described in the previous section. Images of tissue at depths of up to 1.5mm where generated before and after photodisruption.

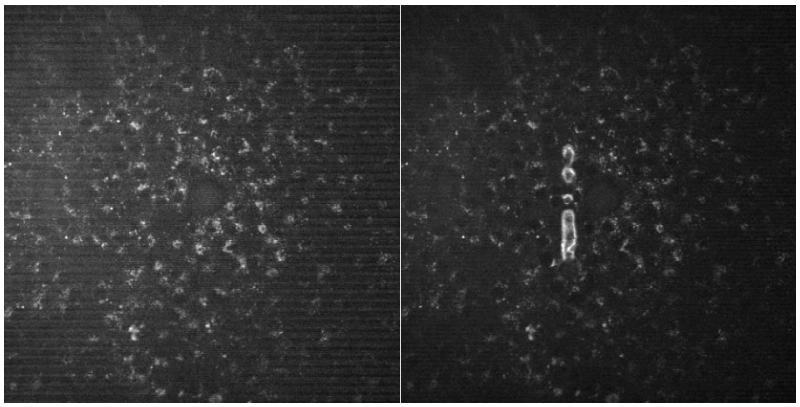

Figure 4.1:TPEF images of the epithelium of a human crystalline lens sample.
TPEF of samples obtained before (left) and after (right) performing laser ablation. Images are 125x125 μm

Figure 4.1 shows two TPEF images of the same area of the epithelium of a human crystalline lens sample before and right after photodisruption was performed on them. Before photodisruption, the image shows autofluorescence signal detected from the tissue itself, allowing for the identification of epithelial cells. After photodisruption, strong autofluorescence signal is detected on the surroundings of the volume exposed to the high power fs laser beam. From the images, a two fold increase in the signal to noise ratio (SNR) of autofluorescence from damaged tissue was calculated compared to that from epithelial cells. These images show that TPEF microscopy is a suitable technique to determine with high contrast the volumes of the tissue that had been affected by photodisruption.

These changes in autofluorescence generated by photodisruption and detected by means of TPEF microscopy were studied at different depths and on different samples in order to characterize them. Also other imaging techniques (namely bright field and transmitted light) were used to generate images of the same areas of the tissue, for comparison purposes.

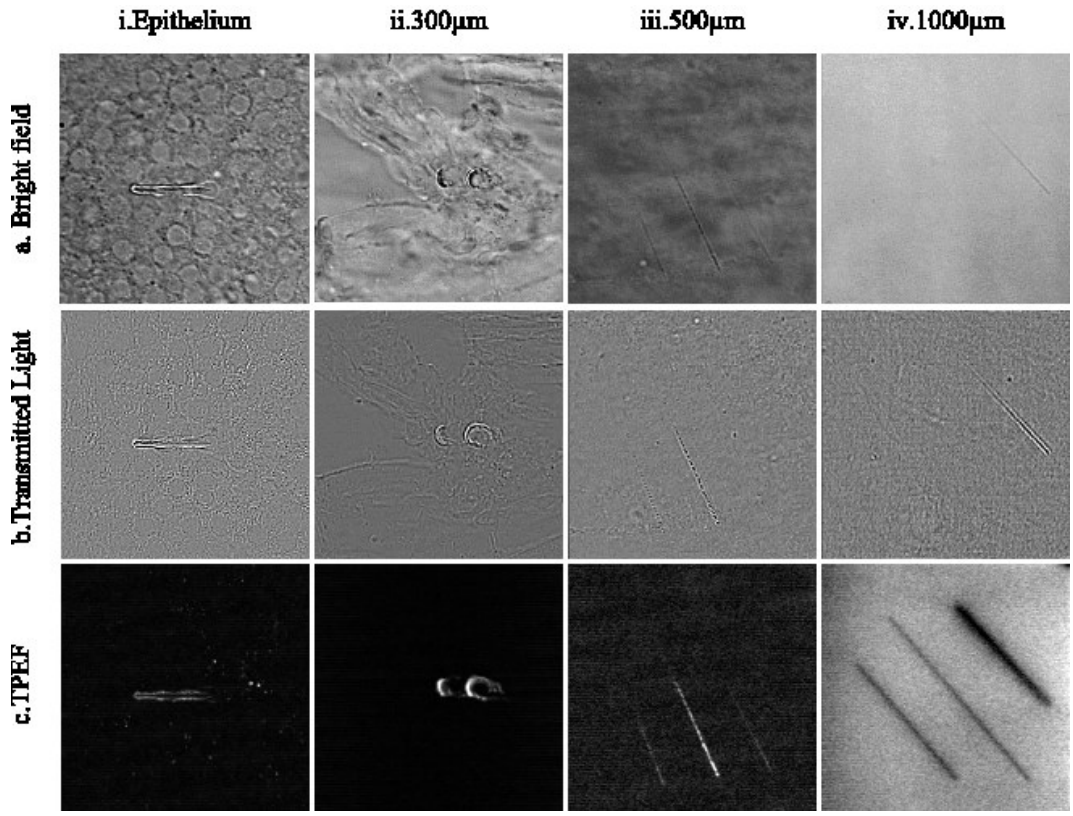

Figure 4.2: Images of the same crystalline lens sample obtained by means of different imaging techniques at different depths
Each column shows images from different depths: (i) surface of the crystalline lens (epithelium), (ii) 300µm, (iii) 500µm deep, and (iv) 1000µm deep. Each row shows images obtained by means of the same technique: (a) bright field images, (b) transmitted light, and (c) TPEF. All images are 125×125µm in size.

Figure 4.2 shows some images obtained from a particular sample of human crystalline lens tissue by means of different techniques and at different depths. On the surface of the crystalline lens, epithelial cells are clearly visible on bright field and transmitted light images. Autofluorescence signal is also generated in epithelial cells, as it can be observed on the TPEF image, however tissue affected by photodisruption shows a two fold increase of autofluorescence signal compared to autofluorescence from epithelial cells.

In images of planes at 300 µm deep, the structure of the lens fiber cells is visible in the bright field and transmitted light images, and may not be straight forward to discriminate from the damage generated by photodisruption. In TPEF images at this depth, untreated fiber cells did not generate any autofluorescence, and therefore the background of the image appears dark. However, damaged tissue did generate autofluorescence, and can be easily identified.

Tissue affected by photodisruption is difficult to identify on bright field and transmitted light images at 500µm, since it is very much localized. In the case of TPEF images for 500µm depth, tissue surrounding photodisruption volume appears bright over a dark background, making it easy to identify.

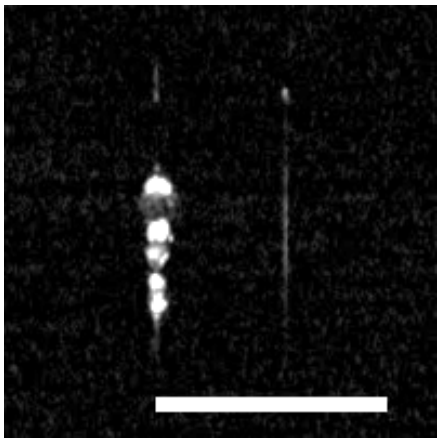

Figure 4.3: TPEF image of photodisruption treatment performed on a human lens tissue sample at 300µm depth.
Photodisruption geometry consisted on two vertical lines using different light beam energies. Left vertical line was performed at 0.0008J/µm, and shows small cavitation due to heat transfer. The width of the cavitation is ~7µm. Right line was performed at 0.0004J/µm, and shows no cavitation. The width of the lesion in this case is under 1µm. Scale bar is 50µm.

For depths at around 1mm, the structure of the lens fiber cells is less apparent on bright field and transmitted light images, probably due to scattering and absorption of light in the tissue. For TPEF images (row c) at 1mm depth (iv) it is interesting to see that the tissue that has been exposed to the fs laser beam appears darker than the surrounding volume, as opposed to brighter signal from damaged tissue over a darker background that can be observed on TPEF images from shallower planes. This effect has been consistently observed on the different samples studied. However, the combination of this increase on the background signal and a decrease in the signal from treated volumes for the TPEF images, translates once again on an increase on the contrast between treated and untreated tissue. Therefore, TPEF images prove appropriate to identify the volumes of the sample that have been treated by means of photodisruption. In order to reduce to a minimum the volume of tissue affected by photodisruption the speed at which the beam was swept over the sample was carefully chosen between values ranging from 0.0005µm/s to 0.05µm/s depending on the depth and the sample itself. Figure 4.3 shows the effect of changing the speed at

which the laser beam is swept over the sample. Slow scanning generated cavitation bubbles, extending photodisruption damage to larger volumes. At higher sweep speeds, fewer pulses were delivered at each point, and the damage was localized on a smaller volume. TPEF images like the ones shown in Figure 4.3 were used to determine for each sample and depth the threshold value of light energy for which photodisruption effects were observed on the sample, but no cavitation bubbles were generated. This threshold value will be referred to from now on as the *heat transfer threshold*.

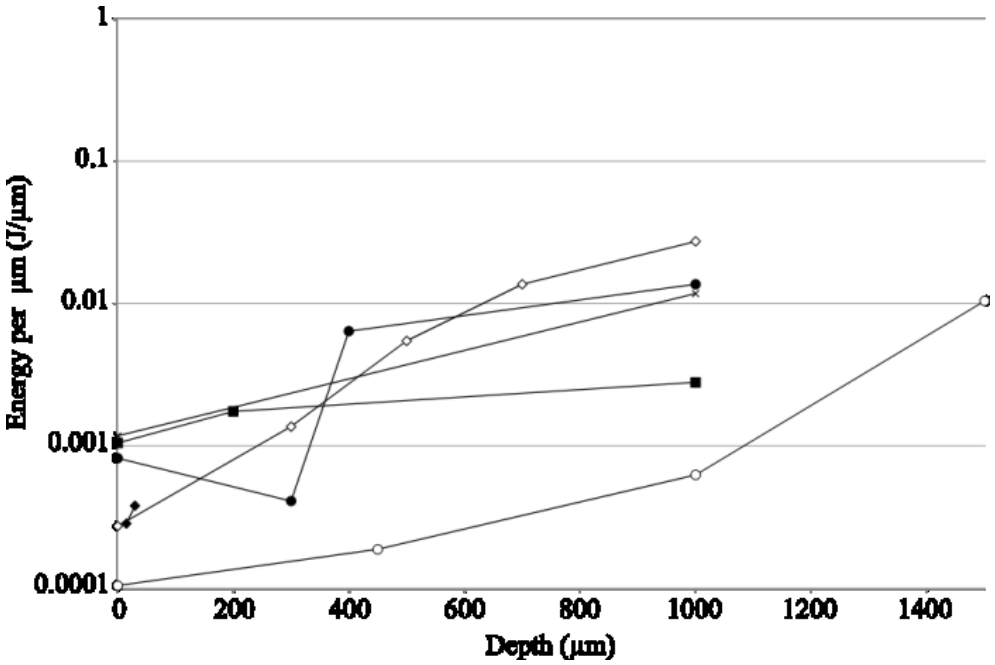

Figure 4.4: Value of the heat transfer threshold at different depths for six different samples.
The value on the y axis corresponds to the minimum energy value applied to the sample during photodisruption at a particular depth for which bubbles were observed. Data corresponding to the same sample are connected by a solid line

Figure 4.4 shows the values of the observed heat transfer threshold for several samples and depths. Great variability has been observed amongst the values of heat transfer threshold for different samples. This may be related to variability in lens transparency, cortical cataract and protein presence amongst the different samples studied, however, no correlation of the heat transfer threshold values with age was observed.

Despite this variability amongst samples, Figure 4.4 shows a tendency to higher values of the heat transfer threshold for deeper layers. In the surface, values as low as

0.0001 J/μm were enough to generate cavitation bubbles in the sample, while at 1.0-1.5mm deep energy had to be increased up to 0.03J/μm. Lens transparency is related to scattering and absorption. These effects may be responsible for lower efficiency in focusing light into a tight volume, and consequently for increasing heat transfer thresholds at deeper layers. Other effects, such as optical aberrations introduced by the lens sample itself, may also affect the performance of the microscope increasing the value of the heat transfer threshold for deeper layers.

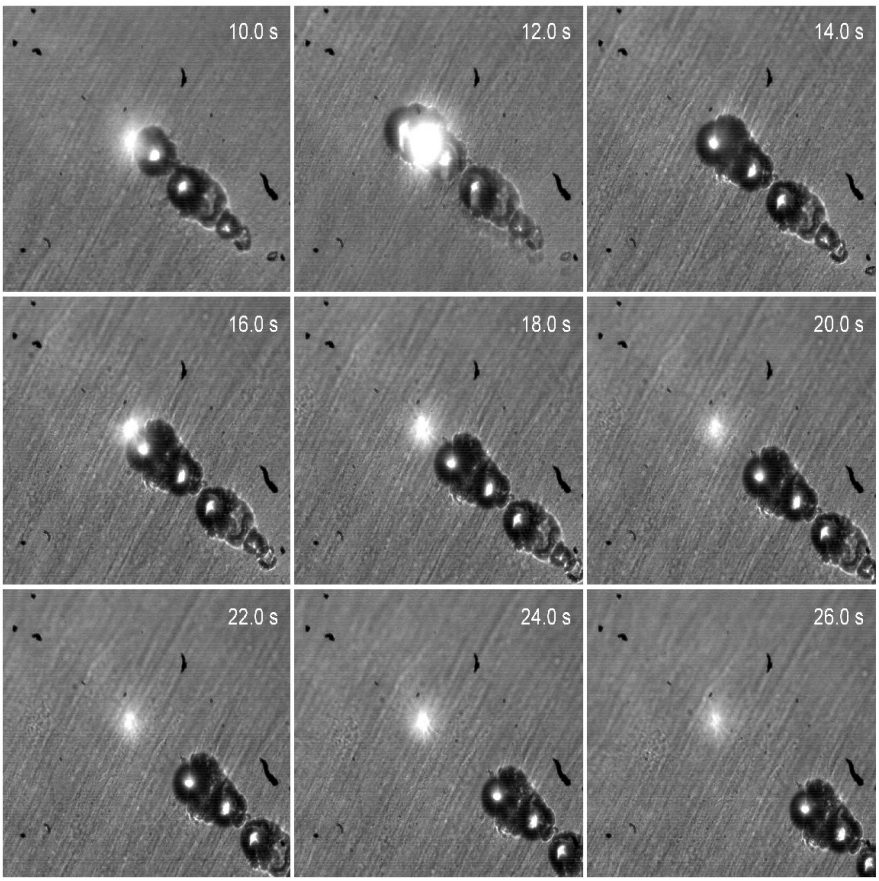

Figure 4.5: Frames of a video that shows the process of photodisruption performed on a human crystalline lens sample at a depth of 300μm.
Photodisruption was performed by focusing a fs laser beam onto the sample, while it was moved to different points by means of the translation stage of the microscope. At a certain point, no more damage is performed on the sample, and instead some sort of scintillation patterns can be observed. Frame size is 233x186μm.

Figure 4.5 shows a video depicting the process of photodisruption performed on a human crystalline lens sample at a depth of 300μm in real time. Photodisruption was performed by focusing a fs laser beam onto the sample, while it was moved by means of the translation stage on which the sample was placed, as detailed before.

The stage moved to different points, and stayed on each of them for 2sec. This time is long enough to ensure photodisruption on the tissue at that depth, and in fact formation of cavitation bubbles is observed in between the visible tissue structure, which is compatible with lens fiber cells. In second 13 of the video, the laser is focused over a volume of the sample where no photodisruption is generated, and instead some sort of scintillation patterns can be observed, that may indicate that the volume is filled with liquid that changes its refractive index due to temperature. This behavior was observed in a number of samples, at depths from 0 to 300μm, and therefore was considered relevant for this work. These volumes did not show any regularity in terms of geometrical distribution in the sample, nor did they present an identifiable shape.

4.5 Discussion and conclusions

The results detailed in the previous section show that laser ablation parameters can be carefully adjusted in order to minimize the volume of the tissue affected by photodisruption on human crystalline lens samples, avoiding the generation of cavitation bubbles. Results also show that TPEF is a very appropriate technique to study the effect of photodisruption in these samples, since the volumes of the tissue that have been affected by photodisruption can be easily identified using this technique.

According to Vogel et al. [20], the pulse energy delivered in the sample plane for the setup described in this work is not enough to achieve optical breakdown. Although usually laser ablation is linked to plasma formation due to optical breakdown, other mechanisms have been reported to modify the structure of the tissue even when only low density plasmas are generated. These mechanisms are mainly chemical effects and temperature build-up related to low density plasmas. If this is the case, in the experiments described above, by changing the speed at which the laser beam is swept over the sample, the temperature build up would be controlled, subsequently avoiding the formation of cavitation bubbles in the tissue, and reducing the volume of tissue affected by photodisruption.

It has also been observed that at depths from 0 to 300μm, some volumes were identified were no autofluorescence linked to photodisruption was observed. These

volumes seemed to be filled with liquid and did not present any regularity that allowed predicting their position. These observations may be compatible with the presence of swollen tissue, which may have appeared due to the process of removal of the anterior part of the eye, and also to the time that passed from donor's death until the experiment was held.

If these liquid filled volumes are not considered, two different regimes have been observed, with very different results in terms of autofluorescence signal observed from tissue damaged by photodisruption. The first regime would be that for tissue at depths from 0 to 500 μm, where an increase in the autofluorescence signal has been observed on tissue damaged by photodisruption. It has been described in the literature that photodisruption on different types of biological tissue can lead to an increase in the TPEF signal due to generation of photoproducts, most likely tyrosine dimerization [30,34,36,42]. These reports are compatible with the results obtained for laser ablation on layers up to 500μm deep. A second regime has been identified at deeper planes depths from 1000 to 1500 μm, in which a background autofluorescence signal has been observed, and a decrease on this signal characterizes the volumes where photodisruption has been performed. It is known that lens aging is related to accumulation of protein aggregates that absorb and scatter light. This leads to the characteristic discoloration of aged crystalline lenses, cataract formation and also the appearance of a number of fluorescent chemical compounds, mainly due to the interaction of UV light with the lens [43,44]. Researchers have suggested the use of this fluorescence as an indicator for cataracts that may help on their early identification [45]. Since the human lens samples used in these experiments come from aged donors, the high background TPEF signal observed is compatible with the presence of these fluorescent materials. Furthermore, photolysis of these chemical products by means of a fs second laser source has been proposed as a method to rejuvenate crystalline lens tissue [43]. Direct photobleaching as well as multiphoton-ionization of these fluorescent species (e.g. free electrons released from tryptophan residues) have been described as the physical mechanisms leading to the chemical deconstruction of these products [46]. These reports would be compatible with the phenomenon observed in these human crystalline lens samples for higher depths.

In conclusion, the use of a fs laser source to efficiently generate precise photodisruption patterns at different depths of up to 1.5mm inside human crystalline lenses has been presented. It has also been shown how the parameters of the laser system can be adjusted to produce either clean micron-sized or broader (bubble mediated) cuts at each particular depth. Also, TPEF microscopy was presented as an appropriate tool for the observation of the resulting photodisruption pattern that allows for a direct high-contrast post-surgical assessment of the procedure, all this employing the same fs laser source. The work described in this paper could help develop laser lentotomy by performing photodisruption in a more localized and controlled manner, as well as using TPEF to assess this damage.

4.6 References

1. W. N. Charman, "The eye in focus: accommodation and presbyopia," Clinical and Experimental Optometry **91**, 207–225 (2008).

2. R. A. Weale, "Epidemiology of refractive errors and presbyopia," Survey of Ophthalmology **48**, 515–543 (2003).

3. A. Glasser, "Restoration of accommodation: surgical options for correction of presbyopia," Clinical and Experimental Optometry **91**, 279–295 (2008).

4. G. Baïkoff, G. Matach, A. Fontaine, C. Ferraz, and C. Spera, "Correction of presbyopia with refractive multifocal phakic intraocular lenses," J Cataract Refract Surg **30**, 1454–1460 (2004).

5. S. Kashani, A. A. Mearza, and C. Claoué, "Refractive lens exchange for presbyopia," Cont Lens Anterior Eye **31**, 117–121 (2008).

6. O. F. Yilmaz, S. Bayraktar, A. Agca, B. Yilmaz, M. B. McDonald, and C. van de Pol, "Intracorneal inlay for the surgical correction of presbyopia," J Cataract Refract Surg **34**, 1921–1927 (2008).

7. D. R. Hamilton, J. M. Davidorf, and R. K. Maloney, "Anterior ciliary sclerotomy for treatment of presbyopia: a prospective controlled study," Ophthalmology **109**, 1970–1976; discussion 1976–1977 (2002).

8. A. Telandro, "Pseudo-accommodative cornea: a new concept for correction of presbyopia," J Refract Surg **20**, S714–717 (2004).

9. J. L. Alió, J. J. Chaubard, A. Caliz, E. Sala, and S. Patel, "Correction of presbyopia by technovision central multifocal LASIK (presbyLASIK)," J Refract Surg **22**, 453–460 (2006).

10. L. A. Ruiz, L. M. Cepeda, and V. C. Fuentes, "Intrastromal Correction of Presbyopia Using a Femtosecond Laser System," Journal of Refractive Surgery **25**, 847–854 (2009).

11. S. Jain, R. Ou, and D. T. Azar, "Monovision outcomes in presbyopic individuals after refractive surgery," Ophthalmology **108**, 1430–1433 (2001).

12. C. Schor, L. Landsman, and P. Erickson, "Ocular dominance and the interocular suppression of blur in monovision," Am J Optom Physiol Opt **64**, 723–730 (1987).

13. R. I. Myers and R. R. Krueger, "Novel approaches to correction of presbyopia with laser modification of the crystalline lens," J Refract Surg **14**, 136–139 (1998).

14. R. Krueger, J. Kuszak, H. Lubatschowski, R. Myers, T. Ripken, and A. Heisterkamp, "First safety study of femtosecond laser photodisruption in animal lenses: Tissue morphology and cataractogenesis," Journal of Cataract & Refractive Surgery **31**, 2386–2394 (2005).

15. T. Ripken, U. Oberheide, M. Fromm, S. Schumacher, G. Gerten, and H. Lubatschowski, "fs-Laser induced elasticity changes to improve presbyopic lens accommodation," Graefes Arch. Clin. Exp. Ophthalmol **246**, 897–906 (2008).

16. S. Schumacher, U. Oberheide, M. Fromm, T. Ripken, W. Ertmer, G. Gerten, A. Wegener, and H. Lubatschowski, "Femtosecond laser induced flexibility change of human donor lenses," Vision Research **49**, 1853–1859 (2009).

17. H. Lubatschowski, S. Schumacher, M. Fromm, A. Wegener, H. Hoffmann, U. Oberheide, and G. Gerten, "Femtosecond lentotomy: generating gliding planes inside the crystalline lens to regain accommodation ability," J Biophotonics **3**, 265–268 (2010).

18. S. I. C. O. Santos, M. Mathew, and P. Loza-Alvarez, "Real time imaging of femtosecond laser induced nano-neurosurgery dynamics in C elegans," Opt. Express **18**, 364 (2009).

19. S. I. C. O. Santos, M. Mathew, O. E. Olarte, S. Psilodimitrakopoulos, and P. Loza-Alvarez, "Femtosecond Laser Axotomy in Caenorhabditis elegans and Collateral Damage Assessment Using a Combination of Linear and Nonlinear Imaging Techniques," PLoS ONE **8**, e58600 (2013).

20. A. Vogel, J. Noack, G. Hüttman, and G. Paltauf, "Mechanisms of femtosecond laser nanosurgery of cells and tissues," Appl. Phys. B **81**, 1015–1047 (2005).

21. T. R. Friberg and E. C. Karatza, "The treatment of macular disease using a micropulsed and continuous wave 810-nm diode laser," Ophthalmology **104**, 2030–2038 (1997).

22. J. K. Luttrull, "Subthreshold diode micropulse photocoagulation for the treatment of clinically significant diabetic macular oedema," British Journal of Ophthalmology **89**, 74–80 (2005).

23. M. B. Parodi, S. Spasse, P. Iacono, G. Di Stefano, T. Canziani, and G. Ravalico, "Subthreshold Grid Laser Treatment of Macular Edema Secondary to Branch Retinal Vein Occlusion with Micropulse Infrared (810 Nanometer) Diode Laser," Ophthalmology **113**, 2237–2242 (2006).

24. S. Sivaprasad, M. Elagouz, D. McHugh, O. Shona, and G. Dorin, "Micropulsed diode laser therapy: evolution and clinical applications," Surv Ophthalmol **55**, 516–530 (2010).

25. R. M. Kurtz, X. Liu, V. M. Elner, J. A. Squier, D. Du, and G. A. Mourou, "Photodisruption in the human cornea as a function of laser pulse width.," J Refract Surg **13**, 653–8 (1997).

26. T. Juhasz, F. H. Loesel, R. M. Kurtz, C. Horvath, J. F. Bille, and G. Mourou, "Corneal refractive surgery with femtosecond lasers," IEEE Journal of Selected Topics in Quantum Electronics **5**, 902–910 (1999).

27. G. M. Kezirian and K. G. Stonecipher, "Comparison of the IntraLase femtosecond laser and mechanical keratomes for laser in situ keratomileusis," Journal of Cataract & Refractive Surgery **30**, 804–811 (2004).

28. D. V. Palanker, M. S. Blumenkranz, D. Andersen, M. Wiltberger, G. Marcellino, P. Gooding, D. Angeley, G. Schuele, B. Woodley, M. Simoneau, N. J. Friedman, B. Seibel, J. Batlle, R. Feliz, J. Talamo, and W. Culbertson, "Femtosecond laser-assisted cataract surgery with integrated optical coherence tomography," Sci Transl Med **2**, 58ra85 (2010).

29. N. J. Friedman, D. V. Palanker, G. Schuele, D. Andersen, G. Marcellino, B. S. Seibel, J. Batlle, R. Feliz, J. H. Talamo, M. S. Blumenkranz, and W. W.

Culbertson, "Femtosecond laser capsulotomy," Journal of Cataract & Refractive Surgery **37**, 1189–1198 (2011).

30. E. J. Gualda, J. R. Vázquez de Aldana, M. C. Martínez-García, P. Moreno, J. Hernández-Toro, L. Roso, P. Artal, and J. M. Bueno, "Femtosecond infrared intrastromal ablation and backscattering-mode adaptive-optics multiphoton microscopy in chicken corneas," Biomedical Optics Express **2**, 2950 (2011).

31. L. Ding, W. H. Knox, J. Buhren, L. J. Nagy, and K. R. Huxlin, "Intratissue Refractive Index Shaping (IRIS) of the Cornea and Lens Using a Low-Pulse-Energy Femtosecond Laser Oscillator," Investigative Ophthalmology & Visual Science **49**, 5332–5339 (2008).

32. L. Xu, W. H. Knox, M. DeMagistris, N. Wang, and K. R. Huxlin, "Noninvasive Intratissue Refractive Index Shaping (IRIS) of the Cornea with Blue Femtosecond Laser Light," Investigative Ophthalmology & Visual Science **52**, 8148–8155 (2011).

33. L. J. Nagy, L. Ding, L. Xu, W. H. Knox, and K. R. Huxlin, "Potentiation of femtosecond laser intratissue refractive index shaping (IRIS) in the living cornea with sodium fluorescein," Invest. Ophthalmol. Vis. Sci. **51**, 850–856 (2010).

34. V. Hovhannisyan, A. Ghazaryan, Y.-F. Chen, S.-J. Chen, and C.-Y. Dong, "Photophysical mechanisms of collagen modification by 80 MHz femtosecond laser," Optics Express **18**, 24037 (2010).

35. K. Koenig, O. Krauss, and I. Riemann, "Intratissue surgery with 80 MHz nanojoule femtosecond laser pulses in the near infrared," Optics Express **10**, 171 (2002).

36. B.-G. Wang, I. Riemann, H. Schubert, D. Schweitzer, K. König, and K.-J. Halbhuber, "Multiphoton microscopy for monitoring intratissue femtosecond laser surgery effects," Lasers in Surgery and Medicine **39**, 527–533 (2007).

37. C. L. Hoy, N. J. Durr, P. Chen, W. Piyawattanametha, H. Ra, O. Solgaard, and A. Ben-Yakar, "Miniaturized probe for femtosecond laser microsurgery and two-photon imaging," Optics Express **16**, 9996 (2008).

38. T.-H. Tsai, S.-H. Jee, J.-Y. Chan, J.-N. Lee, W.-R. Lee, C.-Y. Dong, and S.-J. Lin, "Visualizing laser-skin interaction in vivo by multiphoton microscopy," Journal of Biomedical Optics **14**, 024034 (2009).

39. W. Denk, James H. Strickler, and W. W. Webb, "Two-Photon Laser Scanning Fluorescence Microscopy," Science **248**, 73–76 (1990).

40. M. Mathew, S. I. C. O. Santos, D. Zalvidea, and P. Loza-Alvarez, "Multimodal optical workstation for simultaneous linear, nonlinear microscopy and nanomanipulation: Upgrading a commercial confocal inverted microscope," Rev. Sci. Instrum. **80**, 073701 (2009).

41. A. Edelstein, N. Amodaj, K. Hoover, R. Vale, and N. Stuurman, "Computer Control of Microscopes Using μManager," in *Current Protocols in Molecular Biology*, F. M. Ausubel, R. Brent, R. E. Kingston, D. D. Moore, J. G. Seidman, J. A. Smith, and K. Struhl, eds. (John Wiley & Sons, Inc., 2010).

42. V. Hovhannisyan, W. Lo, C. Hu, S.-J. Chen, and C. Y. Dong, "Dynamics of femtosecond laser photo-modification of collagen fibers," Optics Express **16**, 7958 (2008).

43. L. Kessel, L. Eskildsen, M. van der Poel, and M. Larsen, "Non-Invasive Bleaching of the Human Lens by Femtosecond Laser Photolysis," PLoS ONE **5**, e9711 (2010).

44. A. C. Sen, N. Ueno, and B. Chakrabarti, "Studies on human lens: I. Origin and development of fluorescent pigments," Photochemistry and Photobiology **55**, 753–764 (2008).

45. D. M. Gakamsky, B. Dhillon, J. Babraj, M. Shelton, and S. D. Smith, "Exploring the possibility of early cataract diagnostics based on tryptophan fluorescence," J R Soc Interface **8**, 1616–1621 (2011).

46. S. Kalies, K. Kuetemeyer, and A. Heisterkamp, "Mechanisms of high-order photobleaching and its relationship to intracellular ablation," Biomed. Opt. Express **2**, 805–816 (2011).

Chapter 5: Image formation by linear and nonlinear digital scanned light-sheet fluorescence microscopy with Gaussian and Bessel beam profiles

5.1 Abstract

We present the implementation of a combined Digital Scanned Light-Sheet Microscope (DSLM) able to work in the linear and nonlinear regimes under either Gaussian or Bessel beam excitation schemes. A complete characterization of the setup is performed and a comparison of the performance of each DSLM imaging modality is presented using *in vivo C. elegans* samples and multicellular tumor spheroids.

5.2 Introduction

Traditional wide-field optical fluorescence microscopes are proven invaluable tools that accomplish the most diverse imaging tasks at the cellular and sub-cellular level. Nevertheless, when the systems (organisms or tissues) containing the fluorescent structures grow in size and complexity, traditional microscopy methods become limited or unusable. The main reason for this is that wide-field microscopes detect both the desired in-focus and undesired out-of-focus light. In a thick sample the high-resolution information from the focal plane can become "buried" in the blurred light from the surrounding tissue. The problem is more evident when the task involves following fast dynamical processes over time, with a limited amount of photons. That is why having an alternative technique that would allow the observation of fast events with high spatial resolutions over a large field of view (FOV) is extremely important. To overcome the problem of out-of-focus light, techniques referred as Laser point Scanning Microscopy (LSM), such as confocal and multi-photon microscopies, have been introduced [1]. LSM techniques generate images only from in-focus light providing intrinsic *optical sectioning*. Then, by digitally combining a stack of these images a three dimensional representation of the fluorescent sample can be obtained. In addition to out-of-focus light, another important issue to take into consideration when imaging biological samples is the photodamage (photobleaching and phototoxicity). In LSM techniques, as excitation and collection occurs along the

same axis, the entire sample is repeatedly irradiated when taking an image stack. As a consequence, cumulative photodamage is induced within the sample [2].

To overcome such problems, Selective Plane Illumination Microscopy (SPIM) was proposed [3]. In SPIM, a static sheet of excitation light is produced onto the sample plane using a cylindrical lens. Then, the fluorescence light emerging from this plane is collected through a microscope objective (MO) placed along the axis orthogonal to the excitation sheet. This uncoupling between the excitation and collection branches provides SPIM with: i) 2D optical sectioning capability in large fields of view that does not require point-scanning, and ii) decoupled resolution in the transversal and axial directions, determined by the collection numerical aperture (NA) and light-sheet thickness, respectively. Perhaps the most valuable benefit of this technique is the reduction of the photodamage to the sample, due to the restriction of the irradiation to the plane under observation [4]. Since it also can provide rapid acquisition speed, SPIM has emerged as a powerful tool for *in vivo* time lapse studies, from single cells to whole organisms and tissues [5]. Even though SPIM has proven to be a good alternative to conventional fluorescence microscopy methods, it still holds some drawbacks: i) a broadening of the light sheet deep inside the sample caused by scattering and aberrations, ii) the formation of stripe artifacts induced by absorption and scattering along the illumination axis, and iii) inhomogeneity of the sheet due to diffraction generated by the limiting diaphragm. Moreover, for having large FOVs, the depth of field in the cylindrical lens should be increased. This is achieved by using low NA lenses. However, this also reduces the optical sectioning capability of SPIM as the thickness (waist) of the generated cylindrical beam is increased. The balancing between both parameters has to be chosen carefully for the specimen of interest.

Recently Two-Photon Excited fluorescence Single Plane Illumination Microscopy (2p-SPIM) was demonstrated for imaging the pharynx of cameleon labelled *C. elegans* [6]. The use of two-photon excitation allows better out-of-focus light rejection, improving the quality of the optical sections and reducing the photodamage. These improvements rely on: i) the use of NIR excitation wavelength matching the optical window of biological samples and therefore allowing less sensitivity to scattering, better penetration depth, and reduced linear absorption; and

ii) the nonlinear nature of the absorption in TPEF virtually eliminates the conversion of the scattered excitation into fluorescence [7]. However, compared to two-photon LSM, in 2p-SPIM the total intensity of the nonlinear excitation beam is reduced as the beam is distributed over a plane as opposed to a single point. This drastically reduces the efficiency of fluorescence excitation.

Another interesting alternative implementation of SPIM (in which the beam is static) relies on the generation of the light sheet by scanning in one direction a focused Gaussian beam. This is termed as Digital Scanned (Laser) Light Sheet Microscopy (DSLM) [8,9]. There are several advantages to this implementation over widefield SPIM: i) The full power of the excitation light is concentrated into the single scanned line providing better illumination efficiency and lower exposure times, ii) Each line in the specimen is illuminated with the same intensity generating a homogenous light-sheet, where the height can be easily controlled with the amplitude of the scanning. Nevertheless the degrading effects of excitation scattering present in SPIM are inherited by DSLM. Further improvements were reported (Keller *et al*. [10]) by combining DLSM (and SPIM) with Structured Illumination (SI), with the aim to mitigate the blurring effects of the out-of-focus scattered light. In this approach the sheet is modulated to create sinusoidal patterns over the sample. Digital post-processing of the obtained images allows for the rejection of fluorescence generated by scattered excitation light, resulting in an enhanced optical sectioning and increased contrast. Multidirectional selective plane illumination microscopy (mSPIM) [11] has also been proposed to reduce absorption and scattering artifacts. In mSPIM the light sheet is i) rapidly tilted about the detection axes, and ii) sequentially directed onto the sample from two opposing directions, providing an evenly illuminated focal plane. The two images obtained are further combined by digital image fusion techniques [12]. Notwithstanding, for large and highly scattering samples, and due to the short excitation wavelength, some of the aforementioned problems remain: undesired intensity modulations, loss of resolution and limited penetration depth.

Recently, Truong et al. [13] reported on the use of a scanned light sheet microscope using TPEF (2p-DSLM) for live imaging of fruit fly and zebra fish embryos. They show the advantages of using 2p-DSLM for imaging large highly scattering samples

over the conventional 2p-LSM and 1p-DSLM. Basically, the use of TPEF increases the penetration depth, improves background rejection and reduces phototoxic effects. In addition, the line scanning configuration improves the excitation efficiency and increase the tolerance to aberrations. These advantages allow deep, fast, non-phototoxic imaging of living organisms. Another improvement that has been implemented in order to alleviate the deleterious effect of scattering on scanned sheet microscopy is the use of Bessel beams (BB) [14]. Self-healing properties of these beams allowed imaging 50% deeper inside human skin when compared with Gaussian beams. However, as side lobes of the BB normally introduce a certain amount of background signal to the images acquired, the use of confocal-line detection should be implemented. Another alternative is the use of high NA objective lenses to combine BB with both TPEF and SI. This technique was reported in terms of achieving enhanced isotropic 3D resolutions and was compared to other super-resolution techniques for imaging intracellular features in single cells in a small field of view [15].

In this paper we will show how 2p-DSLM combined with advanced spatial shaping of the beam, by using BB, can be used to improve the optical sectioning, the resolution and the intensity distribution uniformity of the light sheet in large fields of view and for moderately large specimens. This is compared with Gaussian beams in the nonlinear regime and with both Gaussian and BB in the linear regime. We present results on the system characterization and on imaging living *C. elegans*. To the best of our knowledge, this is the first time that 2p-DSLM has been combined with BB excitation to image multi-cellular organisms. The results are put in to context (and for reference purposes only), by producing an image stack using a well demonstrated and optimized SPIM imaging system [16] (in this case working at the excitation wavelength of 488 nm and having a standard GFP band-pass filter (GFP: 526/39) in the collection path).

5.3 Experimental setup

The optical setup we have implemented is shown in Figure 5.1 The *xy* plane is defined as the image plane (plane of interest) of the collection lens, and the *z* axis as the direction orthogonal to that plane along the direction where the fluorescence is

collected (see the inset of Figure 5.1). In our DSLM system, the excitation beam propagates along the *x* axis and the light sheet is generated in the *xy* sample plane by scanning the beam along the *y* direction using a galvo mirror GM. A telescopic system, composed of a scanning lens SL as well as a tube lens TLE, placed after the GM is such that i) the EO back focal plane and the GM axis plane are conjugates and ii) the effective numerical aperture of the lens EO (10×, NA= 0.3, WD = 16 mm, Nikon, Japan) is reduced to half its value, i.e., NA=0.15. This last condition is set to adapt the size of the Gaussian excitation beams to that given by the BB spectral ring. The collection objective lens CO (10×, NA= 0.45, WD = 4 mm) is placed with its axis orthogonal to the sample plane, along the *z* direction. A regular tube lens TLC, providing the objective "design" magnification is used to form an image of the fluorescent structures onto the CCD sensor (Orca R2, 6.45 μm pixel size, 1344x1024 pixels, Hamamatsu). The system can be configured to work in one of the following four modalities: i) linear DSLM with Gaussian beams (DSLM-Gauss), ii) nonlinear DLSM with Gaussian beams (2p-DSLM-Gauss), iii) linear DSLM with BB (DSLM-Bessel), and iv) nonlinear DLSM with BB (2p-DSLM-Bessel). The main excitation source for our DSLM system is a Kerr lens mode-locked Ti:sapphire laser (MIRA 900f, Coherent, France), emitting pulses of 160 fs duration, 76 MHz repetition rate and working at the central wavelength of 860nm.

For the nonlinear modalities the femtosecond laser beam is directly used for excitation. In these cases, the laser light is injected into the system through a couple of mirrors mounted on a translation stage S1. For the linear modalities S1 is set aside allowing the femtosecond-laser beam to enter an alternative optical path where a lens L1 focus the beam on a BBO Second Harmonic Generation (SHG) crystal (cut at 29.2º, 800 nm). A lens L2 is used to collimate the frequency doubled light (at 430nm) emerging from the crystal. For the modalities employing Gaussian beams, both the linear and nonlinear excitation beams reach the DSLM system without any further modification. Otherwise, for the modalities employing BB, an axicon (UVFS glass, apex angle 176º) and a lens L3 are inserted into the optical path by moving the translation stage S2. This combination is such that it produces the Fourier transform of the BB at the GM. This ensures that the BB is formed at the sample plane. To remove the interference of the lower spatial frequency components generated by the

round-tip defect of the axicon prism, a circular (opaque) stop is used [17,18]. This is placed at the back focal plane of the EO and coinciding with the BB Fourier plane given by L3. Filter F1 (BG-39) is used to cut the fundamental beam form the generated SHG light from the BBO crystal and F2 is a band-pass filter (CFP: 479/40) used to cut the excitation light from the fluorescence images. The specimen under observation is mounted on a holder with six degrees of freedom that allows for a fine adjustment of position and tilt with respect to the excitation sheet. The holder is mounted upon a computer-controlled linear translational stage (M-505.6DG, Physik Instrumente GmbH & Co. KG, Karlsruhe, Germany) that scans the sample along z direction.

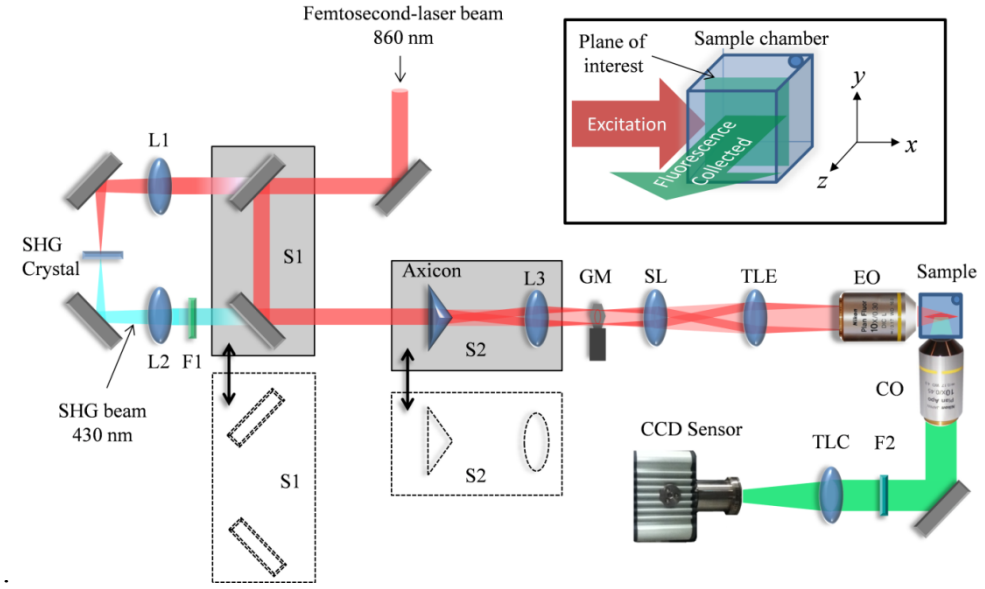

Figure 5.1: Schematic diagram of our DLSM setup.
The translation stage S1 allows switching between linear DSLM, where the beam pass through the SHG crystal and lenses L1 and L2, and 2p-DLSM where the femtosecond-laser beam pass unmodified. Gaussian or Bessel beams are selected by moving the translation stage S2 that contains an axicon and the Fourier transforming lens L3. A galvo mirror GM, a scan lens (SL), a tube lens (TLE) and an excitation objective lens (EO) are used to create the light sheet with the desired properties at the sample plane. The fluorescence generated in the sample is collected at 90 degrees by a collection objective lens (CO) and a regular tube lens (TLC) that forms image onto the CCD sensor with the designed magnification. Filters F1 and F2 are used to cut off the excitation light from the fluorescence images collected. The inset (top-right) shows the excitation-collection geometry that defines the notation of the axes used in this work

5.4 Results 1: *in vivo C elegans* imaging

5.4.1 Samples prepararation

5.4.1.1 Coumarin/fluorescent beads

For characterization of the system two different samples were employed: i) A quartz cuvette filled with a solution of Coumarin 540 dissolved in methanol to a concentration of 0.5 mmol and ii) a solid agar sample containing 0.5 μm diameter green fluorescent beads (G500, solution 1% solids Duke Scientific Corp., USA). For the latter, a 1:10 bead-water solution was created. This was then mixed 1:100 with melted 2% agarose. Then, a 200μl drop of the bead-agar solution was cooled to room temperature on a glass slide for 10 minutes. Once the agar was solidified, a 90° corner was cut. The coverslip with the cut agar was mounted on the holder with one of its face pointing towards the excitation lens and the other towards the collection lens. This configuration allows that all excitation and imaging to be performed using air objectives.

5.4.1.2 Worm samples

To test the system for biological applications, samples containing one or more *Caenorhabditis elegans (C. elegans)* nematodes were prepared. At the beginning, adult hermaphrodite worms were immobilized into a 5μl drop of sodium azide (NaN_3, 25 mM) for 10 minutes. The worms were then picked and mounted on top of a 5mm thick agar (at 2%) bench to preserve them properly hydrated. As in the case of the fluorescent beads, this configuration allowed us to image the worms using air objectives. We employed a genetically modified strain of *C. elegans* expressing the fluorescent protein "cameleon" in the pharynx. This protein is normally used as calcium indicator for imaging calcium transients in intact *C. elegans* [19]. It is composed of four domains, cyan fluorescent protein (CFP), calmodulin, M13 (a calmodulin binding domain), and yellow fluorescent protein (YFP). In our experiment, only CFP fluorescence was excited as this is convenient to visualize the whole pharynx. Furthermore, since the worms were anesthetized no calcium transients were expected.

5.4.2 System characterization

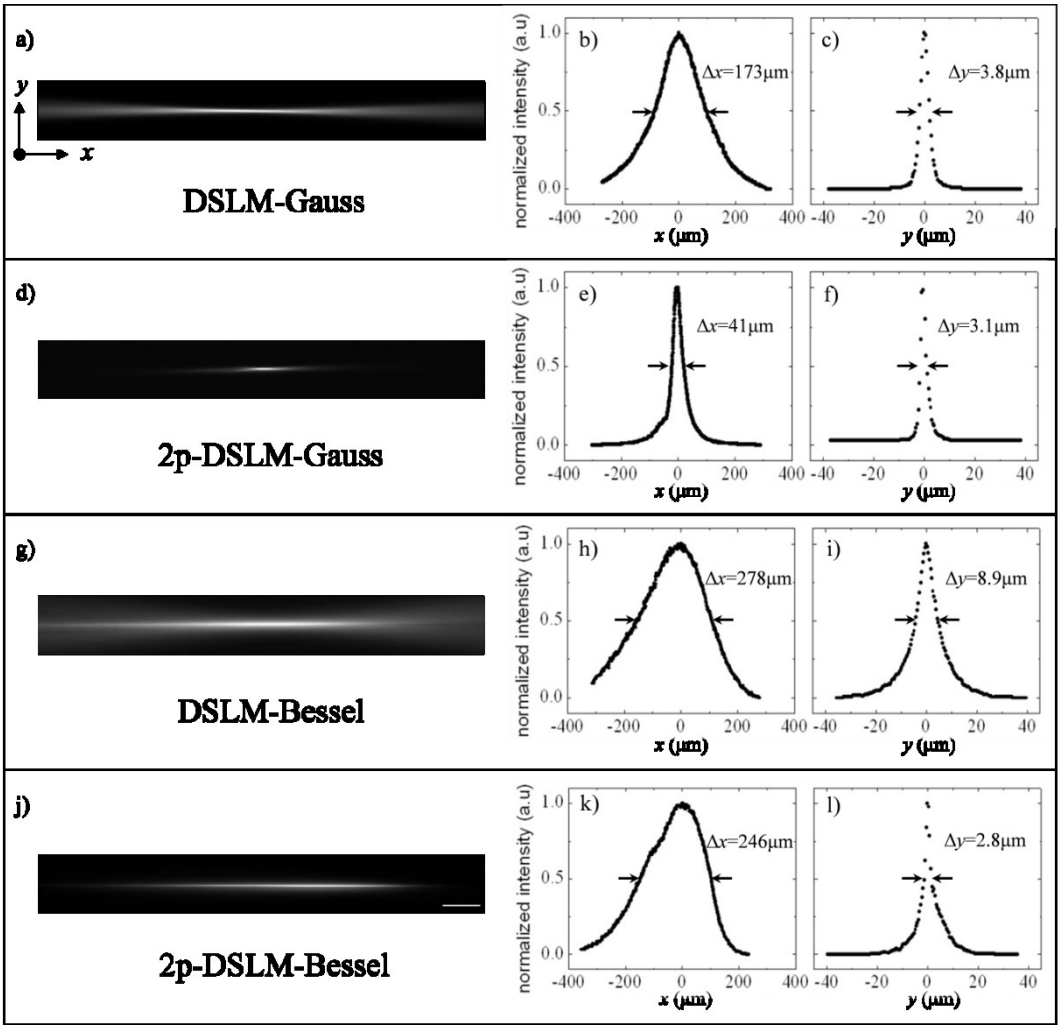

Figure 5.2: Normalized fluorescence images and intensity profiles along x and y for the different excitation beams.
a-c) DSLM with Gaussian beams, d-f) 2p-DSLM with Gaussian beams, g-i) DSLM with BB and j-l) 2p-DSLM with BB. The FWHM widths are indicated between arrows for each modality and their corresponding values Δx and Δy are included. These values are also summarized in Table 5.1. Profiles were taken along x and y directions with the point of maximum intensity located at the origin of coordinates, see the reference axes in Figure 5.1(a). Scale bar: 50 μm, a pixel of the image corresponds to 0.44 μm in the sample.

We performed two sets of experiments to characterize the four modalities available in our system i) measurement of the dimensions of the fluorescent line excited by the light beam and ii) determining the resolution of our system by measuring the transversal and axial dimensions of the point spread function (PSF) of each modality of the system. For this work, we use the full-width-at-half-maximum (FWHM) of the normalized intensity profiles along the axis of interest and centred at the point of

maximum intensity to characterize the dimensions of the different intensity distributions.

The first set of experiments was performed by using a Coumarin solution sample as described in section 3.1. For this, the GM was set to be static and the fluorescent line generated into the sample was imaged on the CCD camera. The images of the excitation lines and the extracted profiles along x and y axes are presented in the Figure 5.2 for each modality: a-c) DSLM-Gauss, d-f) 2p-DSLM-Gauss, g-i) DSLM-Bessel and j-l) 2p-DSLM-Bessel. The FWHM widths Δx and Δy obtained from the profiles are shown over each plot and are summarized in Table 5.1. From Figure 5.2 it is possible to see that when using Gaussian beams in the nonlinear regime (2p-DSLM), an important decrease of the length of the usable FOV occur (down to 0.25× compared with linear DSLM). Nonetheless, for the linear case a considerable amount of background is added from the fluorescence excited outside the Rayleigh range of the beam (see Figure 5.2(a)). Then, a hard aperture is required to exclude the "tails" by either matching the Rayleigh range of the beam to the CCD sensor or by direct clipping of the usable FOV with a custom made limiting pupil.

On other hand, the modalities using BB show an increased FOV evidenced by the increment of the width along x dimension (see Figure 5.2(h) and Figure 5.2(k)). Interestingly, the line width Δy shows little variation among all modalities, except for the case of linear excitation with BB where it becomes more than 2x ticker when compared with the case using Gaussian beams, as shown in Figure 5.2(i). In addition, Figure 5.2(g) shows that for the linear case the blurring of the tails outside the usable FOV get worst when using BB. This would be solved by the use of a hard clipping procedure as described before for the case of Gaussian beams. This is in contrast with the two photon based modalities, Figure 5.2(d) and Figure 5.2(j), where the tails are naturally non existing by the confined nature of the nonlinear excitation. Also, it is worth noting that by using BB the intensity profile along the x direction is asymmetric for both linear and nonlinear modalities as can be appreciated in Figure 5.2(h) and Figure 5.2(k). This effect has been observed before for ideal refractive axicons where a slower decay rate is expected for the points farther from the axicon tip (see for example Akturk *et al.* [17]). In addition to this, the 2p-DSLM-Bessel

image shows some irregularities within the FWHM. Such imperfections in the axial profile are attributed to the mask to remove the low spatial frequency components generated by the imperfect tip at the Fourier spectrum of the BB [17,18]. This mask was chosen in order to give the best trade-off between optical transmission and beam homogeneity in the 2p-DSLM-Bessel configuration. Therefore the small defect observed in Figure 5.2(k) can be attributed to undesired angular frequencies that remain after filtering.

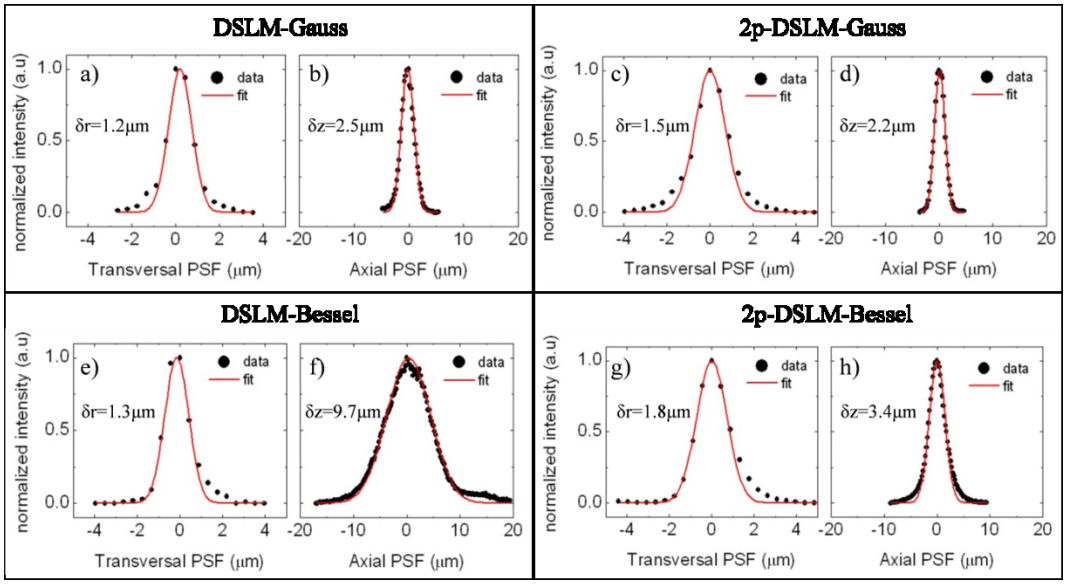

Figure 5.3: Example of the PSFs obtained for the system using a sample of fluorescent beads in agar.
The experimental intensity profiles (black dots) and Gaussian fits (red lines) for both transversal (δr) and axial (δz) dimensions are shown for the different modalities: a, b) DSLM with Gaussian beams, c, d) 2p-DSLM with Gaussian beams, e, f) DSLM with BB and g, h) 2p-DSLM with Bessel beams. The FWHM widths calculated from the Gaussian fit are shown over each graph. The average values of the PSF widths for 5 beads are reported in the Table 5.1.

Table 5.1: Summary of the FWHM widths measured for the light lines (Figure 5.2) and for the PSFs of the system (Figure 5.3).
An error of one pixel was assumed on the light lines. The mean value and statistical error in the PSFs was obtained over 30 measurements.

Modality	Dimensions of the fluorescent light line		PSF from fluorescent beads	
	Δx (μm)	Δy (μm)	Δr (μm)	Δz (μm)
DSLM-Gauss	173	3.8±0.4	1.2±0.2	2.6±0.5
2p-DLSM-Gauss	41	3.1±0.4	1.5±0.2	2.3±0.1
DSLM-Bessel	278	8.9±0.4	1.3±0.1	10.7±0.9
2p-DSLM-Bessel	246	2.8±0.4	1.4±0.2	3.2±0.3

This defect was not observed in the DSLM-Bessel image (Figure 5.2(i)) due to: i) small differences of the spatial frequency spectra at the filtering plane, that make the BB generated with the SHG and femtosecond-laser beams to be slightly different, and ii) the background generated by the BB side lobes that masks any perturbation induced in its axial intensity profile. A second set of experiments was performed in order to measure the size of the transversal (δr) and axial (δz) PSFs of the four DSLM modalities. For this, we employed a sample of beads immersed in agar as described in section 3.1. For each modality, a stack of images was recorded by moving the sample in steps of 0.2 μm along the *z* direction, capturing one image per step. For each image stack, several (~30) beads in the centre of the FOV were selected and cropped to isolate their individual volumetric intensity distributions. In all cases, the brightest voxels of the intensity distributions were found and the intensity profiles were selected along the three reference axes of maximum intensity. The intensity distributions were fit to a Gaussian function and the FWHM values were calculated. Some examples of the intensity profiles and the Gaussian fits obtained for each modality are shown in Figure 5.3. The results are summarized in the Table 5.1. To obtain the transversal PSF width δr, we used both *x* and *y* measurements as $\delta r = 0.5(\delta x + \delta y)$. It has been shown that the transversal resolution of a SPIM system depends exclusively on the optical properties of the collection lens, whereas the axial resolution is determined by both detection lens an*d* the light-sheet thickness [20]. Therefore, we expect to have a similar transversal resolution for all the modalities and a diversity of axial resolutions dependent on the thickness as well on quality of the light-sheet for each modality. This is precisely what we have found in our experiments: As can be seen from the Table 5.1, although the transversal resolution is slightly better in both linear DSLM modalities, they are all very similar. This is not the case for the axial resolution, which is found to be different for each of the modalities and smaller in the nonlinear regimes. Also, as expected, there is a clear correlation between the light-sheet thickening and the axial resolution degradation, as is revealed by comparing Figure 5.2 (c), (f), (i), and (l) with Figure 5.3(b), (d), (f), and (h), Table 5.1 columns Δy and δz. All these indicate that when imaging we should expect better axial resolution when DSLM in the

nonlinear regime is performed. This should also be the case when imaging biological samples, a hypothesis that we verify in a series of experiments using fluorescently labelled *C. elegans* pharynxes.

Table 5.2: Summary of the experimental parameters employed to collect the data supporting Figure 5.4 .

Modality	Parameters					
	Objectives		Wavelength (nm)	Avg. power (mW)	Integration Time (ms)	z step (μm)
	Excitation	Collection				
SPIM	Air, Leica 5×/0.12 NA Plan Epi	Water, Leica 10×/0.3 HCX APO	488	<1	500	2
DSLM-Gauss	Air, Nikon 10×/0.15NA, Plan Fluor (nominal NA=0.3)	Air, Nikon 10×/0.45NA, Plan Apo	430	2	180	2
2p-DLSM-Gauss			860	58	220	2

5.4.3 *C. elegans* imaging

We started by imaging the pharyngeal muscle of *C. elegans* expressing the Cameleon fluorescence protein in a conventional SPIM setup, where the light sheet is formed via a cylindrical lens. This conventional SPIM technique [16] has proven to be useful for a number of samples including chick and mouse tissue and organs, *Drosophila* embryos and for imaging zebrafish development [21] and *C. elegans*. The results obtained with *C. elegans* are used as a reference for our different DSLM images obtained using Gaussian beams (DSLM-Gauss and 2p-DSLM-Gauss). The different experimental conditions are listed in the following Table 5.2 and Figure 5.4 shows the results of such comparison.

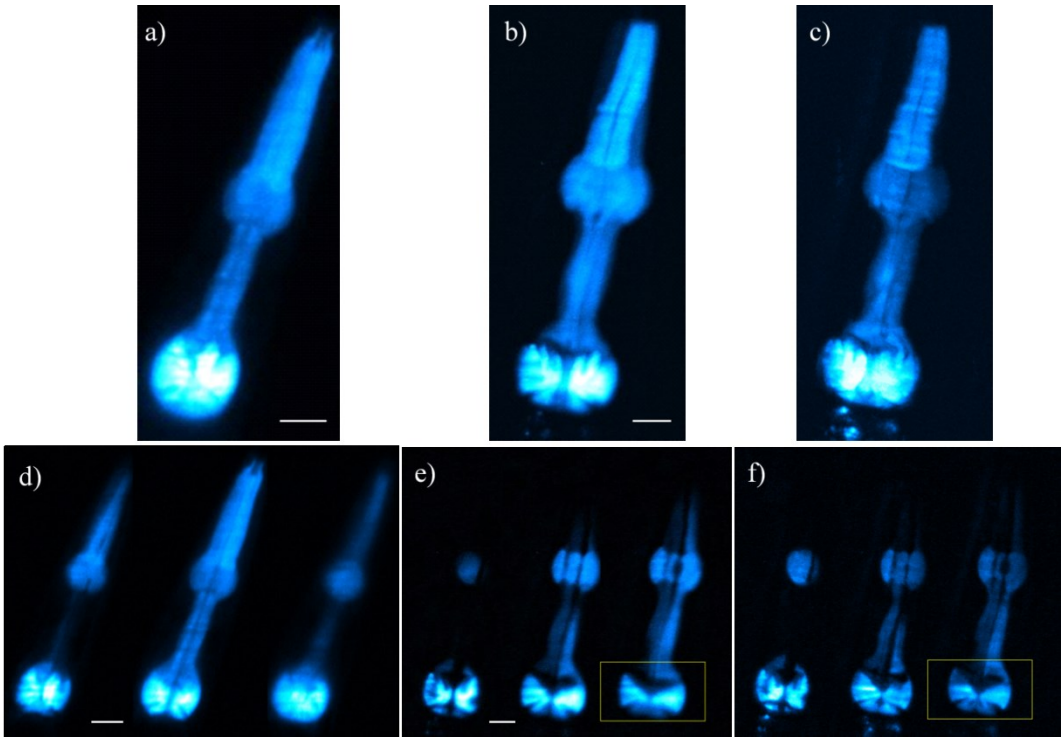

Figure 5.4: Images of a CFP-fluorescent pharynx of a *C. elegans.*
Figures (a-c) are maximum intensity projections (MIP) of z stacks taken with a) the reference state-of-the-art SPIM system, b) DSLM-Gauss and c) 2p-DSLM-Gauss . Figures d) to f) show some individual sections of the z stacks obtained with SPIM , DSLM and 2p-DSLM modalities using Gaussian beams, respectively. All z-stacks are composed of 54 images taken in steps of 2 μm. Scale bars: 20 μm.

Figure 5.4(a-c) show the maximum intensity projection (MIP) and optical sections obtained from the pharynx region of the nematode using the standard SPIM, DSLM-Gauss and 2p-DSLM-Gauss techniques, respectively. By comparing these figures it is possible to see that similar results are obtained for both SPIM and DSLM techniques. However, by directly comparing, Figure 5.4(d-f), it is appreciated that in the two-photon images the pharynx appears less blurry and some details are better discriminated.

with 1p-DSLM using Gaussian beams with lower integration time and using very low (<1mW) excitation power.

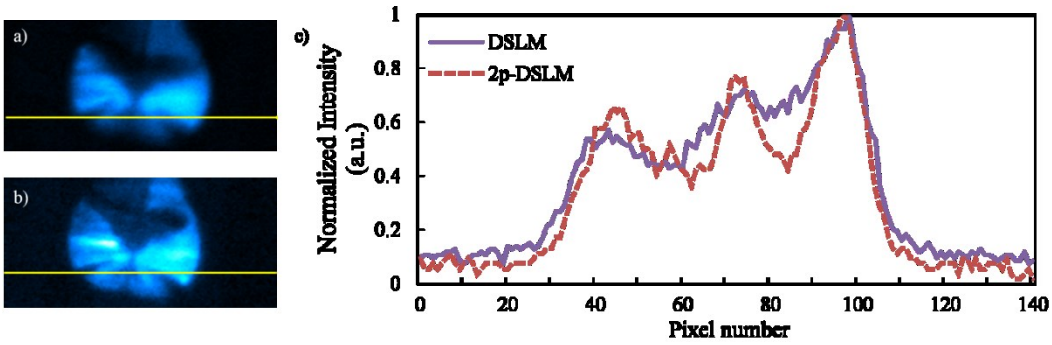

Figure 5.5: Example of the contrast enhancement obtained by using 2p-DSLM.
Regions of interest (ROI) taken from single optical sections (yellow squares on Figure 5.4) for a) DSLM and b) 2p-DSLM. c) Plot of the intensity profiles along the selected lines for both modalities. Intensity values of the plots have been normalized to the maximum of each distribution

To quantify the results obtained with our DSLM system, we provide a plot of the intensity profiles along a line on the fluorescent structures. This has been done for the same worm (and therefore, the same pharynx) as well as for the same optical sections for both modalities, see yellow marked ROIs in Figure 5.4 (e) and (f) that correspond to Figure 5.5(a) and (b), respectively. In this way, a proper quantification of the local intensity and the background signal is obtained. The results can be seen in Figure 5.5. By looking at Figure 5.5(c), it is possible to see that the 2p-DSLM presents a reduced background. In addition, some structures show higher modulations, indicating higher contrasts.

We then proceed to test the use of BB to explore their impact on the length of the FOV. For this we prepared a sample of several worms, all in the same plane and aligned in a row along the direction of incidence (x) of the excitation beam (Figure 5.6(a)). For the four cases the beam was scanned to the amplitude that generates a light sheet that fills the entire FOV in the y direction. The experimental parameters employed to obtain the images of the Figure 5.6 are outlined in Table 5.3. It shows that the longest CCD integration time, and the highest excitation power levels correspond to 2p-DSLM with BB, whereas the same signal level can be obtained

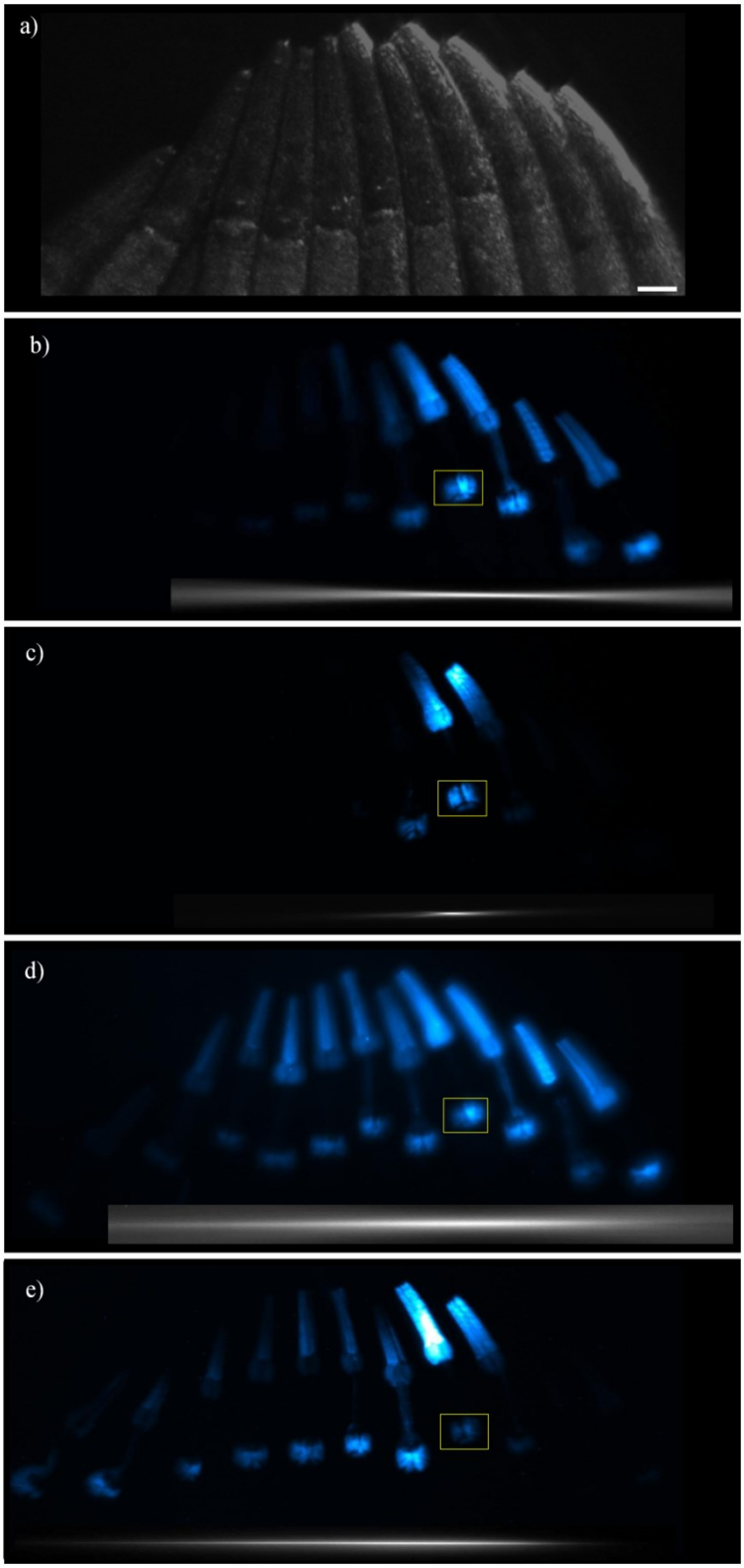

Figure 5.6: Multimodal images of a row of *C. elegans* aligned along the x direction.
Figure a) shows the sample configuration as a reference (image taken using oblique illumination). Figures (b-e) are maximum intensity projections of *z* stacks taken with the four modalities available in our setup: b) DSLM-Gauss, c)

2p-DSLM-Gauss, d) DSLM-Bessel and e) 2p-DSLM-Bessel. The insets below each image indicate the position and extension of the excitation focal lines of Figure 5.2. All *z*-stacks are composed of 50 images taken in steps of 2 μm. Scale bars: 50 μm.

The results are shown in Figure 5.6(b-e), where maximum-intensity-projections of the z stacks are shown for all of our DSLM configurations. Also, the previously obtained excitation focal lines (see Figure 5.2) were included below each figure as an indication of the expected effective FOV. From Figure 5.6 it is possible to see the increase of the FOV in the x direction by using BB, in both linear and nonlinear modalities. Note that this is remarkably extended in the nonlinear regime (compare Figure 5.6(c) and (e)). Now, in terms of image homogeneity the DSLM-Bessel gives better results when compared to any other modality, as seen in Figure 5.6(d). However, the generated image is more blurry due to the side lobes characteristic of the BB. This is in agreement with our characterization results presented in Figure 5.2(i) and Figure 5.3(f). Finally, both DSLM-Gauss and DSLM-Bessel images require hard clipping in the collection path to eliminate the signal from the extremes of the generated beams. This can be clearly seen in the first and last worms in Figure 5.6(b) and (d). This is not the case for the nonlinear techniques in which the image at the effective FOV is in focus showing sharper details (Figure 5.6(c) and (e)).

Table 5.3: Summary of the experimental parameters employed to collect the data supporting Figure 5.6.

Modality	Parameters			
	Wavelength (nm)	Avg. power (mW)	Int. time (ms)	*z* step (μm)
DSLM-Gauss	430	<1	2000	2
DSLM-Bessel	430	<1	2000	2
2p-DLSM-Gauss	860	72	2000	2
2p-DLSM-Bessel	860	290	3000	2

To quantify these results, optical sections were selected from the stack of images for each image modality at the ROIs marked in Figure 5.6, as it is shown in Figure 5.7(a-d). A plot of the intensity profiles along the lines drawn in the optical sections is provided in Figure 5.7(e). From this figure it is possible to see that the DSLM-Bessel case produces the largest generated fluorescence intensity. However, the optical sectioning is badly affected by the side lobes of the BB, causing a complete blurring

of the details. In addition (and similarly to Figure 5.5), we also found that both 2p-DSLM modalities allows for better contrast of the different sample structure, as well as a reduced background.

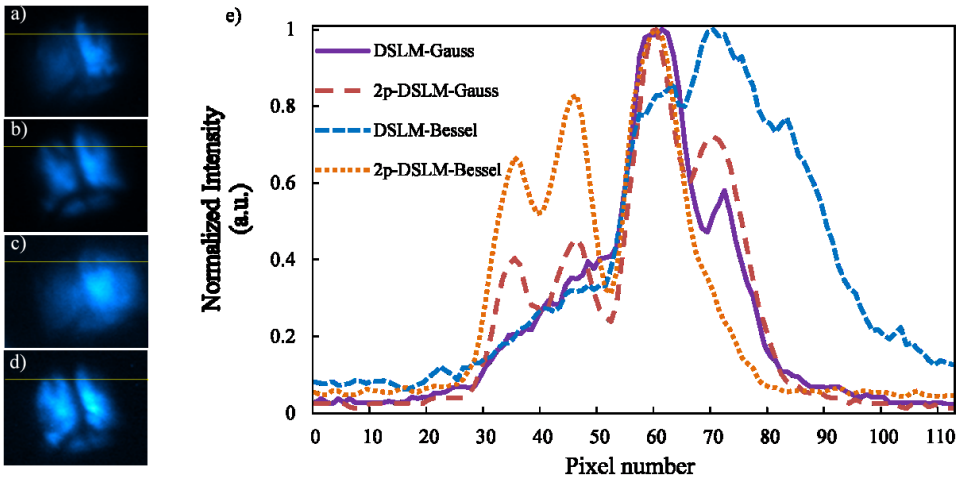

Figure 5.7: Normalized profiles along a selected line taken from approximately the same optical section for all the DSLM modalities.
Optical sections showing the same ROI and the selected line in yellow for a) DSLM with Gaussian beams, b) 2p-DSLM with Gaussian beams, c) DSLM with Bessel beams, and d) 2p-DSLM with Bessel beams. Plots of the intensity profiles along the selected lines are shown in e). Intensity of each plot has been normalized to its respective maximum value.

5.5 .Results 2: Multimodal DSLM with large FOV for thick samples 3D imaging

In the last section we have shown that 2p-DSLM-Bessel is an effective way to increase the FOV of a light-sheet microscope without giving up resolution and increasing the effective contrast of the optical sections captured. For this proof-of-principle demonstration we employed *C. elegans* that helped us to show that the proposed method allows *in vivo* imaging. From an optical point of view these samples can be considered thin and transparent, despite the last experiment shows a row of worms aligned in a row that resembles a thick sample for the excitation beam. On the other hand, the light-sheet microscope we have built was scaled to deal with medium to large sized samples (a few hundreds of microns) that are considered thick for optical microscopy. Thus, in order to show the full potential of the developed optical system more appropriate samples were utilized.

5.5.1 Multi-cellullar tumor spheroids (MCTS)

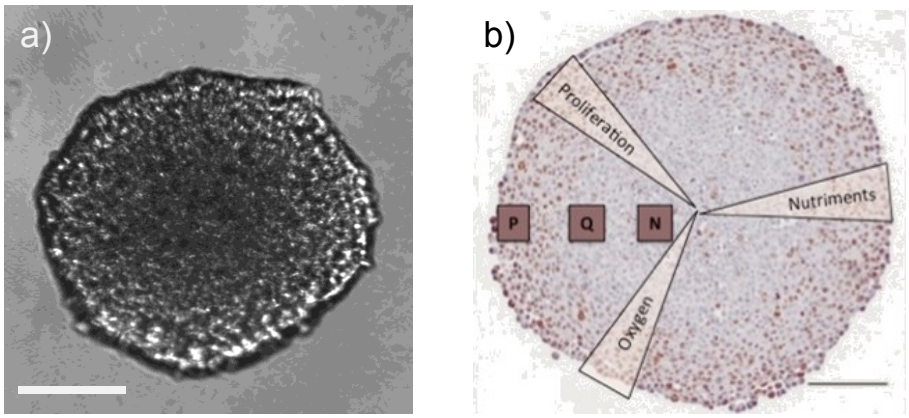

Figure 5.8:Morphology of MCTS.
a) White light image of a MCTS. b) Proliferation, hypoxia and nutrients gradient within a spheroid. P, Q and N stand for Proliferative, Quiescent and Necrotic zones respectively. Scale bars 50 μm.

MCTS are aggregates of cells with spherical symmetry that are analogous to tissues, see Figure 5.8(a). They are constructed without any external scaffolds, taking advantage of the natural tendency of many cell types to aggregate. MCTS are built making adhesive forces between cells greater than the adhesive attraction to the substrate on which the cells are plated [22]. Compared to conventional monolayer cultures, MCTS mimic tumors *in vivo* in many ways, such as the expression of antigens, oxygen gradients within its microenvironment, penetration rate of growth factors and distribution of proliferating/quiescent cells within the spheroid (Figure 5.8(b)). MCTS have important applications for bioenginnering of tissues [23], high-throughput drug testing [24] , and the modelling of cell dynamic processes inside tumors [25], among others.

In contrast to the many studies that are reported on cell cycle and cell proliferation, spatio-temporal dynamics of tumor cell proliferation in complex 3D systems such as spheroids is a young field that is still in development. The challenges for retrieving relevant biological information in MCTS involve getting an imaging system capable of an excellent signal-to-noise ratio, optical sectioning capability, large field of view, good spatial resolution, a fast image stack recording rate and an extremely low sample fluorophore excitation level is required [26]. Although modern fluorescence microscopy, particularly SPIM with its different variants, has the potential to fill in all these, optical imaging inside large spheroids remains technically very

challenging. MCTS can grow to diameters of several hundred micrometers and the optical interrogation of internal structures will be degraded by aberrations and scattering. In SPIM, some works have reported sharper and more contrasted images by implementing adaptive optics in the emission path, either by using a wavefront sensor [27], an optimization algorithm [28] or a model-based correction [29]. Scattering degrade the usability of SPIM microscopes by reducing the penetration depth of the excitation light and by degrading the image quality on the emission path. The DSLM system we have built is very promising as it has the potential to partially mitigate (in the excitation path) the effects of scattering as combine two-photon excitation and Bessel beams. NIR laser beams utilized for two-photon excitation are less sensitive to scattering. Bessel beams have self-healing properties that enables a more robust propagation through samples with strong refractive index heterogeneities, as is the case of MCTS. In the following, the performance of the different DSLM modalities will be tested by using biologically-relevant fluorescently-labelled MCTS.

5.5.2 MCTS samples

Colorectal cancer cells line HCT116 were cultured in DMEM+GlutaMAX (Dulbecco's Modified Eagle Medium; Gibco) supplemented with 10% fetal bovine serum and 1% penicillin–streptomycin (Pen Strep; Gibco), and maintained at 37°C and 5% CO_2 in an incubator. MCTS were prepared in 96-well plates that were coated with 20 mg/ml polyHEMA (Sigma). Cells were plated at a density of 600 cells/well in 100 µl cell culture medium per well then centrifuged to allow spheroid formation. After 4–5 days growth, MCTS of 400–600 µm diameter were collected, washed three times with PBS and then fixed with 10% neutral buffered formalin (Sigma–Aldrich) at room temperature for 4 hours. MCTS in formalin were washed three times and stored in PBS.

For this work we have employed two kinds of MCTS: i) Sulfo-rhodamine B (SRB) stained, non-specific, that provides a sample with uniform fluorescence, and, ii) MCherry-H2B expression, that allows to visualize the chromosomal architecture.

5.5.3 Modification of the multimodal DSLM optical setup

In order to have a system more suitable for experimenting with thicker and more challenging samples we have modified the original setup as follows: i) the SHG crystal was removed as a source of 1p excitation in order to enhance the versatility of the system, as are three new visible lasers at 405, 488 and 532nm; ii) we have also included an additional 2p excitation line at 1044nm (Time-Bandwidth SESAM, 1040nm, 250fs) to allow imaging samples that are red fluorescent; iii) the immersion chamber was redesigned to accommodate a water dipping collection objective (Leica/HCX apo L20X, 0.5NA) that increased the resolution of the system, the magnification was set 25x using the appropriate tube lens; iv) the sample holder was modified to include a custom made capillary holder attached to a motorized rotation stage and a three axis motorized stage (Thorlabs 3-axis NanoMax, Physik instrumente M-116.2SH) allowing full computerized control of the experiments; v) the CCD sensor was replace for a last-generation CMOS sensor (Hamamatsu ORCA-Flash 4.0) that allows for increased sensitivity, larger FOVs and faster detection.

5.5.4 System characterization

Table 5.4: Summary of the characterization of the system for MCTS imaging.

Modality	Dimensions of the fluorescent light line		PSF	
	Δx (μm)	Δy** (μm)	Δr (μm)	Δz (μm)
DSLM-Gauss	260	4.1	1.0	3.5
2p-DLSM-Gauss	220	4.9	1.0	3.0
DSLM-Bessel	480*	1.5	1.0	5.0
2p-DSLM-Bessel	480*	3.1	0.9	2.5

*Full FOV covering was assumed. **FWHM of the beam profiles.

The optical setup was optimized to get large FOVs for the four modalities available in order to fit the size of the MCTS employed. The system was characterized using the same methodology employed in the first section of this chapter. In order to estimate the usable FOV and the light sheet thickness we employed an agar cylinder stained with Sulfo-Rhodamine B. The PSF sizes were measured using 1μm red fluorescent microbeads inside MCTS, the minimum value encountered was used as a reference. The summary of the results can be found in Table 5.4. As it can be appreciated in this table some values have changed as compared with Table 5.1. This

is expected as we changed the collection objective and the length of the light beams, as mentioned in the last section.

5.5.5 Propagation of the excitation beams inside the MCTS

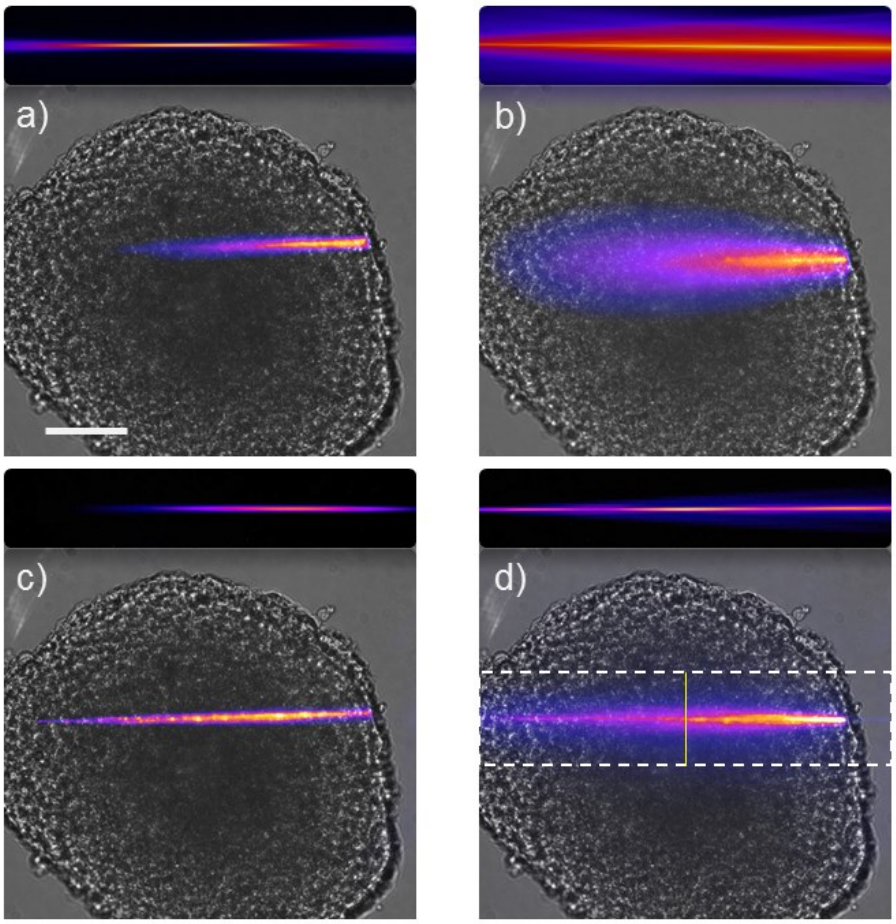

Figure 5.9: Propagation of the beams inside a MCTS.
Figures show the normalized intensity of the SRB fluorescence signal excited by parking the excitation beam at the center of the MCTS for a)1p-DSLM-Gauss, b) 1p-DSLM-Bessel, c) 1p-DSLM-Gauss, and, d) 2p-DSLM-Bessel, respectively. For comparison, the original profile of the excitation beam is shown in the upper part of each image. Beams propagate from right to left in the images. Background is a white light image of the MCTS employed for this demonstration. Solid yellow line in d) indicates one of the lines used for the fits employed to plot the profiles in Figure 5.10(b-c). As an example, to obtain the profile 2p-DSLM-Bessel, all vertical lines between the dotted white lines have to be fitted with the functions mentioned in the text.

To test the behavior inside the MCTS, we imaged the fluorescence excited by the different beams propagating through the same MCTS measuring 400µm and stained with the Sulfo- Rhodamine B. The MCTS was positioned in such way that the different beams enter the spheroid approximately at the same position, centered in the z axis so that the emitted fluorescence travels about 200 µm inside the MCTS.

Figure 5.9 shows the results obtained for the different beams. By comparing the original reference beams that are show on top of each image one can observe that the beams are affected to some degree by scattering when they propagate through the MCTS. In order to get a quantitative comparison between the different modalities we have employed an approach consisting on fitting line-by-line (see for example yellow line in Figure 5.9(d)) the intensity images of each beam intensity distribution profile to obtain the changes both in the intensity and the width of the excitation. For the case of Gaussian beams the fit was done to a biased Gaussian function. For the Bessel modalities we employed a function that is a biased Gaussian term plus a $sinc^2$ term. In the Bessel modalities, the Gaussian term accounts for the broadening and averaging of the beam while propagates trough the MCTS while the $sinc^2$ term accounts for the non-diffracting component of the beam during propagation. The results are shown in Figure 5.10.

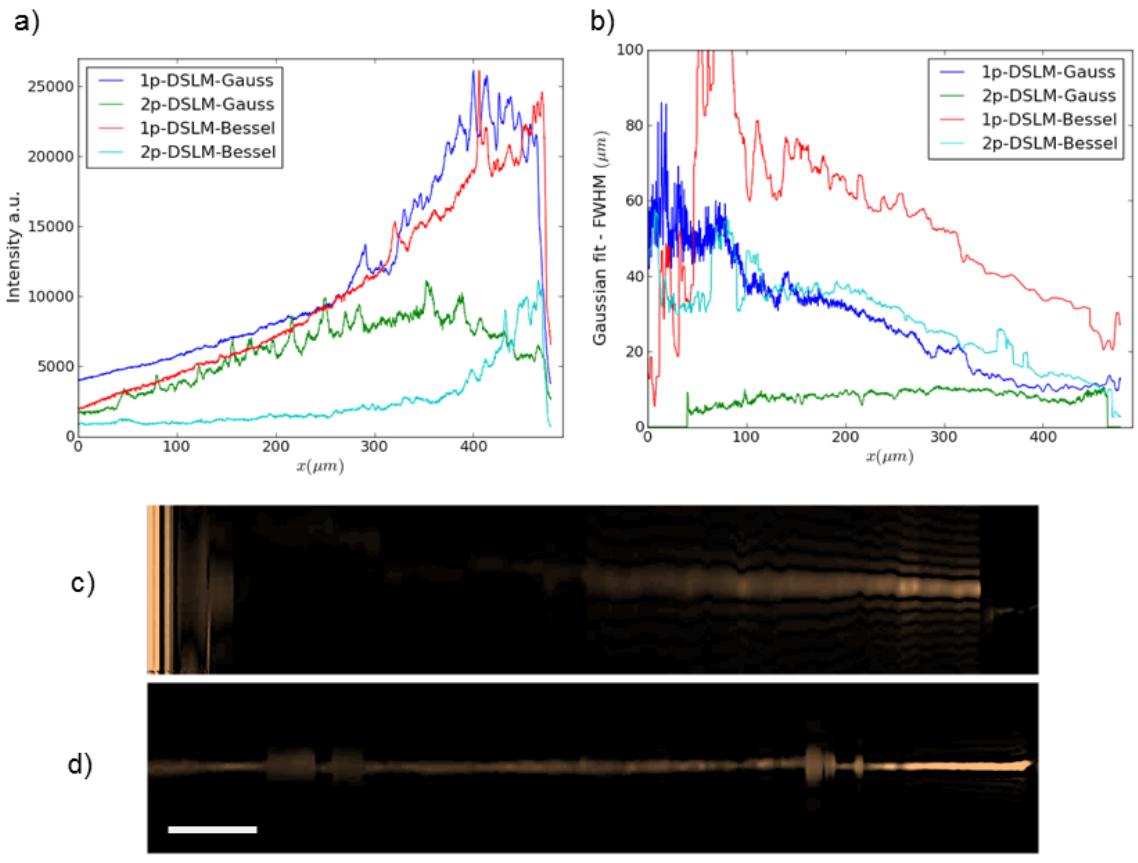

Figure 5.10: Analysis of the propagation of the DSLM excitation beams.
a) Intensity profiles of the four beams (intensities of 2p modalities were scaled 4x for better visualization). b) FWHM width of the Gaussian component of the fit of the four beams(see main text for further explanation). The evolution of the

$sinc^2$ fitting component of c)1p-DSLM-Bessel and d) 2p-DSLM-Bessel, respectively.

Figure 5.10(a) shows the intensity profiles of the different beams upon propagation inside the MCTS. All of them present a characteristic exponential decay as expected from Beer´s law, except the beam corresponding to the 2p-DSLM-Gauss modality that follows up to some point the original intensity distribution (compare green line in Figure 5.10(a) and Figure 5.9(a) up). The maximum intensity shows a substantial decrease when using two photon modalities, as expected. Figure 5.10(b) shows the Gaussian component of the line-to-line fit to the profiles. All of them show a monotonically increasing width of the Gaussian component upon propagation, except again by the beam corresponding to the 2p-DSLM-Gauss modality, that remains constant. Figure 5.10(c) and (d) show images of the $sinc^2$ components of both Bessel modalities. It is clear from the images that Bessel component of 1p modality is broader and extinguish much faster than its 2p counterpart that remain practically invariant along the full FOV. This can be interpreted as the combined effect of less sensitivity to scattering provided by the use of NIR wavelengths and the self-reconstructing properties of Bessel beams.

5.5.6 Imaging of biologically relevant MCTS

Once we have characterized our modified multimodal DSLM system with uniformly stained MCTS, we perform some imaging experiment in order to produce high resolution 3D images of fluorescent MCTS. MCTS with H2B-MCherry expression generated from cancer cells are interesting models to study the influence of malignant cell-interactions on cellular proliferation, differentiation, apoptosis and gene expression. H2B-MCherry allows the observation of both mitotic chromosomes and interphase chromatin revealing various chromatin condensation states of the cells within the MCTS.

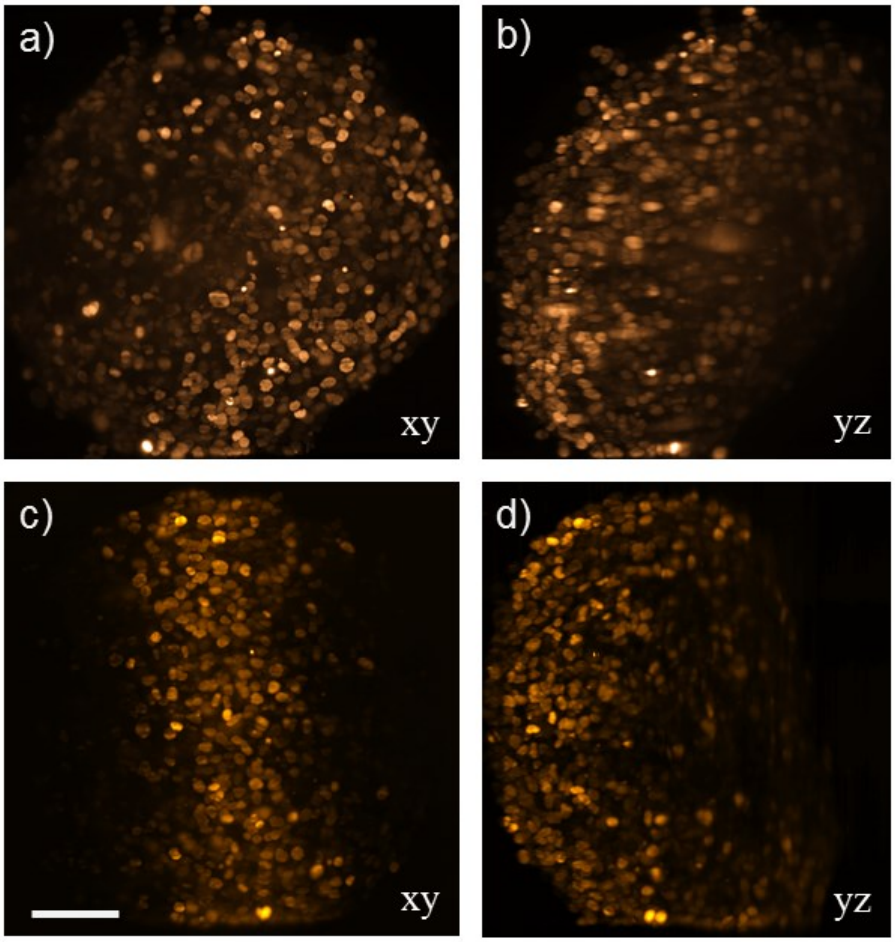

Figure 5.11: 3D imaging of MCTS expressing H2B-mCherry with Gaussian modalities.
Images are maximum intensity projections obtained on the given planes from *z* stacks taken with (a-b) DSLM-Gauss, and, (c-d) 2p-DSLM-Gauss. All *z*-stacks are composed of 50 images taken in steps of 2 µm. Scale bars: 100 µm.

Figure 5.11 shows the images obtained from H2B-MCherry MCTS with the Gaussian modalities. Although, both of them offer permit a clear observation of the relevant features of the chromatin structures(Figure 5.11(a,c)), it is apparent that the z-sections are of better quality and appeared more contrasted in the 2p case (compare Figure 5.11 (b) and (c)).

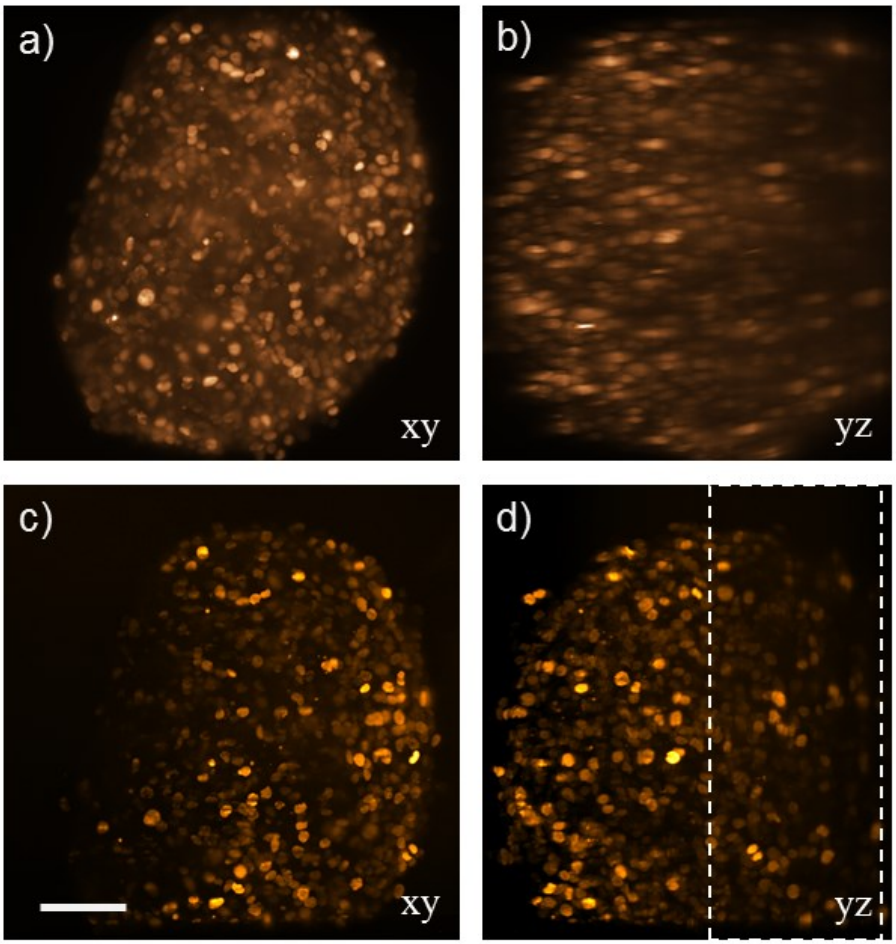

Figure 5.12: 3D imaging of MCTS expressing H2B-mCherry with Bessel modalities.
Images are maximum intensity projections obtained on the given planes from *z* stacks taken with (a-b) DSLM-Bessel, and, (c-d) 2p-DSLM-Bessel. All *z*-stacks are composed of 200 images taken in steps of 2 μm. Scale bars: 100 μm.

Figure 5.12 shows the images obtained from H2B-MCherry MCTS with the Bessel modalities. Here it is evident that 1p-DSLM-Bessel introduces an important amount on background noise in the images, as can be observed in the xy projection Figure 5.12(a). Besides, the axial resolution and the optical sectioning worsen as is evident in the yz projection image that appears smeared along the z axis, see Figure 5.12(b). On the other hand, 2p-DSLM-Bessel images, Figure 5.12(c-d), are remarkably clear and well contrasted as compared with the rest of the modalities, particularly in the axial zone corresponding to the deeper structures that are located farther from the collection objective (dotted square Figure 5.12 (d)).

Table 5.5: Summary of the experimental parameters employed to collect the data supporting Figure 5.11 and Figure 5.12.

Modality	Parameters			
	Wavelength (nm)	Avg. power (mW)	Int. time (ms)	*z* step (μm)
DSLM-Gauss	532	<1	200	2
DSLM-Bessel	532	<1	500	2
2p-DLSM-Gauss	1044	300	1000	2
2p-DLSM-Bessel	1044	450	2000	2

5.6 Discussion and concluding remarks

We have built a very versatile DSLM system that allows changing between different modalities without affecting significantly the light-sheet's properties (position and tilt). Thanks to this, a fair comparison between the different modalities can be done up to the level of a single optical section.

To start off with our comparative analysis, we can see, from Figure 5.4 and Figure 5.11, that 2p-DSLM offers a slightly better image quality than DSLM in terms of a higher contrast and a reduced background noise. However, the reduced FOV observed in Figure 5.4 can become a limiting factor in applications requiring visualizations of large samples. To ameliorate this, we have presented an alternative configuration that enables larger FOVs, still using Gaussian beams, at the cost of increasing the power requirements of the employed femtosecond-laser. Besides, this configuration presented an outstanding penetration depth as shown in Figure 5.9(c) and Figure 5.10(a,b), and moderately good axial resolution, as it can be seen Table 5.4. Other alternatives such as bidirectional illumination can be used [11]. This could effectively double the usable FOV in 2p-DLSM [13]. Furthermore, thanks to the localized nature of two photon excitation it would allow for the superposition of the two counter-propagating excitation beams with minimal mutually induced background. Nevertheless, for highly refracting samples, or even for asymmetric preparations, the light path coming from the opposite sides can be severely degraded and tilted. This would lead to a poor overlap of the beams, affecting the axial resolution and the contrast. 2p-DSLM-Bessel would play an important role in preserving image quality, i.e., when resolution and contrast are the priority. This

would also give an imaging system with enhanced penetration depths as well as with high axial resolution across the FOV. This indicates that BBs are good alternative if a nonlinear technique is to be used and large FOV is required. Also, it is interesting to note that the FOV can be increased in size up to 4x when compared with the use of Gaussian beams, without compromising the axial resolution (see also Table 5.1). Figure 5.6(e) shows this fact clearly: the image quality is equivalent to the 2p-DSLM image using Gaussian beams (Figure 5.6(c)) but more pharynxes are now evident in the extended FOV. When the FOV is kept constant, then BBs excel the rest of the modalities in terms of axial resolution, see Table 5.4. These results can be understood in the context of the non-diffractive character of BBs illustrated in Figure 5.10(d) and the localized nature of two-photon excitation that add together to produce an outstanding performance.

This is not the same for the linear case (DSLM-Bessel), as the image resolution is degraded due to the side lobes that generate fluorescence that broadens the axial PSF up to the level of the depth-of-field of the collection objective (see Table 5.1 and Table 5.4). As a consequence, its imaging capabilities are severely degraded in terms of contrast and background reduction as can be seen in Figure 5.6(d), Figure 5.7(e), Figure 5.9(b) and Figure 5.12(a,b). This calls for the use of more advanced detection methods such as line confocal approaches that enable the filtering of the undesired fluorescence and help to recover the contrast of the images acquired [30]. However, if for a given application resolution is not important, the use of DSLM-Bessel would give larger FOV and will produce, in a very efficient way (i.e. with small excitation powers producing high fluorescent signals), very homogenous images.

In terms of fluorescence yield, the modalities using linear excitation seem to be much more efficient, as can be appreciated in Table 5.2, Table 5.3 and Table 5.5. The excitation powers needed to obtain the same fluorescence signal are less than 1mW in the linear cases, compared to tens or hundreds of mW for the nonlinear cases. In particular, the DSLM-Gauss modality shows a good trade-off between fluorescence generation, resolution and FOV coverage. This could be very useful for imaging applications of samples that do not tolerate large excitation powers or when dealing with faint or moderate fluorescing samples.

Finally, regarding the laser power levels employed for our experiments as reported in Table 5.2 and Table 5.3, it is important to stress that for the maximum power level employed, which corresponds to 2p-DSLM-Bessel modality, the peak intensity at the sample plane was about 100 GW/ cm^2. This is below the 200 GW/cm^2 threshold for avoiding phototoxicity in long term imaging experiments [31]. In fact for the *in vivo* experiments reported here, all the worms recovered approximately 30 minutes after being anesthetized, and all of them showed again good activity on the agar bench. On the other hand, average power employed for 2p modalities in the experiments with MCTS are closer to the upper limit set by the recommended threshold. This fact has to be taken in consideration if 2p modalities want to be employed for living MCTS. For these experiments, the restriction of the FOV to the region of interest could help to decrease the average power, as the case of the first experiment reported in this chapter. Finally, the use of femtosecond lasers with shorter pulses [32] that can increase the 2p excitation efficiency at moderate average powers would be advisable for power sensitive samples and experiments

5.7 Summary

We have demonstrated two configurations of a multimodal DSLM that can be employed effectively for a variety of samples and experiments, going from living, thin and transparent nematodes to thick highly scattering tumor spheroids. Switching between linear and non-linear, or between Gaussian and BB can be done in a practical and reliable way. This has enabled us to perform a complete characterization and comparison of the performance for imaging of the different modalities. For practical purposes having available several DSLM modalities allows us to adapt the system to the particular requirements of each experiment. In fact, DSLM with Gaussian beams can be used when dealing with dim fluorescence samples and where there is more value in gathering many photons than having superior performance in terms of optical sectioning and contrast. 2p-DSLM with Gaussian beams will be appropriate to image localized structures inside highly scattering samples with high resolution and high fluorescence yield. The use of BB together with DSLM, although giving a large and homogeneous field of view, it can impose some restrictions in the axial resolution and the overall contrast of the images due to the fluorescence excited by the side lobes. This indicates that, to effectively

use it for real microscopy applications, a light rejection strategy, such as line confocal detection, has to be implemented. Finally, the use of BB combined with 2p-DSLM results in a system with and improved image contrast, providing an ideal technique for deep, high resolution imaging over moderately large FOVs, but employing two orders of magnitude higher average powers which may not be advisable for light-sensitive or non-perturbing experiments.

5.8 References

1. W. J. Alford, R. D. VanderNeut, y V. J. Zaleckas, "Laser scanning microscopy," Proc. IEEE **70**, 641- 651 (1982).

2. K. König, "Cell Damage During Multi-Photon Microscopy," en *Handbook Of Biological Confocal Microscopy*, J. B. Pawley, ed. (Springer US, 2006), pp. 680-689.

3. J. Huisken, J. Swoger, F. Del Bene, J. Wittbrodt, y E. H. K. Stelzer, "Optical Sectioning Deep Inside Live Embryos by Selective Plane Illumination Microscopy," Science **305**, 1007 -1009 (2004).

4. E. G. Reynaud, U. Kržič, K. Greger, y E. H. K. Stelzer, "Light sheet-based fluorescence microscopy: More dimensions, more photons, and less photodamage," HFSP J. **2**, 266-275 (2008).

5. J. Huisken y D. Y. R. Stainier, "Selective plane illumination microscopy techniques in developmental biology," Development **136**, 1963 -1975 (2009).

6. J. Palero, S. I. C. O. Santos, D. Artigas, y P. Loza-Alvarez, "A simple scanless two-photon fluorescence microscope using selective plane illumination," Opt. Express **18**, 8491-8498 (2010).

7. W. R. Zipfel, R. M. Williams, y W. W. Webb, "Nonlinear magic: multiphoton microscopy in the biosciences," Nat Biotech **21**, 1369-1377 (2003).

8. P. J. Keller, A. D. Schmidt, J. Wittbrodt, y E. H. K. Stelzer, "Reconstruction of Zebrafish Early Embryonic Development by Scanned Light Sheet Microscopy," Science **322**, 1065 -1069 (2008).

9. P. J. Keller y E. H. K. Stelzer, "Quantitative in vivo imaging of entire embryos with Digital Scanned Laser Light Sheet Fluorescence Microscopy," Curr. Opin. Neurobiol. **18**, 624-632 (2008).

10. P. J. Keller, A. D. Schmidt, A. Santella, K. Khairy, Z. Bao, J. Wittbrodt, y E. H. K. Stelzer, "Fast, high-contrast imaging of animal development with scanned light sheet-based structured-illumination microscopy," Nat Meth **7**, 637-642 (2010).

11. J. Huisken y D. Y. R. Stainier, "Even fluorescence excitation by multidirectional selective plane illumination microscopy (mSPIM)," Opt. Lett. **32**, 2608-2610 (2007).

12. J. Swoger, P. Verveer, K. Greger, J. Huisken, y E. H. K. Stelzer, "Multi-view image fusion improves resolution in three-dimensional microscopy," Opt. Express **15**, 8029-8042 (2007).

13. T. V. Truong, W. Supatto, D. S. Koos, J. M. Choi, y S. E. Fraser, "Deep and fast live imaging with two-photon scanned light-sheet microscopy," Nat Meth **8**, 757-760 (2011).

14. F. O. Fahrbach, P. Simon, y A. Rohrbach, "Microscopy with self-reconstructing beams," Nat Photon **4**, 780-785 (2010).

15. T. A. Planchon, L. Gao, D. E. Milkie, M. W. Davidson, J. A. Galbraith, C. G. Galbraith, y E. Betzig, "Rapid three-dimensional isotropic imaging of living cells using Bessel beam plane illumination," Nat Meth **8**, 417-423 (2011).

16. K. Greger, J. Swoger, y E. H. K. Stelzer, "Basic building units and properties of a fluorescence single plane illumination microscope," Rev. Sci. Instrum. **78**, 023705 (2007).

17. S. Akturk, B. Zhou, B. Pasquiou, M. Franco, y A. Mysyrowicz, "Intensity distribution around the focal regions of real axicons," Opt. Commun. **281**, 4240-4244 (2008).

18. O. Brzobohatý, T. Čižmár, y P. Zemánek, "High quality quasi-Bessel beam generated by round-tip axicon," Opt. Express **16**, 12688-12700 (2008).

19. R. Kerr, V. Lev-Ram, G. Baird, P. Vincent, R. Y. Tsien, y W. R. Schafer, "Optical Imaging of Calcium Transients in Neurons and Pharyngeal Muscle of C. elegans," Neuron **26**, 583-594 (2000).

20. C. J. Engelbrecht y E. H. Stelzer, "Resolution enhancement in a light-sheet-based microscope (SPIM)," Opt. Lett. **31**, 1477-1479 (2006).

21. J. Swoger, M. Muzzopappa, H. López-Schier, y J. Sharpe, "4D retrospective lineage tracing using SPIM for zebrafish organogenesis studies," J. Biophotonics **4**, 122-134 (2011).

22. R.-Z. Lin, R.-Z. Lin, y H.-Y. Chang, "Recent advances in three-dimensional multicellular spheroid culture for biomedical research," Biotechnol. J. **3**, 1172-1184 (2008).

23. E. Fennema, N. Rivron, J. Rouwkema, C. van Blitterswijk, y J. de Boer, "Spheroid culture as a tool for creating 3D complex tissues," Trends Biotechnol. **31**, 108-115 (2013).

24. Y.-C. Tung, A. Y. Hsiao, S. G. Allen, Y. Torisawa, M. Ho, y S. Takayama, "High-throughput 3D spheroid culture and drug testing using a 384 hanging drop array," Analyst **136**, 473-478 (2011).

25. C. Lorenzo, C. Frongia, R. Jorand, J. Fehrenbach, P. Weiss, A. Maandhui, G. Gay, B. Ducommun, y V. Lobjois, "Live cell division dynamics monitoring in 3D large spheroid tumor models using light sheet microscopy," Cell Div. **6**, 22 (2011).

26. F. Pampaloni, N. Ansari, y E. H. K. Stelzer, "High-resolution deep imaging of live cellular spheroids with light-sheet-based fluorescence microscopy," Cell Tissue Res. **352**, 161-177 (2013).

27. R. Jorand, G. Le Corre, J. Andilla, A. Maandhui, C. Frongia, V. Lobjois, B. Ducommun, y C. Lorenzo, "Deep and Clear Optical Imaging of Thick Inhomogeneous Samples," PLoS ONE **7**, e35795 (2012).

28. C. Bourgenot, C. D. Saunter, J. M. Taylor, J. M. Girkin, y G. D. Love, "3D adaptive optics in a light sheet microscope," Opt. Express **20**, 13252 (2012).

29. D. Turaga y T. E. Holy, "Aberrations and their correction in light-sheet microscopy: a low-dimensional parametrization," Biomed. Opt. Express **4**, 1654-1661 (2013).

30. F. O. Fahrbach y A. Rohrbach, "Propagation stability of self-reconstructing Bessel beams enables contrast-enhanced imaging in thick media," Nat Commun **3**, 632 (2012).

31. K. König, P. T. C. So, W. W. Mantulin, y E. Gratton, "Cellular response to near-infrared femtosecond laser pulses in two-photon microscopes," Opt. Lett. **22**, 135-136 (1997).

32. P. Xi, Y. Andegeko, L. R. Weisel, V. V. Lozovoy, y M. Dantus, "Greater signal, increased depth, and less photobleaching in two-photon microscopy with 10 fs pulses," Opt. Commun. **281**, 1841-1849 (2008).

Chapter 6: Fast 3D light-sheet imaging

6.1 Abstract

In light-sheet microscopy techniques the specimen under investigation is illuminated with a thin sheet of laser light and the fluorescence emitted from this thin volume is recorded orthogonally with an array detector. The sample is then scanned orthogonally to the light sheet to obtain optical sections of the object at different depths. The optical sections are digitally combined then to obtain a high resolution 3D representation of the object.

The medium to high numerical aperture lenses needed to produce high resolution images in the detection arm determine the effective depth-of-field (DoF) of the imaging system to a few microns. The light sheet is restricted then to be within the DoF of the collection lens in order to produce in-focus images, the light sheet is usually placed in the middle of the DoF. As the light sheet is static, the object is scanned across the light sheet to obtain the optical sections. In light-sheet microscopy samples attached to a supporting structure (glass/plastic capillaries, agarose cylinders, metallic hooks) are usually placed within an immersion chamber that preserves certain properties of the sample (hydration, osmotic pressure, optical clearing). Mechanical movement of the sample imposes limitations on the maximum scan speed achievable with such systems, limited by the time of relaxation of the sample and the maximum step response of the device. Fluxes within the chamber can be also driven by the movement of the sample and the supporting structure attached to it introducing mechanical as well as optical disturbances in to the system. These limitations call for an alternative way to scan the sample within a light sheet microscope that would allow for faster scan rates and less movement related artifacts.

Here we present a new light sheet-based imaging system that contains a wavefront encoding system that extends the DoF in the collection path. This allows capturing 3D stacks of wavefront encoded images without any movement of the sample or imaging objective. This system allows, by moving the light sheet, fast 3D imaging at speeds only limited by the maximum frame rate available in the detector. To obtain the final 3D decoded image, a deconvolution algorithm is used.

6.2 Introduction

6.2.1 Fast 3D Microscopy

Faster imaging speeds, with increased sensitivity acquisition and higher resolutions are the demands of current fluorescence microscopy for biological applications. For instance, 3D volumetric images acquired in a few milliseconds are required to follow intrinsic biological phenomena [1]. Calcium waves of heart and brain cellular cultures, the embryonic zebrafish beating heart and the red blood cells in the developing cardio-vascular are a few of the most challenging biological processes calling for faster optical microscopy. Spinning-disk microscopy [2] or confocal laser scanning using resonant scanners [3] are the commercial fastest devices that have pushed the technological limits reaching up to 30 frames per second with reasonable signal [4]. In these techniques the signal-to-noise ratio is compromised at higher speeds due to the intrinsic limitation of the photon budget. Under such conditions the amount of generated photons per voxel per second becomes importantly reduced. This might be overcome by an increased excitation power. However, this also may cause unwanted photobleaching followed by photodamage on the sample. This limitation is importantly reduced when using Light Sheet Fluorescence Microscopy (LSFM) as it efficiently achieves optical sectioning by only illuminating the imaged plane in the sample [5]. This technique allows higher illumination intensities with minimum photobleaching/photodamage and naturally sets the acquisition speed limit to the acquisition time of the camera [6] without giving up photon excitation/collection efficiency.

LSFM is a dynamic field that is constantly advancing. In the past few years important contributions have led to enhanced spatial [7] [8] [9] and temporal [6] [10] resolution as well as breakthroughs in the conceptual design and complexity of live imaging experiments [11] [12] [13] [14]. A particularly interesting implementation of LSFM relies in sequential multiview imaging, in which the sample is rotated and image stacks are sequentially acquired from multiple view angles [7]. Recently, at least two implementations of simultaneous multiview light-sheet microscopy, where two light sheets and two collection paths are employed to capture 4 simultaneous views of the sample, were proposed [12] [13]. In these approaches 2 cameras, placed each side of the sample were used to capture two

sequences of two high resolution images that cover the entire sample volume in four views while the sample is scanned only once. With these approaches authors claim improving the imaging speed more than 20-fold over sequential multiview light-sheet microscopy, reaching a rate of 0.3-0.2 volumes per second to follow *in toto* Drosophila embryo development. Recently, an optimized version of this multiview approach has been reported to record the neuronal activity of Zebra fish embryos [14]. Genetically encoded calcium indicator from the entire volume of the brain of the larval zebrafish was recorded *in vivo* at 0.8 Hz.

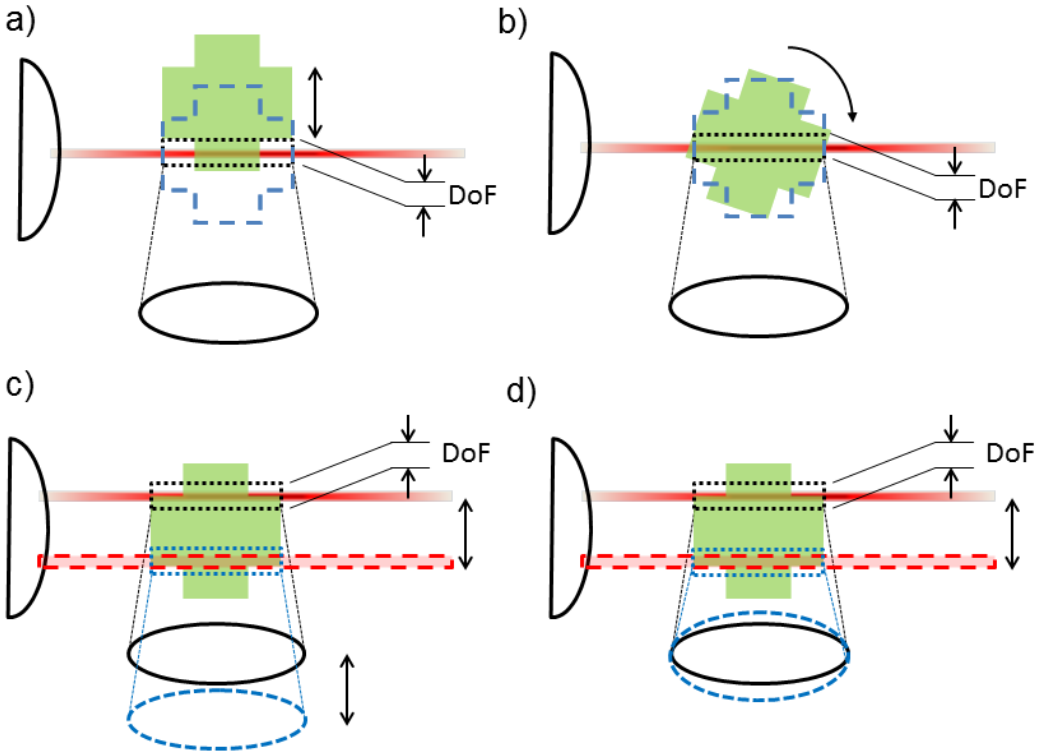

Figure 6.1: Scheme of the different scanning paradigms in LSFM.
Figures a) and b) illustrate the scanning methods of the most standard LSFM implementations. Sample is a) axially scanned, and/or, b) rotated to obtain the optical sections required for a tomographic reconstruction. Figures c) and d) show other LSFM variants where the sample is kept static. In c) the collection objective is moving synchronized to the light sheet to capture the axial optical sections, whereas in d) the focal distance of the collection arm is changed synchronized to the light sheet to capture the optical sections. Note that in all the four configurations the primary requirement is to keep the light-sheet within the DoF of the collection lens for each step of the scanning.

All these conventional implementations of LSFM are promising alternatives for fast 3D imaging but they have an intrinsic limitation. As the sample has to be mechanically scanned to obtain the volumetric data the capture speed may be limited by: i) mechanical perturbations in the environment, that increases the stabilization

time preceding the capture, and, ii) high frequency oscillations on the biological the sample, that may cause negative side effects on living samples [15]. Schemes of mechanically sample scanned are illustrated in Figure 6.1(a-b).

Alternative implementations based on the synchronized movement of the light sheet and the collection objective, keeping the sample static, have been proposed (see scheme on Figure 6.1(c)). Objective-Coupled Planar Illumination Microscopy where the light sheet is produced with an optical fiber coupled mechanically to the detection objective was implemented to measure calcium transients on sensory neurons of mouse vomeronasal organ [6]. The movement of both light sheet and collection objective is realized through a piezo-controlled stage obtaining volumetric images as fast as 20 planes per second or 2 volumes per second. A similar configuration, termed as *i*SPIM, uses a modified inverted microscope with an additional mechanical housing for two objectives, one for light sheet illumination and the other one for fluorescence collection [10]. By rapidly translating the light sheet synchronized with the collection objective (driven by a piezo stage) through the sample, the module enables rapid volumetric image collection without requiring specimen movement. They reported volumetric captures as fast as 0.5-0.3 volumes per second at the maximum speed of 20 frames per second (integration time of 50ms).

These alternative implementations effectively help to reach higher capture rates. Nevertheless, there are some remaining limitations: i) it is prone to motion artifacts by the movement of the objective, ii) it requires the sample to be covered between two cover glasses which prevent rotating the sample to perform multiview imaging, and iii) the objectives for producing and collecting the light sheet fluorescence have to be implemented in a 45 degree configuration that fixes the attack angle of the light sheet to a very limited range, reducing even more the flexibility typical of conventional SPIM configurations.

Recently, a cleverer alternative to avoid moving parts around the sample was proposed. By actively modifying the focal distance of the collecting objective (using deformable liquid lenses), and moving the light sheet in a synchronised way, imaging speed up to ~30 volumes per second (510 fps) have been reported [16]. Please refer to Figure 6.1(d) for an scheme of this configuration. However, modulation of the at

those high speeds can only be achieved using sinusoidal scanning patterns. This is due to the nonlinear response of the liquid lenses at such high frequencies that reduce the usable axial scanning range of the system and increase the complexity of the synchronization scheme.

There are other novel alternatives, not based on LSFM, that are capable of fast 3D imaging, such as multifocus microscopy. There, an entire 3D focal stack is recorded in a single exposure of the camera, by multiplexing different axial object planes to different positions in the same image plane. Recently, a multifocus microscope having a diffractive grating (MFG) that generates nine simultaneous axially spaced images has been reported [17]. In this case, the MFG splits the fluorescence light emitted from the sample into separate paths, forming an array of 3x3 images on a CCD camera. Using this technique, volumetric images of *C. elegans* embryos were recorded at 9 volumes per second. Although this is an interesting technique that provides an alternative for 3D imaging, it possesses some limitations: i) poor of optical sectioning (equivalent to the one of a widefield microscope), ii) poor optical efficiency of the gratings employed (67%) (that would affect the final SNR) and, iii) reduction of the FOV as the entire 3D image stack should fit in one single frame.

Therefore, a method capable of fast, unperturbed and full optical sectioning imaging would be a breakthrough in the field 4D imaging at high speeds.

In this work we present a LSFM in which only the light sheet is scanned through the sample and any other element remains static. To be able to image the whole sample during the scanning, the depth of field (DOF) of the collecting objective is passively extended by the use of a wavefront coding mask. By doing so, the generated 2D fluorescence image for every position of the scanning light sheet is efficiently collected and recorded by the camera. This results in a stack of 2D images that is used to reconstruct the final 3D image. Furthermore, as only the light sheet is moved, fast 3D imaging can be achieved without any synchronization between the camera and the light sheet. Since typical light scanning devices can run at KHz rates, 3D acquisition speeds are only limited by the reading speed of the camera. This is a completely new paradigm of volumetric scanning in LSFM that allows non-disturbing, fast 3D imaging.

6.2.2 Extended depth of field imaging

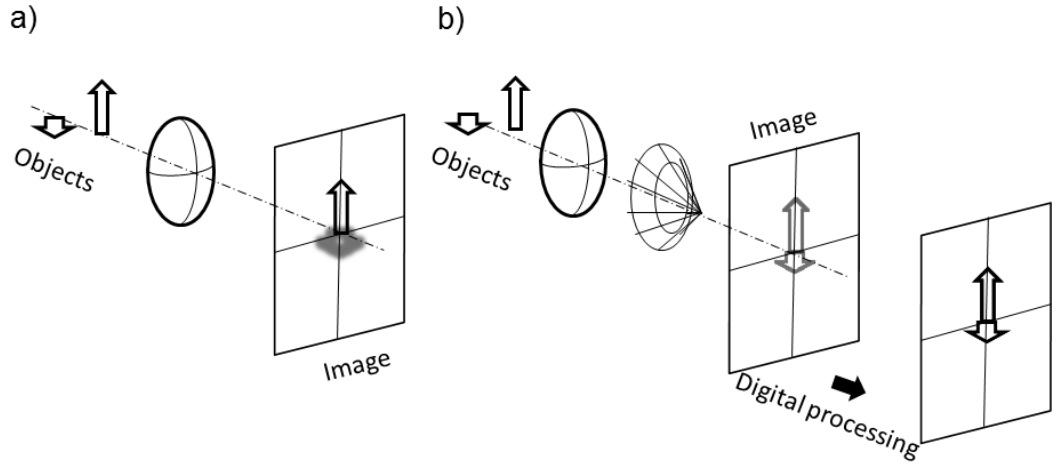

Figure 6.2: Principles of extended DoF imaging.
In a) conventional optical systems objects located at different axial positions cannot be focused at the same image plane, whereas in b) EDoF systems objects can be focused at the same plane using an optical-digital approach.

There are several ways to extend the depth of field of an optical system. The depth of field (DoF) of a microscopic imaging system is given by:

$$\mathrm{DoF} = \frac{\lambda_{em} n}{\mathrm{NA}^2} + \frac{n\ e}{\mathrm{M}\ \mathrm{NA}}$$

Where λ is the excitation wavelength, n is the refractive index of the medium between the sample and the objective lens , and NA is the objective numerical aperture. The variable e is the smallest distance that can be resolved by a detector that is placed in the image plane of the microscope objective, whose lateral magnification is M. In regular microscopy systems, the second term of the equation can be neglected as $\mathrm{M} >> e$. Then the easier way to increase the DoF is by reducing the NA. However, lateral resolution of the system would be reduced as it is directly proportional to NA. An additional side effect of reducing the NA is a drastic decrease of the light throughput of the optical system that scales inversely as the square of NA. Thus an ideal extended DoF optical system should be optimized to maximize the light gathering power, to achieve the maximum lateral resolution, and yet have a large DoF [18]. A number of methods have been proposed to work around these limitations and to produce an extended DoF microscope. Potuluri et al. [19] have demonstrated the use of rotational shear interferometry with a conventional widefield

transmission microscope obtaining a system with infinite DoF. However, this comes at the expenses of a change in magnification with depth and the rapid drop in image contrast away from the imaging lens focal plane, besides being complex and severely reducing signal–to–noise ratio (SNR). Another approach is based in the so called *wavefront coding* (WFC) technique [20]. Here, the pupil of the lens is modified in such a way that the information along the axial direction is encoded into the pupil's optical wavefront. The resulting image at the detector plane contains information of an extended range of axial positions as compared with a regular lens with the same NA. A further digital restoration step is required to fully recover the features of the imaged 3D objects [21]. A scheme of these extended DoF systems is shown in Figure 6.2. This digital-optical system capable of extended DoF imaging does not have an optical-only equivalent. In general, WFC techniques use pupil masks that are some complex function of amplitude and phase. This function can be smoothly varying and therefore usable over a range of wavelengths, or it can have discontinuities in step sizes that depend on the wavelength, such as a binary phase mask [22]. Other approaches rely on the use of amplitude pupil masks [23]. These can be effective at increasing the depth of field, but they do tend to reduce the light throughput of the pupil. This poses a major problem for low light fluorescence microscopy. Hybrid approaches have also being designed by combining an annulus with a binary phase mask [24]. This allows a large boost in light throughput while giving, at the same time, a ten times increase in depth of field. However, these masks are wavelength dependent imposing serious restrictions for their use in microscopy.

The cubic phase mask (CPM) was one of the first generation wavefront encoding systems, designed for general extended DoF imaging [20] [25]. These masks can give a ten times increase in the DoF without loss of transverse resolution. Converting a standard widefield microscope to a wavefront coding system is, in principle, straightforward. The phase mask is placed in the back pupil of the microscope objective. Once a phase mask is chosen to match a lens and application, an appropriate digital inverse filter can be designed by measuring the PSF. The digital restoration can be a simple single-step Weiner deconvolution [26]. Other iterative deconvolution approaches can be employed to increase the fidelity of the restored images [27]. In this case the processing time increases proportionally to the number

of iterations required for the convergence of the employed algorithms [28]. The main trade off of such systems is between the DoF achieved and the resulting sensitivity to the noise for a given mask [20]. The cubic PM also introduces some slight lateral shift when imaging the specimen features away from best focus position [29]. This is in addition to a perspective projection due to the imaging geometry, since an extended DoF image is obtained from a lens at a single position on the optical axis. High numerical aperture imaging can be also benefited from WFC approaches and has the potential to produce high lateral resolution, but it requires more complex theory to be modelled accurately [18] [30].

Axicons are conical lenses that can be also used to achieve EDoF of a microscope. The axicon, was first introduced by McLeod in 1954 and it can produce an extended focal segment [31] [32]. Due to this peculiar ability, axicons have been incorporated in numerous applications [33–36]. In the DSLM variant of LSFM axicons have been used to create a Bessel beam that is scanned in one direction to increase the FOV of the excitation light sheet [37–39] as was explained in last chapter. Interestingly, axicons can behave as image forming elements that can be combined with spherical lenses to design imaging systems with EDoF [34,40]. As it is customary in wavefront coding methods, the images obtained with these systems exhibited overall reduced contrast, and digital deconvolution processing has to be performed.

Finally, and importantly, in standard implementations of wavefront coding technologies, the extension of the depth of field is strictly related to the invariance of the effective PSF of the collection system over a determined range of defocus values. This means that these systems tend to maximize the extension of the axial PSF of the imaging lens. This is incompatible with the concept of optical sectioning and results in a system incapable of depth discrimination.

6.3 Description of the method: combining LSFM and WFC techniques

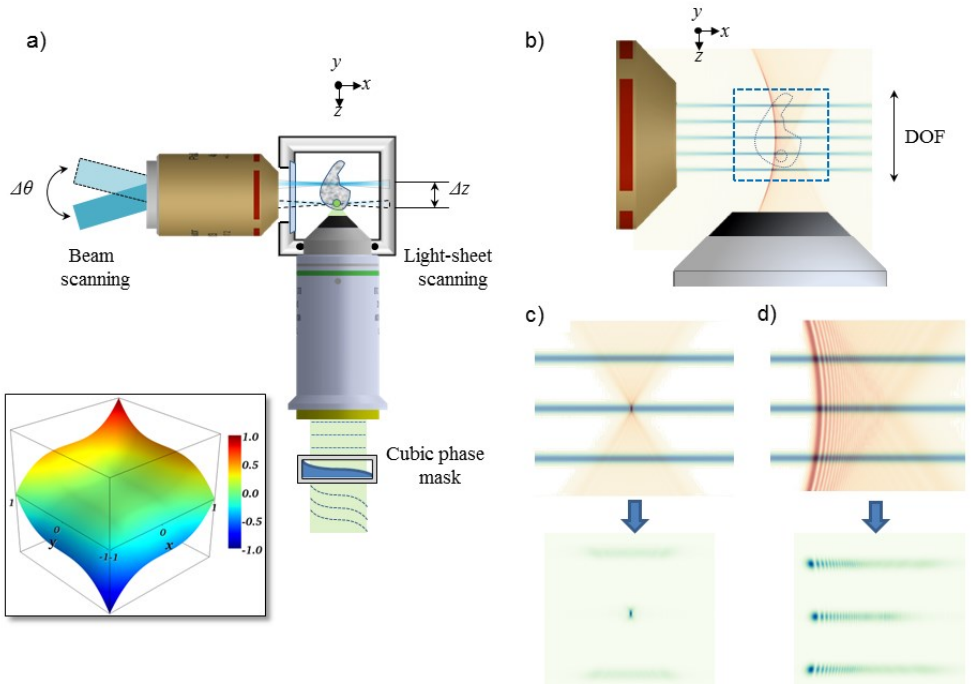

Figure 6.3: Description of the WFC-LSFM approach.

Figures describe the principles of the implementation of WFC on a light-sheet microscope. Figure a) is the scheme of the proposed optical setup. Inset shows the shape of a generic cubic phase mask of unitary amplitude that is inserted at the back aperture of the collection objective. Figure b) illustrates the new light-sheet scanning paradigm that results from the extended DoF given by the cubic phase mask. Figures c) and d) explain the PSF formation mechanisms in a standard LSFM and in the proposed WFC-LSFM, respectively. Upper images show the shape of the light-sheets at different positions during an axial scanning (blue) and the PSF of the collection system (red). Lower images show the effective PSFs of the system for the same configuration.

Extending the DOF of an imaging system can be done, in a passive way, by the use of WFC techniques. These work by modifying the Optical Transfer Function (OTF) of the imaging system, while minimally impacting on its resolution and optical throughput. This is normally done by simply placing a cubic phase mask at the exit pupil of an objective lens. In the particular case of LSFM, the WFC mask should be inserted just at the back aperture of the collection objective, see Figure 6.3 (a). By doing this, the light-sheet is now free to move axially within a range Δz determined by the amount of DoF created by the cubic mask. The light sheet can be scanned at the sample plane by changing the tilt of the incident excitation beam al the back aperture of the excitation objective. This is done by using a galvometric mirror

conjugated to the exit pupil of the objective. Figure 6.3(b) show different positions of the light-sheet within the DoF to illustrate how an axial scan can be performed to retrieve the optical sections of the biological sample. This light-sheet axial scanning cannot be performed in a regular LSFM microscope as the effective imaging point-spread function (PSF), that results from the multiplication of the excitation light-sheet and the PSF of the collection objective, degrades rapidly as the light-sheet diverges form the *in focus* position just at the center of the DoF, see Figure 6.3(c). In contrast, when the same argument is applied to a WFC powered LSFM microscope, it can be seen form Figure 6.3(d) that the effective PSF remains practically invariant for the same light-sheet axial displacement, Figure 6.3 (d).

6.4 Practical implementation of a WFC-LSFM

To practically implement a WFC-LSFM system, we use a deformable mirror (DM) lying in a conjugated plane with the exit pupil of the objective lens (see Materials and methods section). The use of the DM allows the generation of different phase masks that can achieve different extensions of the DOF. A Shack-Hartmann sensor, connected to the DM in a closed-loop approach, is used to ensure proper shaping of the mirror. Note that this set up has the advantage that it can also be used to compensate sample aberrations. The targeted wavefronts on the DM were set to be the traditional cubic phase masks, $\Delta\varphi=k\cdot PV\cdot(u_x^3+u_y^3)$, where u_x and u_y are the normalised spatial coordinates at the pupil, k is the wavenumber and PV is the peak-to-valley amplitude of the wavefront. Three different cubic phase masks having 10, 20, and 30 μm PV were used. For the experiments presented in this chapter our sCMOS camera was set with an active area of 2048 x 512, 2048x256 and 2048x128 pixels^2. Under these conditions, the maximum reading speeds of the sCMOS are 400, 800 and 1600 fps, respectively.

6.4.1 Materials and methods

6.4.1.1 Optical setup

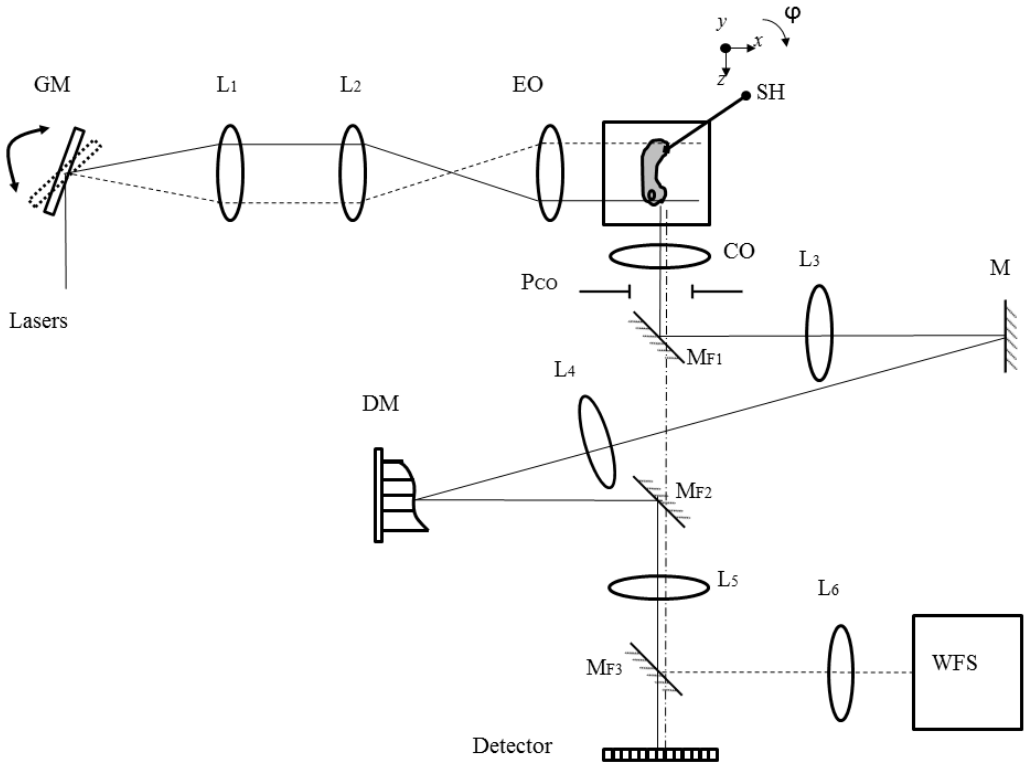

Figure 6.4. Schematic of the optical setup employed.
Detailed description can be found in the text. List of parts according to the nomenclature employed in this figure can be found in Table 6.1.

The basic design of the WFC-LSFM employed in this work is shown in Figure 6.4 and it is based on the LSFM optical setup described in the previous chapter. The complete list of components is shown in Table 6.1.

For the purposes of this work we employed SPIM and one-photon DSLM with Gaussian beams with a power at the sample plane below P=0.3mW. The set-up contains an excitation arm with a lasers (λ=488nm) that is directed to a pair (two axis) galvanometric scanning mirror assembly (GM). In the SPIM mode, a cylindrical lens is placed at a distance equal to its focal length to the galvo mirrors, which remain static. In the DSLM mode, the fast GM is used to scan the beam in the *y* direction generating an *x*-*y* plane (not shown). In both cases, the relay lenses, L1 and L2, and the excitation objective, EO, generate the light sheet on the sample plane. These lenses are also used to adjust the beam size according to the required axial resolution and Field of View (FoV). The slow GM is used to scan the light

sheet in the *z* direction but remains static for conventional SPIM and DSLM. The generated fluorescence is collected with a water dipping infinity-corrected objective (CO), located in the collection arm of the LSFM. In order to image the illuminated plane, the distance between the front lens of the CO and the light sheet is set to be equal to the working distance of the objective.

Table 6.1. List of parts of the WFC-LSFM.

Item	Manufacturer/model	Notes
Laser	Cobolt MLD/ 0488-06-010060-100	488nm , 150mW
Galvo Mirrosr/GM	Thorlabs/GVS002	2 axis.
L1	Thorlabs/LA1027-A	F=35mm
L2	Thorlabs/LA1433-A	F=150mm
Excitation objective/EO	Nikon/Plan Fluor 10x	NA=0.3, WD=16mm
Sample holder/SH	Thorlabs/3-axis NanoMax, Physik instrumentel M-116.2SH	Stepper motors for xyz translation and φ rotation.
Collection objective CO	Leica/HCX apo L20X	NA=0.5
L3	Thorlabs/AC254-200-A	F=200mm
L4	Thorlabs/AC254-250-A	F=250mm
DM-Deformable Mirror	Imagine optic/Mirao52e	
L5	Thorlabs/AC508-250-A	F=250mm
L6	Thorlabs/AC254-060-A	F=60mm
WFS	Imagine optic/Haso 3 32	
Detector	Hamamatsu/ ORCA-Flash 4.0 C11440-22C	
Synchronization/Control	National instruments/PCIe-6353	

An optical system, composed by a couple of steering mirrors, M_{F1} and M, and a couple of relay lenses, L3 and L4, is used to conjugate the exit pupil of the CO (P_{CO}) to the surface of a deformable mirror (DM). The DM (mirao52e, Imagine Optic) generates the wavefront required for extending the depth of field of the CO. To set the shape of mirror, a Shack-Hartmann a wavefront sensor (HASO v3, Imagine Optic), placed at a conjugated plane to the DM (and therefore to the exit pupil to the CO), was employed. For this, a couple of relay lenses, L5 and L6, and two additional

steering mirrors, M_{F2} and M_{F3}, were used. Once the DM produces the target phase, M_{F3} is removed from the optical path. Finally, lens L5 is effectively employed as a tube lens that focuses the captured fluorescent light on the sCMOS detector. Note also that mirrors, M_{F1}, M_{F2} can be moved to enable/disable the wavefront coding optical path, allowing the optical setup to be used as a regular LSFM.

6.4.1.2 Cubic mask generation/Adaptive optics loop

The cubic phase masks employed in this work were generated using the principles of adaptive optics as described in Jorand et al. [41]. This is done in two steps briefly described as follows:

6.4.1.2.1 Pupil conjugation

Basically, the pupil of the objective, P_{co}, the surface of the deformable mirror (DM) and the microlens array of the wavefront sensor (WFS), should be all placed at a conjugated plane to each other. To ensure that, a uniform light sheet generated using a dyed (FITC-dextran) agar sample was imaged using the standard DSLM configuration (mirrors M_{F1}, M_{F2} and M_{F3} are removed). Once this is done, mirrors M_{F1} and M_{F2} are enabled and the shape of the DM is set to the factory pre-callibrated flat configuration and its position is adjusted to be in a conjugated plane with the pupil of the objective. Finally the wavefront sensor (WFS) is enabled (by re-introducing mirror M_{F3}) and its position is adjusted so that the microlens array is at a conjugated with the pupil of the objective.

6.4.1.2.2 Phase mask generation

To produce the required cubic phase masks we designed three wavefronts with peak-to-valley amplitudes: PV=10, 20 and 30 μm. Wavefront measurements were done using, as guiding stars, 1 μm fluorescent beads in agar. A closed-loop approach was employed to set the shape of the DM according to the specified wavefront targets for the different PV amplitude values, including the reference PV=0 were the target is a flat wavefront. Once that the DM have produced the target phase, its shape (pattern of voltages) was recorded for future use. The final mirror shapes were recorded after the closed-loop converges to a solution within 30nm RMS wavefront error. The mirror shapes corresponding to each designed phase mask were then employed for the experiments.

6.4.1.3 Deconvolution, MTF, and particle tracking

Deconvolution was perfomed using an implementation of the Richardson-Lucy algorithm that is included in the plugin "Deconvolution lab" of imageJ [42]. The PSFs for each case were obtained from beads immersed in agar as explained in methods. Single PSFs were cropped, background-corrected, resized and centered before loading them to the deconvolution routine. Deconvolutions were performed plane-by-plane. This allowed decoding only the effects of the wavefront encoding process leaving the z-component of the PSF intact as they only depend on the properties of the illuminating light sheet. The number of iterations was set to 20 as these value showed to be enough to guarantee the convergence of the algorithm for all the experiments performed in this work. Enhanced or more specific deconvolution algorithms can be equally used [27,28,43].

MTFs were calculated as the modulus of the Fourier transform of the PSFs obtained using a sample of fluorescent microspheres [44], for the different conditions mentioned in the text. Fourier transforms were computed using the Fast fouruier Transform library implemented in the Scipy library of Python [45].

Particle tracking was done manually using the ImageJ plugin MTrackJ. Z positions were recalculated using a Gaussian fitting to increase the precision of the localization.

6.4.1.4 Control software – synchronization

A custom made Labview interface was developed to operate and synchronize the acquisition of the microscope images with the GM scanning system. Two acquisition modes were used: i) External controlled mode (synchronous) and ii) free running mode (asynchronous).

In the synchronous mode, the GMs are driven by a triangle and saw-tooth voltage signals for fast (*y axis*) and slow (*z axis*) mirrors, respectively. A step function trigger signal controls the data acquisition of the camera and ensures that every image is taken when the galvos are static. All these voltage signals were generated by a NI USB-6353 data acquisition and generation card device (DAQ) from National Instruments (National Instruments Corp., Austin, TX, USA). The labview program was made in such a way that the frequency of the fast scanning signal is an integer

multiple of the slow scanning signal in order to avoid introducing incomplete frames within the integration time of the camera. The z-scanned signal was generated in steps. For each z position, a trigger signal is fired just after the galvo reaches the programmed value and an image is captured. The exposure time was set to a value slightly lower than the step interval. The maximum frame rate practically achievable with this synchronous configuration is 250Hz as this corresponded to an integration time of just over 1 ms, the minimum allowed by the sCMOS in the actual configuration.

In the free running mode the GM are also driven by a triangle and saw-tooth voltage as before but in this case, there is no triggering signal controlling the acquisition of the camera. In this mode, the camera continuously acquires an image according with the specified frame rate. This allows taking advantage of the maximum integration time of the camera for the modes faster than 100fps.

6.4.2 Sample preparation and mounting

The samples are held by a custom made capillary sample holder (SH) that is attached to a three axis motorized stage (*x, y and z*) and a rotation stage that controls the angle ø. The SH is located into a custom-made immersion chamber that is filled with a physiological fluid (PBS) that keeps the samples in osmotic equilibrium. Chamber is made from a cube of Teflon optically accessible from three glass windows made with coverslips (N= 1.5, 170 μm thickness). The objective lens enters the chamber from a hole machined at one face of the cube, the objective is held with the chamber with an o-ring that prevents any fluid leaking.

Fluorescent microspheres/ FITC-dextran

We employed green fluorescent microspheres of 0.2 and 1 μm (Duke scientific, G200 and G0100, 2% solids) for the experiments reported in this work. To obtain a sample of microspheres sparsely distributed over the imaging volume we prepared a dilution 1:1000 in ultrapure water (type 1, Milli-Q,). Different aliquotas of this stock solution were stored in 1.5 ml conical tubes. The stock solution were vortex for 30 s before preparing the sample for imaging to obtain a disperse distribution. We added 10 μl of the stock solution to 0.1-ml of 1% low-melting agarose (LMA) at 45^{o}C in another 1.5-ml conical tube and vortex gently. Agarose-microbead solution were

drawn directly to a glass capillary (Hirschmann Z611263, 100 µl) with a micropippete. Samples were incubated at 4% for 5 min for stabilization and then mounted into a custom made LSFM sample holder. A custom-made plunger was used to force the agar cylinder out of the capillary in front of the detection objective. For the particle tracking experiments, a sample 0.2 µm microspheres was prepared and loaded, just before the experiment the agar cylinder were forced to get into the glass capillary again leaving some microspheres floating into the PBS. Experiment started off within 20 s after releasing the microspheres.

For the case of FITC-dextran samples, a stock solution of 100mM was prepared dissolving 0.7mg of FITC-Dextran (Sigma, FD70-100MG) in 1ml of ultrapure water and stored in a 1.5-ml conical tube. Just before the experiment, 10µl of the stock solution (vortexed by 10s) were mixed with 1ml of LMA at 45^{o}C. The prepared solution was injected into a capillary and mounted in the same way as explained before for the samples of beads.

C. elegans strains

C. elegans were grown on nematode growth medium agar plates using standard procedures [46]. We employed two transgenic strains for this work, first; the ljIs1[myo2::YC2.1] line showing expression of yellow cameleon2.1 (YC2.1) throughout the pharynx and, second, juIs76[unc25::GFP] line expressing GFP in a subset of D-type moto-neurons. Adult hermaphrodite worms were immobilized into a 5 µl drop of sodium azide (NaN3, 25 mM) for 10 minutes. A few worms were then picked and transferred to a 5 µl drop of PBS. Then, a micropipette tip (0.1 ml) was loaded with 50 µl of LMA (1%, 45^{o}C) keeping the plunger temporarily depressed in order to drawn up the drop containing the worms by a slow releasing of the plunger. Immediately after, the agar-worm solution was drawn directly from the tip into a glass capillary using the micropippeter. This transfer has to be done slowly to keep the worms evenly distributed in the agar cylinder. Samples were incubated at 4% for 5 min for stabilization and then mounted into a custom made LSFM sample holder. A custom-made plunger was used to force the agar cylinder out of the capillary in front of the detection objective.

6.5 Results 1: Proof-of-principle and characterization

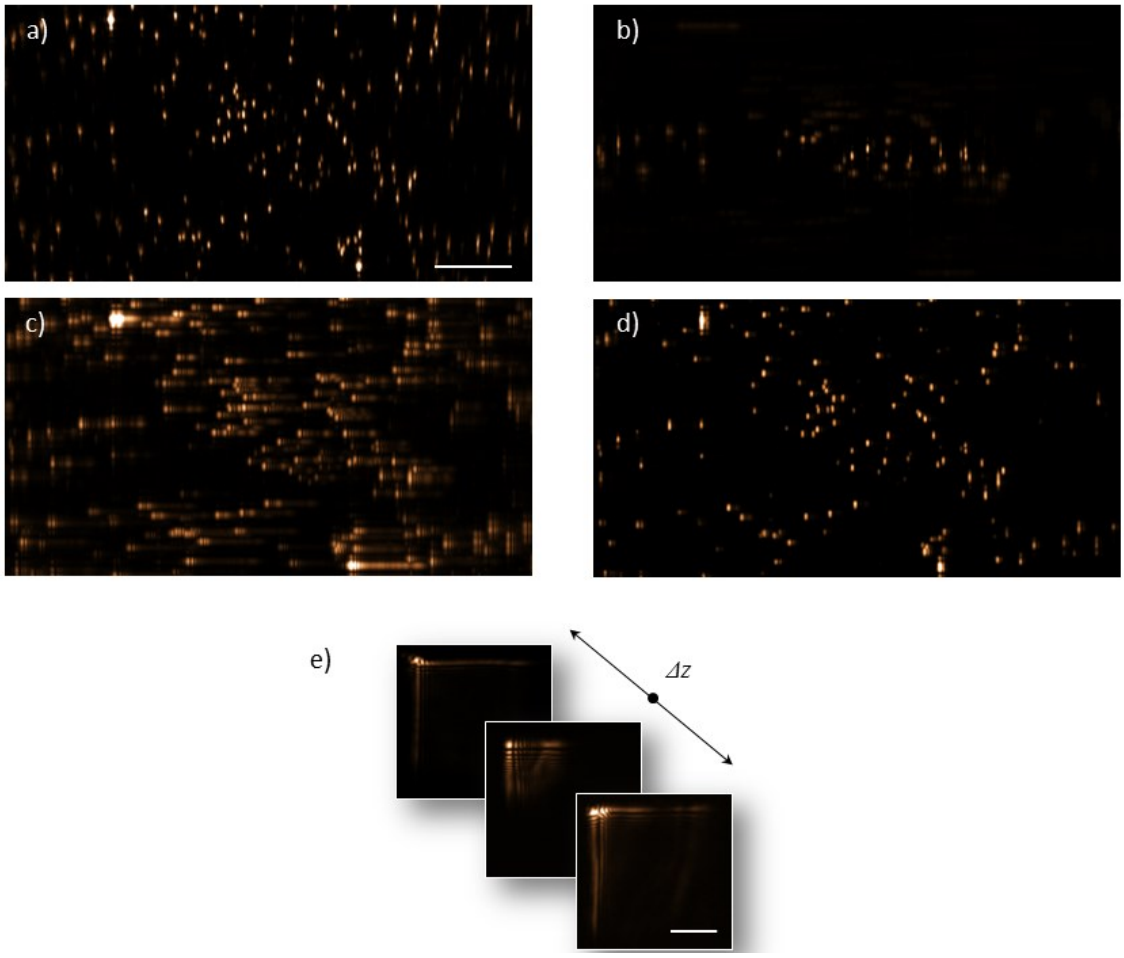

Figure 6.5: Experimental demonstration of WFC-LSFM.
Figures a-d) show xz maximum intensity projections of a stack of images of a sample of 1µm microspheres suspended in agar. First, the DM was set to PV=0µm, standard LSFM mode, and a stack of images were acquired by a) scanning the sample, and, b) scanning the light sheet. Then the DM was set to a cubic phase mask with PV=10µm, WFC-LSFM mode, and a stack of images were acquired by c) scanning the light sheet. Figure d) show the results after deconvolving the stack of images captured in c). Figure e) show the *xy* shape of the PSF and its variation along the DoF. Scalebars: a-d) 50µm, e) 20µm.

We started by comparing standard LSFM and our WFC-LSFM system by imaging fluorescent beads suspended in agar.

We first set, as a reference, the DM to PV=0 µm (flat DM) for standard LSFM. A stack of images of 170 µm in depth was then obtained by moving the sample in the z-direction, Figure 6.5(b). To illustrate the effect of the WFC technique, the sample was slowly (2Hz) scanned with the light sheet. As one can expect with the DM still flat, the resulting image is restricted to the limited objective DOF (Figure 6.5(a)).

However, by setting the DM to a PV=10 µm, the DOF is extended and the whole volume can be imaged, as can be seen in Figure 6.5(c). This figure also shows the need for a deconvolution process, as the image of the beads is deformed due to the modification of the PSF introduced by the cubic mask. The image after deconvolution (Figure 6.5(d)) is similar to that obtained with standard LSFM (Figure 6.5(b)). Notice that the deconvolution have been performed to the entire stack of images and not just to the projection image.

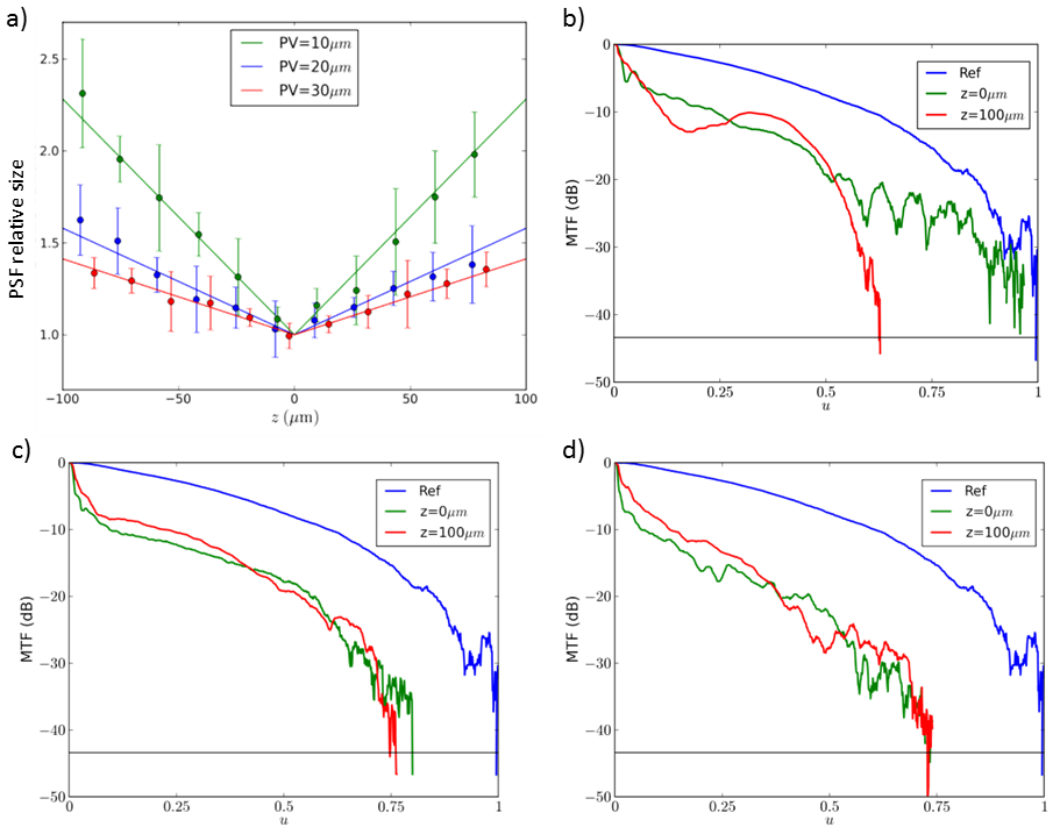

Figure 6.6: PSF size and resolution along the DoF.
Figure a) shows the relative variation of the PSF for the three cubic phase masks employed in this work. The change in the between the resolution along the DoF is assessed by analyzing the MTFs of the three cubic phase mask employed, b) PV=10 µm, c) PV=20 µm, d) PV=30 µm.

Note that, despite that WFC is employed to produce PSF invariance to defocus, the PSF is not perfectly invariant along the z-axis, as shown in Figure 6.5(e). The relative size variation, regarding to the minimum at center of the DoF, for the three cubic masks employed along the DoF explored (170µm) is shown in Figure 6.6(a). This has two important implications. Firstly, the deconvolution cannot be performed using a single PSF for all the planes, and has to be performed using a plane-by-plane

strategy (see methods). While this can be easily done in our system (as the PSF can be measured at each plane), this is not possible in standard WFC. In addition, the lateral shift along the DOF of the PSF can be calibrated and corrected (see methods). These are important advantages of WFC-LSFM in front of standard WFC techniques. Secondly, due to PSF variance, the *x-y* resolution of the system is not constant along the z axis. To assess this change in resolution, the MTF of the system was characterized keeping the same conditions and having the standard LSFM (flat DM) as a reference. For the DM set to PV=10, 20 and 30 μm, the cut off frequency (resolution) dropped by 3%, 20% and 27% at the central plane and by 35%, 25% and 27% at the edge of the imaged volume, see Figure 6.6(b-d). Note that higher values of PV result in a smaller variation in the *x-y* resolution along the z axis. This shows that, for the imaged volume, the PSF can be considered invariant when large PV values are used. Nevertheless, higher PV increase the sensitivity to noise that would detriment the quality of the image after deconvolution.

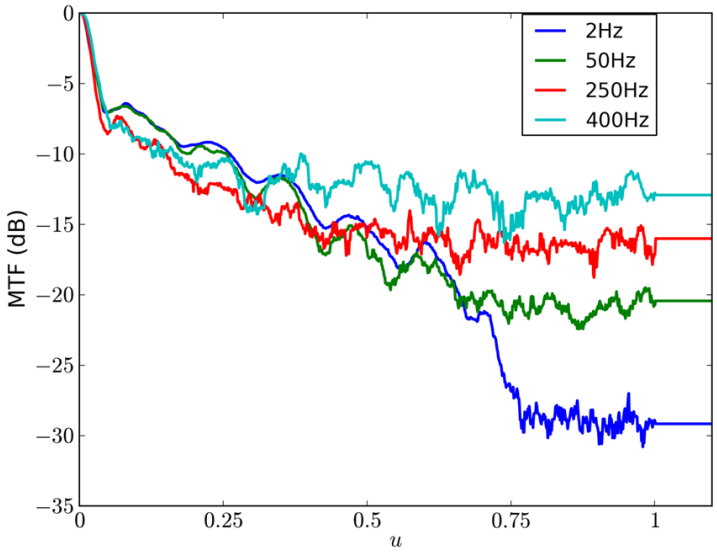

Figure 6.7: WFC-LSFM performance for different scanning rates.
MTFs at the center of the DoF for different scanning rates.

We then proceed to assess the performance of WFC-LSFM at different scanning rates going from 2 fps (integration time, Δτ=440ms) and up to the maximum speed of 400fps (Δτ=2.2ms) As expected, at fast imaging speeds the resolution is masked by the signal to noise ratio, which decreases in a 75% due to the low integration times, see Figure 6.7. Therefore, to recover the masked frequencies (and recover the

resolution), higher excitations intensities or brighter samples would be required. In addition, note that larger/smaller active areas can be equally used having slower/faster readings, e.g. 2048x 128 pixels^2 at 1600 fps, (see supplementary table 2 for sCMOS camera specifications).

6.6 Results 2: Applications for in vivo imaging and particle tracking

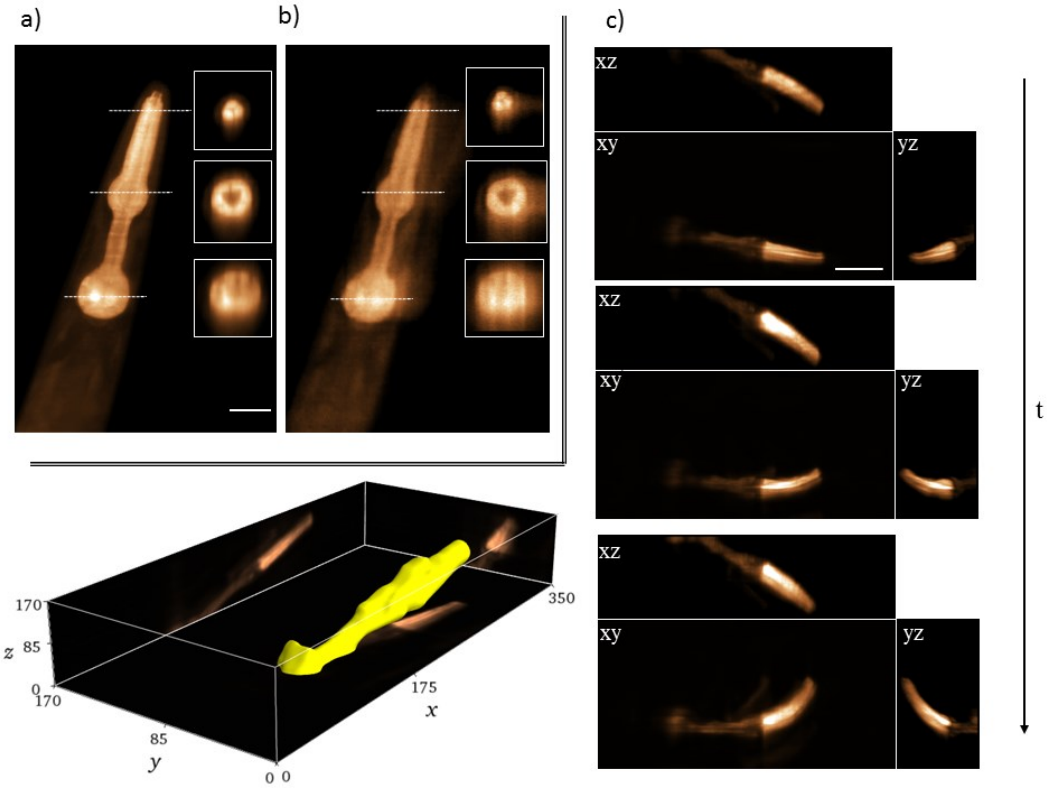

Figure 6.8: WFC-LSFM for fast 4D imaging of *C. elegans* pharyngeal structures.
Maximum intensity projections *xy* projections of a fluorescent *C. elegans* pharynx obtained with a) standard LSFM and b) WFC-LSFM using a cubic phase mask of PV=20 μm. Insets in a) and b) show selected *xz* sections along the dotted lines. Fast volumetric imaging enabled by WFC-LSFM was employed for capturing the movement of a worm recovering from anaesthesia. A set of consecutive frames (Δt=42ms) of this 4D experiment is shown in c), 3D iso-surface rendering is shown in c) bottom-left. Scalebars: a-b) 20μm, c) 50μm.

To show the capabilities of the proposed system for *in vivo* applications we started off by using genetically modified *C. elegans* worms expressing yellow-Cameleon protein in the pharynx region (see methods). Figure 6.8(a) illustrates the results obtained by regular LSFM and Figure 6.8(b) those obtained in WFC-LSFM with the cubic mask with PV=20 μm after the deconvolution. As it can be seen from the xy

projection and the different xz sections that the main features of the pharynx [47], including the buccal cavity, the metacorpus lumen and the grinder, can be recovered.

We then tested the fast capabilities of our WFC-LSFM for *in vivo* imaging . In the first case, the whole pharynx of a moving worm was imaged at a speed up to 573 planes/s or 24 volumes/s. This was enough to reconstruct the 4D (3D+time) pharynx movements of the worm recovering from anaesthesia, see Figure 6.8(c). An iso-surface rendering is also shown at a selected time point to further illustrate the 3D nature of the data retrieved and to visualize better the pharynx boundaries.

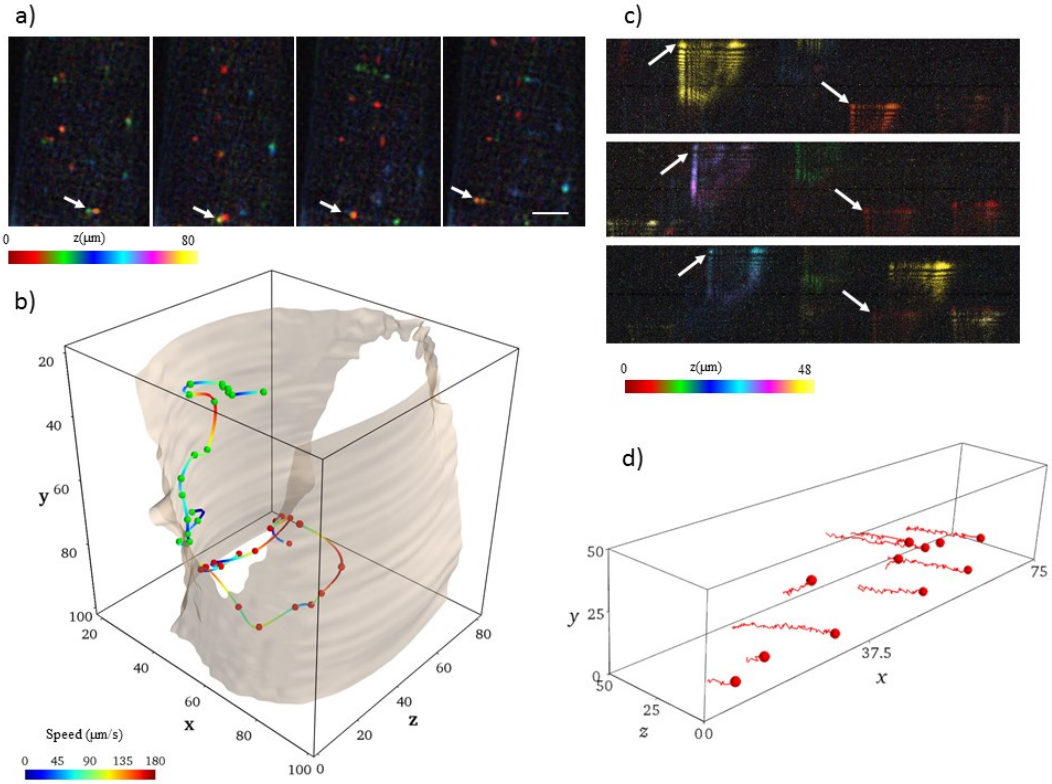

Figure 6.9: WFC-LSFM for fast volumetric structure/particle tracking. Fluorescent neuron cell-bodies of larvae moving inside *C elegans* worm in a "bagging" state were imaged using WFC-LSFM. Figure a) show four 3D consecutive time frames (Δt=100ms) of the deconvolved data. Color indicates depth according to the color bar in the bottom. A couple of cell bodies were tracked and their trajectories were plotted in b). The iso-surface represents the cavity of the host worm where the larvae move, for reference. Color along trajectories indicates the local speed of the larva, according to the colorbar in the bottom. Microspheres floating in PBS were imaged using WFC-LSFM. Figure c) show three 3D consecutive time frames (Δt=13ms) of the original data. Color indicates depth according to the color bar in the bottom. Particles were tracked and their trajectories were plotted in d). Scalebar 10μm

WFC-LSFM enables also the capability of performing fast volumetric tracking of structures and particles. To demonstrate this, we tracked the rapid movements of *C*

elegans larvae inside the body of a worm undergoing in a "bagging" state or *endotokia matricida* [48,49]. In such case, larvae transiting along the host worm resulted in a complex dynamic scenario that can be studied at high speed with the presented method. For this we imaged at a speed of 100 planes/s or 10 volumes/s. Figure 6.9(a) show four consecutive frames (Δt=100ms) color-coded 3D images after the deconvolution process. We then manually tracked the GFP labelled cell bodies of two different larvae. Figure 6.9(b) shows their 3D trajectories and velocity vectors showing the dynamics of this particular biological process. In this case, dynamic speeds up to 180 μm/s could be measured in 4D.

To further show the potential of the developed system for single-particle tracking and particle image velocimetry, we imaged microspheres of 0.2 μm freely floating into the chamber's saline buffer. In this case we set the camera at the maximum speed recommended by the manufacturer, i.e., 1600 planes/s with an effective volumetric imaging speed of 73 volumes/s. Figure 6.9(c) show three consecutive frames (Δt=13ms) color-coded 3D images of the raw data obtained for this sample. In this case we simply recorded the 3D centroid of the main lobe of the PSFs (white arrow in Figure 6.9(c)). The resulting 3D tracks for some microspheres are shown in Figure 6.9(d). A subsequent analysis of the trajectories resulted in a speed of the particles of 32.8 μm/s and diffusion coefficient $D=2.4\pm0.4\mu m^2/s$, which is in good agreement with the expected value D_{ex} =2.10 $\mu m^2/s$ for the same conditions [50].To our knowledge, these two experiments constituted the fastest 3D imaging and tracking performed up to date.

6.7 Conclusion

To sum up, the technology we present integrates LSFM and WFC techniques in a unified system. This provides an unprecedented capability that can be used for obtaining a holistic view of fast biological dynamics in their own environment at video-rate speed, covering the needs for fast 3D imaging and tracking.

In addition, the limitations of the standard WFC technique disappear by combining it with LSFM, opening the door to the development of more suitable WFC masks and artifact-free deconvolution methods. In closing, the proposed technology is a breakthrough in both LSFM and WFC fields.

6.8 References

1. J. Vermot, S. E. Fraser, y M. Liebling, "Fast fluorescence microscopy for imaging the dynamics of embryonic development," HFSP J. **2**, 143-155 (2008).

2. T. Tanaami, S. Otsuki, N. Tomosada, Y. Kosugi, M. Shimizu, y H. Ishida, "High-Speed 1-Frame/ms Scanning Confocal Microscope with a Microlens and Nipkow Disks," Appl. Opt. **41**, 4704-4708 (2002).

3. N. Callamaras y I. Parker, "Construction of a confocal microscope for real-time x-y and x-z imaging," Cell Calcium **26**, 271-279 (1999).

4. E. Wang, C. M. Babbey, y K. W. Dunn, "Performance comparison between the high-speed Yokogawa spinning disc confocal system and single-point scanning confocal systems," J. Microsc. **218**, 148-159 (2005).

5. J. Huisken, J. Swoger, F. Del Bene, J. Wittbrodt, y E. H. K. Stelzer, "Optical Sectioning Deep Inside Live Embryos by Selective Plane Illumination Microscopy," Science **305**, 1007 -1009 (2004).

6. T. F. Holekamp, D. Turaga, y T. E. Holy, "Fast Three-Dimensional Fluorescence Imaging of Activity in Neural Populations by Objective-Coupled Planar Illumination Microscopy," Neuron **57**, 661-672 (2008).

7. J. Huisken y D. Y. R. Stainier, "Even fluorescence excitation by multidirectional selective plane illumination microscopy (mSPIM)," Opt. Lett. **32**, 2608-2610 (2007).

8. P. J. Keller, A. D. Schmidt, A. Santella, K. Khairy, Z. Bao, J. Wittbrodt, y E. H. K. Stelzer, "Fast, high-contrast imaging of animal development with scanned light sheet-based structured-illumination microscopy," Nat Meth **7**, 637-642 (2010).

9. L. Gao, L. Shao, C. D. Higgins, J. S. Poulton, M. Peifer, M. W. Davidson, X. Wu, B. Goldstein, y E. Betzig, "Noninvasive Imaging beyond the Diffraction Limit of 3D Dynamics in Thickly Fluorescent Specimens," Cell **151**, 1370-1385 (2012).

10. Y. Wu, A. Ghitani, R. Christensen, A. Santella, Z. Du, G. Rondeau, Z. Bao, D. Colón-Ramos, y H. Shroff, "Inverted selective plane illumination microscopy (iSPIM) enables coupled cell identity lineaging and neurodevelopmental imaging in Caenorhabditis elegans," Proc. Natl. Acad. Sci. U. S. A. **108**, 17708-17713 (2011).

11. P. J. Keller y E. H. K. Stelzer, "Quantitative in vivo imaging of entire embryos with Digital Scanned Laser Light Sheet Fluorescence Microscopy," Curr. Opin. Neurobiol. **18**, 624-632 (2008).

12. R. Tomer, K. Khairy, F. Amat, y P. J. Keller, "Quantitative high-speed imaging of entire developing embryos with simultaneous multiview light-sheet microscopy," Nat. Methods **9**, 755-763 (2012).

13. U. Krzic, S. Gunther, T. E. Saunders, S. J. Streichan, y L. Hufnagel, "Multiview light-sheet microscope for rapid in toto imaging," Nat. Methods **9**, 730-733 (2012).

14. M. B. Ahrens, M. B. Orger, D. N. Robson, J. M. Li, y P. J. Keller, "Whole-brain functional imaging at cellular resolution using light-sheet microscopy," Nat. Methods **10**, 413-420 (2013).

15. L. N. Vandenberg, C. Stevenson, y M. Levin, "Low frequency vibrations induce malformations in two aquatic species in a frequency-, waveform-, and direction-specific manner," PloS One **7**, e51473 (2012).

16. F. O. Fahrbach, F. F. Voigt, B. Schmid, F. Helmchen, y J. Huisken, "Rapid 3D light-sheet microscopy with a tunable lens," Opt. Express **21**, 21010-21026 (2013).

17. S. Abrahamsson, J. Chen, B. Hajj, S. Stallinga, A. Y. Katsov, J. Wisniewski, G. Mizuguchi, P. Soule, F. Mueller, C. D. Darzacq, X. Darzacq, C. Wu, C. I. Bargmann, D. A. Agard, M. Dahan, y M. G. L. Gustafsson, "Fast multicolor 3D imaging using aberration-corrected multifocus microscopy," Nat. Methods **10**, 60-63 (2013).

18. M. R. Arnison, C. J. Cogswell, C. J. R. Sheppard, y P. Török, "Wavefront Coding Fluorescence Microscopy Using High Aperture Lenses," en *Optical Imaging and Microscopy*, P. Török y F.-J. Kao, eds., Springer Series in Optical Sciences No. 87 (Springer Berlin Heidelberg, 2003), pp. 143-165.

19. P. Potuluri, M. Fetterman, y D. Brady, "High depth of field microscopic imaging using an interferometric camera," Opt. Express **8**, 624-630 (2001).

20. J. Dowski y W. T. Cathey, "Extended depth of field through wave-front coding," Appl. Opt. **34**, 1859-1866 (1995).

21. J. Ojeda-Castaneda, R. Ramos, y A. Noyola-Isgleas, "High focal depth by apodization and digital restoration," Appl. Opt. **27**, 2583-2586 (1988).

22. L. Liu, F. Diaz, L. Wang, B. Loiseaux, J.-P. Huignard, C. J. R. Sheppard, y N. Chen, "Superresolution along extended depth of focus with binary-phase filters for the Gaussian beam," J. Opt. Soc. Am. A Opt. Image Sci. Vis. **25**, 2095-2101 (2008).

23. J. Ojeda-Castaneda, E. Tepichin, y A. Diaz, "Arbitrarily high focal depth with a quasioptimum real and positive transmittance apodizer," Appl. Opt. **28**, 2666-2670 (1989).

24. T. Wilson, M. A. A. Neil, y F. Massoumian, "Point spread functions with extended depth of focus," en (2002), Vol. 4621, pp. 28-31.

25. S. Bradburn, W. T. Cathey, y E. R. Dowski, "Realizations of focus invariance in optical-digital systems with wave-front coding," Appl. Opt. **36**, 9157-9166 (1997).

26. F. Diaz, F. Goudail, B. Loiseaux, y J.-P. Huignard, "Increase in depth of field taking into account deconvolution by optimization of pupil mask," Opt. Lett. **34**, 2970-2972 (2009).

27. R. N. Zahreddine, R. H. Cormack, y C. J. Cogswell, "Noise removal in extended depth of field microscope images through nonlinear signal processing," Appl. Opt. **52**, D1 (2013).

28. D. S. C. Biggs y M. Andrews, "Acceleration of iterative image restoration algorithms," Appl. Opt. **36**, 1766-1775 (1997).

29. G. Carles, "Analysis of the cubic-phase wavefront-coding function: Physical insight and selection of optimal coding strength," Opt. Lasers Eng. **50**, 1377-1382 (2012).

30. C. J. R. S. Matthew R. Arnison, "A 3D vectorial optical transfer function suitable for arbitrary pupil functions," Opt. Commun. **211**, 53-63 (2002).

31. J. H. MCLEOD, "The Axicon: A New Type of Optical Element," J. Opt. Soc. Am. **44**, 592-592 (1954).

32. J. H. MCLEOD, "Axicons and Their Uses," J. Opt. Soc. Am. **50**, 166-166 (1960).

33. T. Čižmár, V. Kollárová, X. Tsampoula, F. Gunn-Moore, W. Sibbett, Z. Bouchal, y K. Dholakia, "Generation of multiple Bessel beams for a biophotonics workstation," Opt. Express **16**, 14024-14035 (2008).

34. G. Druart, J. Taboury, N. Guérineau, R. Haïdar, H. Sauer, A. Kattnig, y J. Primot, "Demonstration of image-zooming capability for diffractive axicons," Opt. Lett. **33**, 366 (2008).

35. G. Häusler y W. Heckel, "Light sectioning with large depth and high resolution," Appl. Opt. **27**, 5165-5169 (1988).

36. P. Dufour, M. Piché, Y. De Koninck, y N. McCarthy, "Two-photon excitation fluorescence microscopy with a high depth of field using an axicon," Appl. Opt. **45**, 9246-9252 (2006).

37. O. E. Olarte, J. Licea-Rodriguez, J. A. Palero, E. J. Gualda, D. Artigas, J. Mayer, J. Swoger, J. Sharpe, I. Rocha-Mendoza, R. Rangel-Rojo, y P. Loza-Alvarez, "Image formation by linear and nonlinear digital scanned light-sheet fluorescence microscopy with Gaussian and Bessel beam profiles," Biomed. Opt. Express **3**, 1492 (2012).

38. T. A. Planchon, L. Gao, D. E. Milkie, M. W. Davidson, J. A. Galbraith, C. G. Galbraith, y E. Betzig, "Rapid three-dimensional isotropic imaging of living cells using Bessel beam plane illumination," Nat Meth **8**, 417-423 (2011).

39. F. O. Fahrbach, P. Simon, y A. Rohrbach, "Microscopy with self-reconstructing beams," Nat Photon **4**, 780-785 (2010).

40. Z. Zhai, S. Ding, Q. Lv, X. Wang, y Y. Zhong, "Extended depth of field through an axicon," J. Mod. Opt. **56**, 1304-1308 (2009).

41. R. Jorand, G. Le Corre, J. Andilla, A. Maandhui, C. Frongia, V. Lobjois, B. Ducommun, y C. Lorenzo, "Deep and Clear Optical Imaging of Thick Inhomogeneous Samples," PLoS ONE **7**, e35795 (2012).

42. W. S. Rasband, "ImageJ, U. S. National Institutes of Health, Bethesda, Maryland, USA," http://rsb.info.nih.gov/ij/.

43. C. Vonesch y M. Unser, "A fast thresholded landweber algorithm for wavelet-regularized multidimensional deconvolution," IEEE Trans. Image Process. Publ. IEEE Signal Process. Soc. **17**, 539-549 (2008).

44. M. Somayaji, V. R. Bhakta, y M. P. Christensen, "Experimental evidence of the theoretical spatial frequency response of cubic phase mask wavefront coding imaging systems," Opt. Express **20**, 1878-1895 (2012).

45. Eric Jones, "SciPy: Open Source Scientific Tools for Python," http://www.scipy.org/.

46. "WormAtlas," http://www.wormatlas.org/.

47. L. Avery y B. B. Shtonda, "Food transport in the C. elegans pharynx," J. Exp. Biol. **206**, 2441-2457 (2003).

48. Chen J. y Caswell-Chen E.P., "Why Caenorhabditis elegans adults sacrifice their bodies to progeny," Nematology **5**, 641-645 (2003).

49. J. Chen y E. P. Caswell-Chen, "Facultative Vivipary is a Life-History Trait in Caenorhabditis elegans," J. Nematol. **36**, 107-113 (2004).

50. B. Rieger, H. R. C. Dietrich, L. R. Van Den Doel, y L. J. Van Vliet, "Diffusion of microspheres in sealed and open microarrays," Microsc. Res. Tech. **65**, 218-225 (2004).

Chapter 7: Conclusions and future perspectives

In this thesis, I have explored several ideas to find new photonic applications to solve problems in biological microscopy. Adaptive optics had been used to correct the aberrations in the optical path of a TPEF microscope to enhance the signal retrieved from different tick samples at different depths. The concept of using an intrinsically generated nonlinear guide star was demonstrated for the first time and applied using biologically relevant samples. In the quest for additional applications of adaptive optics for laser micro-surgery, I have built a new multimodal microscopy work station based on a previous proof-of-principle optical setup. To enhance the reliability of the system the optical setup was completely redesigned and the software was importantly updated. Using this new optical setup, I have developed new techniques based on the use of PSHG microscopy to assess the damage induced by a femtosecond laser when it is employed for laser axotomy of soil worms. Thanks to this, fine adjustment of the power of the femtosecond laser for the dissection of *C elegans* axons in conditions of minimum damage was achieved. This was done even at the level of the structural arrangement of the myosin structure within the muscles adjacent to the axon. Using this know-how, I have developed a complete application for testing axon regeneration enhancing agents employing a custom-made microfluidic chip for immobilization. This development was employed to make the first studies on the effects of the drug Citicoline in the neuron regeneration of invertebrate animal models. Further application of the multimodal microscope for the evaluation of the effects of femtosecond-laser photodisruption in human crystalline lenses was demonstrated. Here, I have presented, for the first time, the use of TPEF for the evaluation of the damage induced by the laser at different depths within the lens. Besides, conditions for changing between low-plasma-density ablation and bubble-mediated photodisruption were characterized. Another path I have followed during my PhD thesis was the use of wavefront engineering methods applied to light-sheet microscopy. Here, I have designed and built a very versatile multimodal LSFM based on a DSLM scheme. Using this system I have proven for the first time the use of femtosecond Bessel beams to excite two-photon fluorescence of living multicellular organisms. I have shown that this modality exploits the full potential of both, self-reconstructing properties, in one side, providing high resolutions over a

larger FOV and nonlinear microscopy, in the other, further enhancing the optical sectioning capabilities of LSFM. In addition to this, I have performed a modification of the original optical setup in order to demonstrate the capabilities of the multimodal LSFM for imaging large, highly-scattering cancer tumor models. Here, it was shown that both modalities 2p- Gaussian and Bessel, employing femtosecond laser beams permit retrieving optical sections with enhanced contrast in biologically relevant MCTS. Besides, the enhanced self-reconstructing properties of femtosecond Bessel beams were demonstrated experimentally by using uniformly stained MCTS. In a similar way, the final application included in this thesis was about the use of wavefront engineering methods to break the scanning paradigms of LSFM. Here I have applied AO principles to extend the DOF of a LSFM collection arm. I have demonstrated how this simple modification release the constraint imposed by the DOF in the excitation sheet, enabling a wide range of new applications. I have presented three relevant applications of this new technology. First, fast imaging of a living specimen at unprecedented volumetric rates was achieved. Second, fast three-dimensional particle tracking and particle velocimetry of cellular structures in a living organism was demonstrated. And third, three-dimensional particle tracking and particle velocimetry of microspheres in solution, were the state-of-the-art detector employed were pushed to its velocity limits. To my knowledge this is the fastest light-sheet microscopy volumetric image ever done.

From the technological development point-of-view this thesis left two fully functional microscopes: the multimodal microscopy workstation and the multimodal LSFM. Both of them are available at the Super Resolution Light microscopy and Nanoscopy facility of ICFO, and are employed by users of the facility in a daily basis. Besides, as we have identified the excellent potential of the device for fast LSFM using and extended DOF a patent was filed on its implementation.

7.1.1 Future perspectives

The future prospects of the technological advancements and applications presented in this thesis are numerous. Firstly, the implementation of AO in the microsurgery with femtosecond lasers is a must. I see two immediate applications that can benefit in the

future from the developed technology, i) the aberration correction for femtosecond microsurgery inside transparent multi-layered structures, such as many microfluidic chips, as long as the target is a fluorescent structure, and, ii) photo-disruption of transparent tissues, such as the crystalline lens, where the autofluorescence generated by with the femtosecond may be employed as nonlinear guide star. In both cases, AO to correct the sample induced aberrations would enhance the efficiency of the energy deposition on the sample, either by reducing the required laser power or by reducing the dissected volume.

Second, axon regeneration studies that were carried out in this thesis demonstrate the potential of this basic model of neuron injury, multimodal imaging and immobilization device, for multiple experiments that would help to understand spontaneous axon regeneration and the evaluation of the effects of some small molecules and drugs on this process. Ideally the developed devices would be combined with novel molecular and genetic tools, to properly address these fundamental questions. Particularly, Citicoline effects on axon regeneration would be amenable to be revisited exploring more extensively the space of parameters: worms ages, distance from the axotomy to ventral cord, spatial and time scales of axon regrowth, frequency and density of branching, etc.

Other interesting prospect that comes from the study on damage assessment is the possibility to use SHG/PSHG to study the mechanism of damage by laser irradiation on muscular structures at the cellular level. The reason why the thick filaments undergo in a change of phase from SB to DB, when a medium to large damage is inflicted with the laser is still controversial, and deserves further investigation.

LSFM implementing TPEF and Bessel beams was shown to be very promising for increasing the excited FOV as well as for imaging thickly scattering samples with high contrast. Nevertheless, the required powers for excitation and imaging MCTSs with this modality are close to the limit considered harmful for biological samples. To alleviate this, changing to fluorescent proteins that have a bigger two-photon action cross-section (than MCherry in our case) would be of great benefit. Also, finely adjusting the Bessel beam length to produce a shorter but still reasonable

FOV, may help to reduce the beam axial spreading and therefore the total average power employed.

Finally, the LSFM system developed for fast, unperturbed imaging would provide an ideal environment for fast/volumetric localization-based super-resolution microscopy (STORM/PALM) or single particle/molecule techniques. In fact, initial calculations showed that using WFC-LSFM would result in a system able to increase up-to 20 times the actual volumes covered by standard localization-based microscopes.

Fast volumetric imaging of 3D Calcium dynamics in neuron cultures can be also benefited with this novel technology. The required frame rate required to image calcium waves in 2D is usually of 100Hz. This indicates that, for a volumetric calcium wave image, every plane should be recorded at such speed. To do that, the full potential of the employed camera can be exploited by running at 1600Hz and acquiring 16 planes of calcium data instead of just one. This would be a breakthrough in the field.